



Michigan Technological University  
*Create the Future* Digital Commons @ Michigan Tech

---

Dissertations, Master's Theses and Master's  
Reports - Open

Dissertations, Master's Theses and Master's  
Reports

---

2012

## Performance evaluation and characterization of symmetric capacitors with carbon black, and asymmetric capacitors using a carbon foam supported nickel electrode

JinJin Wang  
*Michigan Technological University*

Follow this and additional works at: <https://digitalcommons.mtu.edu/etds>

 Part of the [Chemistry Commons](#)

Copyright 2012 JinJin Wang


---

### Recommended Citation

Wang, JinJin, "Performance evaluation and characterization of symmetric capacitors with carbon black, and asymmetric capacitors using a carbon foam supported nickel electrode", Master's Thesis, Michigan Technological University, 2012.

<https://doi.org/10.37099/mtu.dc.etds/33>

Follow this and additional works at: <https://digitalcommons.mtu.edu/etds>

 Part of the [Chemistry Commons](#)

PERFORMANCE EVALUATION AND CHARACTERIZATION OF SYMMETRIC  
CAPACITORS WITH CARBON BLACK, AND ASYMMETRIC CAPACITORS USING  
A CARBON FOAM SUPPORTED NICKEL ELECTRODE

by

JINJIN WANG

A THESIS

Submitted in partial fulfillment of the requirements for the degree of

MASTER OF SCIENCE

(Chemistry)

MICHIGAN TECHNOLOGICAL UNIVERSITY

2012

© 2012 JINJIN WANG

This thesis, "Performance Evaluation and Characterization of Symmetric Capacitors with Carbon Black, and Asymmetric Capacitors Using a Carbon Foam Supported Nickel Electrode," is hereby approved in partial fulfillment of the requirements for the Degree of MASTER OF SCIENCE IN CHEMISTRY.

Department of Chemistry

Signatures:

Thesis Advisor

\_\_\_\_\_  
Dr. Bahne C. Cornilsen

Department Chair

\_\_\_\_\_  
Dr. Sarah A. Green

Date

\_\_\_\_\_

# Table of Contents

List of Figures .....	vii
List of Tables.....	xi
Acknowledgement .....	xiv
Abstract .....	xv
Chapter 1 Introduction .....	1
Chapter 2 Background .....	5
2.1 History of Electrochemical Capacitors .....	5
2.2 Advantages and Applications of ECs .....	6
2.3 Fundamental Theory of Electrochemical Capacitors .....	10
2.3.1 Basic Principles of the Electrochemical Capacitor .....	10
2.3.2 Basic Principles of the Asymmetric Electrochemical Capacitor .....	11
2.4 Ni(OH) <sub>2</sub> / NiOOH Active Mass Structure .....	14
Chapter 3 Methods and Characterization Techniques.....	18
3.1 Instruments and Chemicals .....	18
3.2 Experiment Method .....	19
3.2.1 Positive Electrode Preparation for Asymmetric Cells .....	19

3.2.2 Negative Electrodes Preparation and Characterization.....	23
3.3 Assembly of Symmetric and Asymmetric Cells .....	25
3.4 Symmetric and Asymmetric Cells Characterization .....	27
3.5 XRD Characterization of the Positive Electrodes.....	27
3.5.1 XRD Sample Preparation.....	28
3.5.2 XRD Powder Pattern Collection.....	29
3.5.3 XRD Powder Pattern Calculation .....	30
Chapter 4 Results .....	31
4.1 Electrochemical Characterization of Symmetric Capacitors .....	31
4.1.1 Cyclic Voltammetry Measurements .....	31
4.1.2 Constant Charge / Discharge Cycling.....	35
4.1.3 Comparison of CV and Cycling Performance .....	39
4.2 BET Surface Area and Resistivity Measurements for Negative Electrodes .....	41
4.3 Electrochemical Characterization of Asymmetric Capacitors .....	45
4.3.1 Constant Current Experiment .....	45
4.3.2 Cycle Life Test.....	49
4.4 XRD Characterization of Nickel Hydroxide Electrodes.....	51
4.4.1 The Electrochemical Performance of Nickel Hydroxide Electrodes .....	51
4.4.2 The XRD Patterns of Six Samples.....	56

Chapter 5 Discussion .....	59
5.1 Evaluation of Symmetric Capacitors .....	59
5.1.1 Evaluation of the 3 wt% Symmetric Capacitor .....	59
5.1.2 Evaluation of the 5 wt% Symmetric Capacitor .....	60
5.1.3 Comparison of the 3 wt%, 5 wt%, and 10 wt% Symmetric Capacitors .....	61
5.2 Evaluation of the Asymmetric Capacitor J2 .....	62
5.2.1 Evaluation of the Asymmetric Capacitor J2 at 31.16 mA/cm <sup>2</sup> Current Density .....	63
5.2.2 Evaluation of the Asymmetric Capacitor J2 at 20.46 mA/cm <sup>2</sup> Current Density .....	65
5.3 Comparison of Cell J2 with Previous Work and Literature .....	70
5.4 Evaluation of the Cycle Life Testing of the Asymmetric Cells .....	71
5.5 Evaluation of XRD Characterization of Nickel Electrode.....	72
5.5.1 Evaluation of the XRD Pattern for the Deposited Electrode .....	73
5.5.2 Evaluation of the XRD Patterns for Charged 1x and Charged 10x Electrodes	78
5.5.3 Evaluation of the XRD Pattern for Discharged Electrodes .....	80
Chapter 6 Conclusions and Future Work .....	88
6.1 Conclusions.....	88
6.1.1 Conclusions: Symmetric Capacitors .....	88

6.1.2 Conclusions: Asymmetric Capacitors .....	88
6.1.3 Conclusions: XRD Characterization of the Positive Electrode .....	89
6.2 Future Work .....	89
References .....	91
Appendix A Preparation and XRD Characterization of the 50 % Discharged Electrode .....	96
Appendix B IR Spectra of the Chemically Prepared Nickel Compounds .....	100
Appendix C The Charge/Discharge Capacities of Nickel Positive Electrodes for XRD Characterization .....	105

## LIST OF FIGURES

Fig. 1.1. Bode diagram: electrochemical cycles and their transformation during aging and overcharge process. ....	3
Fig. 2.1. Ragone plot of the specific power and specific energy capabilities of various electrochemical devices, including electrochemical capacitor.....	6
Fig. 2.2. Schematic diagram of a double-layer capacitor showing electrolyte film in contact with carbon particles .....	11
Fig. 2.3. Schematic diagram of ion movement during the charging process (C(-) indicates negative electrons on the surface of carbon electrode).....	13
Fig. 2.4. The modified Body diagram.....	14
Fig. 2.5. Defect representation of Nickel Hydroxide Electrode .....	17
Fig. 3.1. Example of flooded cell.....	21
Fig. 3.2. Typical deposition profile ( $100 \text{ mA/cm}^2$ ).....	21
Fig. 3.3. Example of 45 min deposited electrode .....	22
Fig. 3.4. Voltage profile of the formation process for a nickel hydroxide electrode relative to a Hg/HgO reference electrode. ....	23
Fig. 3.5. Carbon black electrodes (3 wt% PTFE/CB and 97% Ketjenblack, EC-600JD) .....	24
Fig. 3.6. Swagelok cell connected for charge-discharge cycling.....	26
Fig. 4.1. CV plot obtained at different scan rates in the 3 wt% symmetric capacitor	32
Fig. 4.2. CV plot obtained at different scan rates in the 5 wt% symmetric capacitor (Swagelok-type PFA cell, Celgard 3501 separator, 5 wt% PTFE/CB). ....	34
Fig. 4.3. Potential vs. time response of the 3 wt% symmetric capacitor at $30.0 \text{ mA/cm}^2$ current density for first 6 cycles .....	36
Fig. 4.4. Potential vs. time response for the 3 wt% symmetric capacitor at 1 <sup>st</sup> and	



300 <sup>th</sup> cycle numbers with 30.0 mA/cm <sup>2</sup> current density .....	36
Fig. 4.5. The discharge capacity and efficiency vs. function of cycle number of the 3 wt% symmetric capacitor at 30.0 mA/cm <sup>2</sup> over 300 cycles .....	37
Fig. 4.6. Potential vs. time response of the 5 wt% symmetric capacitor at 18.8 mA/cm <sup>2</sup> current density for first 5 cycles .....	37
Fig. 4.7. Potential vs. time response for the 5 wt% symmetric capacitor at 1 <sup>st</sup> and 300 <sup>th</sup> cycle numbers with 18.8 mA/cm <sup>2</sup> current density .....	38
Fig. 4.8. The discharge capacity and efficiency vs. function of cycle number of the 5 wt% symmetric capacitor at 18.8 mA/cm <sup>2</sup> over 300 cycles .....	38
Fig. 4.9. Comparison of the CV performance of the 3 wt% and 5 wt% symmetric cells at the 100 mV/s scan rate.....	39
Fig. 4.10. Ragone plot for the 3 wt%, 5 wt%, and 10 wt% symmetric capacitors .....	41
Fig. 4.11. ER as a function of the PTFE/CB wt% .....	44
Fig. 4.12. The energy and power density as the function of ER for the 3 wt%, 5 wt% and 10 wt% symmetric cells .....	44
Fig. 4.13. Discharge capacity as a function of cycle life at three current densities....	46
Fig. 4.14. Ragone plot for the J2 asymmetric capacitor .....	46
Fig. 4.15. Comparison of the potential vs. time response between the first, middle and last cycles for the asymmetric capacitor (J2) at three different current densities .....	48
Fig. 4.16. Discharge capacity as a function of cycle life for asymmetric J1, J2, and J3 at 31.16, 7.79, and 5.85 mA/cm <sup>2</sup> , respectively .....	49
Fig. 4.17. Comparison of the cell specific capacitance of the J1, J2 and J3 asymmetric capacitors.....	50
Fig. 4.18. Ragone plot for the J1, J2 and J3 asymmetric capacitor .....	51
Fig. 4.19. Potential vs. time response of the formed electrode.....	52

Fig. 4.20. Potential vs. time response of the charged 1x at 10 mA/cm <sup>2</sup> .....	52
Fig. 4.21. Potential vs. time response of the discharged 1x at 10 mA/cm <sup>2</sup> with a Hg/HgO reference electrode. ....	53
Fig. 4.22. Potential vs. time response of a typical cycle (a), the entire cycle of the charged 10x (b), at 10 mA/cm <sup>2</sup> with a Hg/HgO reference electrode. ....	54
Fig. 4.23. Potential vs. time response of a typical cycle, cycle 2 (a), the first cycle showing extensive overcharging (b), the entire set of 10 cycles through the 10 <sup>th</sup> discharge (c), at 10 mA/cm <sup>2</sup> with a Hg/HgO reference electrode. ....	55
Fig. 4.24. Comparison of the XRD powder patterns of deposited (a), formed (b), charged 1x (c) and discharged 1x (d), charged 10x (e) and discharged 10x (f) electrodes .....	56
Fig. 4.25. Comparison of the XRD patterns of the charged 1x (c) and charged 10x (e) electrodes .....	57
Fig. 4.26. Comparison of the XRD patterns of the formed (b), discharged 1x (d), and discharged 10x (f) electrodes .....	57
Fig. 5.1. Ragone plot for the 3 wt% symmetric cell, asymmetric Ni(OH) <sub>2</sub> /AC cells, J2, SW 104, and Zn-Co co-doped Ni(OH) <sub>2</sub> /AC .....	70
Fig. 5.2. XRD Powder Pattern Calculation.....	75
Fig. 5.3. Comparison of experimental XRD pattern of the deposited electrode (a) and the calculated XRD pattern (b) with R $\bar{3}$ m structure.....	77
Fig. 5.4. Comparison of experimental XRD patterns of the charged 1x (a) and 10x (b) electrodes and calculated XRD pattern (c) with R $\bar{3}$ m structure.....	79
Fig. 5.5. Comparison of the experimental XRD pattern of the formed electrode (b) with the calculated XRD patterns of P $\bar{3}$ m $\beta'$ (c) and R $\bar{3}$ m 3 $\gamma$ (a).....	83
Fig. 5.6. Comparison of experimental XRD patterns: the discharged 1x (c) and discharged 10x (b), with the calculated P $\bar{3}$ m $\beta'$ pattern (d) and the calculated R $\bar{3}$ m 3 $\gamma$ pattern (a).....	86
Fig. A.1. Potential vs. time response for the 6 cycle preparation of the 50% discharged sample (a) with an expansion of the last 50% discharge cycle (b) at 10 mA/cm <sup>2</sup>	

versus a Hg/HgO reference electrode. ....	97
Fig. A.2. Comparison of experimental XRD pattern of the 50% discharged electrode, in the 6 <sup>th</sup> cycle (b) with the calculated XRD patterns of $P\bar{3}m\beta'$ (c) and $R\bar{3}m$ $3\gamma$ (a). ....	98
Fig. A.3. Comparison of experimental XRD patterns of the formed (a), the discharged 1x (b), the 50% discharged (c), and the discharged 10x (d) electrodes .....	99
Fig. B.1. IR spectrum of sample no. 2 (reduced).....	101
Fig. B.2. IR spectrum of the sample no. 3 (re-oxidized). ....	102
Fig. B.3. IR spectrum of sample no. 4 (heated sample).....	103
Fig. B.4. IR spectrum of sample no. 5 (re-oxidized of the heated sample) with 300 scans on Bruker, IFS-66 FTIR .....	104

## LIST OF TABLES

Table 2.1. Comparison of some important characteristics of the electrochemical capacitors and lithium-ion batteries. ....	8
Table 2.2. Applications of ECs which serve as backup power sources .....	9
Table 2.3. Applications of ECs which serve as main power sources .....	9
Table 2.4. Comparison of empirical and nonstoichiometric formulae.....	16
Table 3.1. A series of negative electrodes. ....	25
Table 3.2. Components of symmetric and asymmetric cells. ....	26
Table 3.3. Electrodes used for XRD characterization. ....	29
Table 4.1. Cell specific capacitance and columbic efficiency calculated for the 3 wt% symmetric capacitor, at five different CV scan rates .....	33
Table 4.2. Cell specific capacitance and columbic efficiency calculated for the 5 wt% symmetric capacitor, at five different CV scan rates .....	35
Table 4.3. Comparison of cell specific capacitances, energy, and power densities for the 3 wt%, 5 wt% and 10 wt% symmetric capacitors.....	40
Table 4.4. BET surface areas of 3 wt% and 5 wt% PTFE/CB electrodes.....	42
Table 4.5. Effective resistance, ER for 3 wt%, 5 wt% and 10 wt% PTFE/CB electrodes at $\Delta V = 0.0010$ V .....	43
Table 4.6. Comparison of the average specific capacitance, energy and power density of asymmetric capacitor (J2) as a function of the current density .....	47
Table 4.7. Comparison of cycle life, cell specific capacitance, energy and power density of asymmetric capacitor J1, J2, and J3 .....	50
Table 4.8. Experimental XRD patterns of six samples. ....	58
Table 5.1. Comparison of the constant current charge/discharge times, $\Delta V_{IR}$ , cell capacitances, efficiencies, energy, and power densities for the cycles at 31.16	

mA/cm <sup>2</sup> .....	64
Table 5.2. Comparison of the constant current charge/discharge times, $\Delta V_{IR}$ , cell capacitances, efficiencies, energy, and power densities for the cycles at 20.46 mA/cm <sup>2</sup> . ....	66
Table 5.3. Comparison of the constant current charge/discharge times, $\Delta V_{IR}$ , cell capacitances, efficiencies, energy, and power densities for the cycles at 7.79 mA/cm <sup>2</sup> . ....	69
Table 5.4. Input parameters for the R $\bar{3}$ m structural model of the deposited electrode for the XRD powder pattern calculation. ....	76
Table 5.5. The experimental XRD pattern of the deposited electrode and the calculated pattern with R $\bar{3}$ m structure (see Table 5.4). ....	77
Table 5.6. Input parameters for R $\bar{3}$ m structural model of the charged 1x and 10x electrodes in XRD calculation. ....	79
Table 5.7. The experimental XRD pattern of the charged 1x and 10x electrodes and the calculated pattern with R $\bar{3}$ m structure. ....	80
Table 5.8. Input parameters for the P $\bar{3}$ m structural model of the formed electrode for the XRD powder pattern calculation.....	82
Table 5.9. Comparison of the experimental XRD pattern with the calculated P $\bar{3}$ m and R $\bar{3}$ m patterns for the formed sample (see input in Table 5.8 and 5.6). ....	84
Table 5.10. Input parameters for a P $\bar{3}$ m structural model of the discharged 1x and 10x electrodes for the XRD powder pattern calculation.....	85
Table 5.11. Comparison of the experimental XRD patterns for the discharged 1x and 10x electrodes with the calculated pattern with P $\bar{3}$ m and R $\bar{3}$ m structures. ....	87
Table A.1. The capacities, depth of discharge (discharged to 0.0 V), cut off charge voltage, the charge and discharge times of the formation and cycling processes for the 50% discharged electrode (after 6 <sup>th</sup> cycle). ....	96
Table A.2. Input parameters for the P $\bar{3}$ m structural model of the 50% discharged sample for the XRD powder pattern calculation.....	98
Table A.3. Comparison of the experimental XRD pattern of the 50% discharged	

sample and the calculated patterns with the $P\bar{3}m$ and $R\bar{3}m$ structures.....	99
Table B.1. Preparation of the Nickel Hydroxide/Oxyhydroxide Compounds .....	100
Table C.1. The capacities, depth of discharge (discharge to 0.0 V), cut off charge voltage, the charge and discharge time of the formed electrode.....	105
Table C.2. The capacities, depth of discharge (DOD, discharge to 0.15 V), cut off charge voltage, the charge and discharge time of the formation and cycling process of the charged 1x electrode. ....	106
Table C.3. The capacities, depth of discharge (DOD, discharge to 0.15 V), cut off charge voltage, the charge and discharge time of the formation and cycling process of the discharged 1x electrode. ....	107
Table C.4. The capacities, depth of discharge (DOD, discharge to 0.15 V), cut off charge voltage, the charge and discharge time of the formation and cycling process of the charged 10x electrode. ....	108
Table C.5. The capacities, depth of discharge (DOD, discharge to 0.15 V), cut off charge voltage, the charge and discharge time of the formation and cycling process of the discharged 10x electrode. ....	109

## ACKNOWLEDGEMENT

I give my deepest gratitude to my advisor, Dr. Bahne C. Cornilsen for his guidance, support and patience to help me accomplish my project and become an independent researcher. His understanding and warm personality has made my academic journey so rewarding. I am also grateful to Dr. Tony N. Rogers, who serves as my unofficial co-advisor, for all his encouragement and precious suggestion to help me grow. Also, a big thank you goes to my committee member Dr. Shiyue Fang for his thoughtful suggestions and instructions in writing my thesis.

I would like to further thank Dr. Pushpalatha Murthy and Dr. Patricia A. Heiden for their great assistance, Dr. Faith A. Morrison for allowing me to use her lab, Mr. Edward A. Laitila for x-ray training and discussion of my results, the Department of Chemistry and Department of Geology for use of equipment and facilities.

I would like to extend my appreciations to my colleagues, Ming Ning, Padmanaban Sasthan Kuttipillai, Matthew B. Chye, and Wen Nee Yeo. From them, I have learned many useful and practical techniques, which are seldom covered in the published papers or books.

Finally, thank you go to my parents for their unconditional love and support throughout my studies, my dear friends, Jing, Zhichao, Hui, Tan, Matha, Mimi, Jingtuo, Ning and all my friends for their earnest help and accompany. I am very lucky to have all of you in my life.

Lastly, I offer my regards and blessings to all of those who supported me in any respect during the completion of the project.

## ABSTRACT

This thesis evaluates a novel asymmetric capacitor incorporating a carbon foam supported nickel hydroxide positive electrode and a carbon black negative electrode. A series of symmetric capacitors were prepared to characterize the carbon black (CB) negative electrode. The influence of the binder, PTFE, content on the cell properties was evaluated. X-ray diffraction characterization of the nickel electrode during cycling is also presented.

The 3 wt% and 5 wt% PTFE/CB symmetric cells were examined using cyclic voltammetry (CV) and constant current charge/discharge measurements. As compared with symmetric cells containing more PTFE, the 3 wt% cell has the highest average specific capacitance, energy density and power density over 300 cycles, 121.8 F/g, 6.44 Wh/kg, and 604.1 W/kg, respectively. Over the 3 to 10 wt% PTFE/CB range, the 3 wt% sample exhibited the lowest effective resistance and the highest BET surface area.

Three asymmetric cells (3 wt% PTFE/CB negative electrode and a nickel positive) were fabricated; cycle life was examined at 3 current densities. The highest average energy and power densities over 1000 cycles were 20 Wh/kg (21 mA/cm<sup>2</sup>) and 715 W/kg (31 mA/cm<sup>2</sup>), respectively. The longest cycle life was 11,505 cycles (at 8 mA/cm<sup>2</sup>), with an average efficiency of 79% and an average energy density of 14 Wh/kg.

The XRD results demonstrate that the cathodically deposited nickel electrode is a typical  $\alpha$ -Ni(OH)<sub>2</sub> with the R $\bar{3}$ m structure (ABBCA stacking); the charged electrodes are  $3\gamma$ -NiOOH with the same stacking as the  $\alpha$ -type; the discharged electrodes (including as-formed electrode) are aged to  $\beta'$ -Ni(OH)<sub>2</sub> (a disordered  $\beta$ ) with the P $\bar{3}$ m structure (ABAB stacking). A  $3\gamma$  remnant was observed.



# CHAPTER 1

## INTRODUCTION

The electrochemical capacitor (EC) has attracted much attention in recent years as an energy storage device due to the high power performance and long cycle life.<sup>1-2</sup> Because of different charge storage mechanisms, there are two types of ECs: one type just stores charge in electrical double layers at the electrode/electrolyte interface (symmetric ECs); another type utilizes both electrical double layers and Faradaic redox processes to store energy (asymmetric ECs). Considerable recent research has focused on ECs which was aimed at increasing power and energy density as well as lowering fabrication costs while using environmentally friendly materials. From the materials point of view, activated carbons (ACs), conducting polymers, and transition-metal oxides are fundamental candidates for supercapacitor electrode materials.<sup>2-3</sup> Among these materials, active carbon (AC) materials are widely used due to their high specific surface area (SSA) and high electrical conductivity. The specific capacitance of the ACs linearly increases with the SSA and the ACs exhibit specific capacitances of 70-180 F/g, 35-60 F/cm<sup>-3</sup>, in common non-aqueous electrolytes.<sup>4-6</sup>

Although porous electrodes with high surface areas can increase the specific capacitance of an EDLC, there is still a major problem with high-specific-surface-area carbons: not all of the Brunauer-Emmett-Teller (BET) surface area is electrochemically accessible to the electrolyte.<sup>7</sup>

In addition, the applications of symmetric ECs are limited by low energy density. In order to increase the energy density, and at the same time maintain the long cycle life and fast charge capability, a hybrid system combining an EC of high power density to a battery of high energy density was introduced.<sup>8</sup> This is known as an asymmetric capacitor. Various

combinations of anode and cathode have been reported, such as metal oxides/AC, conductive polymers/AC and  $\text{Li}_4\text{Ti}_5\text{O}_{12}/\text{AC}$ .<sup>8-11</sup> Amorphous metal oxides ( $\text{NiO}$  and  $\text{RuO}_2$ ) are also widely studied as potential electrode material candidates for higher energy redox capacitors.<sup>12-13</sup> Also, nickel hydroxide was introduced as a candidate for a positive electrode material.<sup>14</sup> Beliakov, *et al.* first reported an asymmetric EC composed of a  $\text{Ni}(\text{OH})_2$  positive electrode with high energy storage capacity and an AC negative electrode with high power showed enhanced specific capacitance.<sup>11</sup>

Bode, *et al.*'s interpretation of nickel electrode chemistry proposes that the  $\text{Ni}(\text{OH})_2$  exists in two polymorphic forms, known as  $\alpha\text{-Ni}(\text{OH})_2$  and  $\beta\text{-Ni}(\text{OH})_2$ , within the cycled materials. They suggest that these are transformed, on charging, into what Bode called  $\gamma\text{-NiOOH}$  and  $\beta\text{-NiOOH}$ , respectively (see Fig.1.1).<sup>15</sup> Their interpretation is based upon the XRD patterns of chemically produced  $\alpha\text{-Ni}(\text{OH})_2$  and  $\beta\text{-Ni}(\text{OH})_2$ .

Currently,  $\beta\text{-Ni}(\text{OH})_2$  is often chosen as a positive electrode material in the battery industry. If overcharging is involved, the  $\beta\text{-Ni}(\text{OH})_2/\beta\text{-NiOOH}$  cycle is transformed into an  $\alpha\text{-Ni}(\text{OH})_2/\gamma\text{-NiOOH}$  cycle, and is accompanied with a large volumetric change. Some authors suggest this change causes rapid capacity fading during electrochemical charge/discharge.<sup>15</sup> They suggest that as compared with the  $\beta\text{-Ni}(\text{OH})_2$  and  $\beta\text{-NiOOH}$  cycle, it is much more advantageous for the  $\alpha\text{-Ni}(\text{OH})_2$  and  $\gamma\text{-NiOOH}$  cycle. In order to understand the electrochemical mechanism of this electrode, there has been a tremendous amount of work done.<sup>15,16-18</sup>

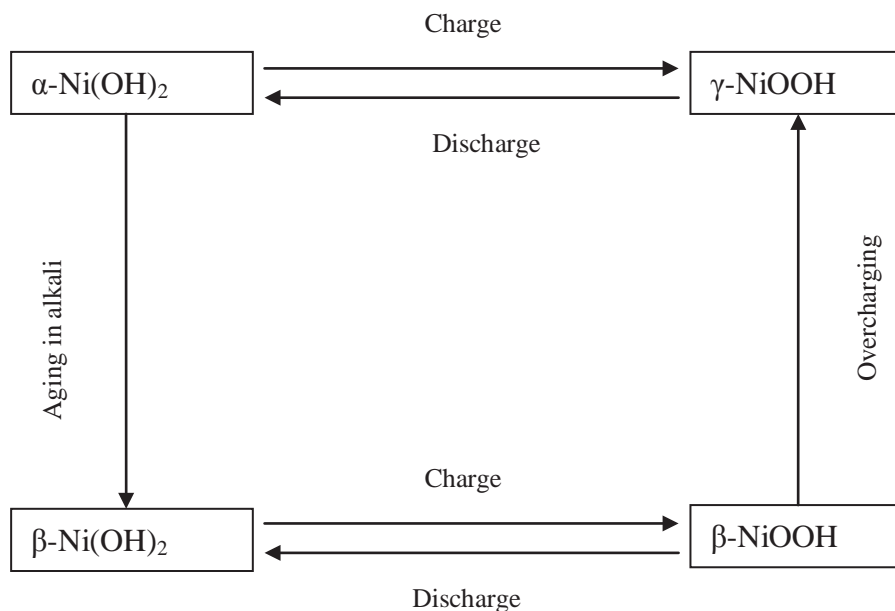


Fig. 1.1. Bode diagram: electrochemical cycles and their transformation during aging and overcharge process.

However, due to the complexity of nickel electrode materials, their structure must be precisely defined during the charge/discharge process. In order to improve the performance of an asymmetric capacitor, it is very important to understand the structure change of the nickel electrode during the cycling process (this is discussed further in the following, section 2.4).

The goal of this work is to test the Ni/C foam positive electrode to determine optimum cycle life. Asymmetric capacitors, combining a high power density EC electrode and a high energy density Faradic electrode are well known for high efficiency and significantly improved energy density. To do this, we choose a  $\text{Ni(OH)}_2/\text{C}$  asymmetric capacitor with carbon black (Ketjenblack EC-600JD) negative electrode. These asymmetric capacitors will be fully studied and characterized electrochemically by the constant current charge/discharge. After that, XRD will be employed to identify the structural changes during the charge/discharge processes. An XRD powder pattern

calculation program has been applied to predict the powder patterns for various model structures for comparison with experimental power patterns.

## CHAPTER 2

### BACKGROUND

#### 2.1 History of Electrochemical Capacitors

Unlike the battery, electrochemical capacitors (EC) possess a high power density and longer cycle life. They bridge the gap between batteries and conventional dielectric capacitors, which can be observed in Ragone plots (see Fig. 2.1).<sup>1</sup>

It was Becker from the General Electric Co. in 1957 who first reported an electrical device using electrochemical double layer charge storage.<sup>19</sup> However, Robert A. Rightmire, a chemist at the Standard Oil Company of Ohio (SOHIO), has been credited with the invention of the commonly used format of the EC in 1966.<sup>20</sup> In 1971, Tarasatti and Buzzanco first noted that there was some similarity between the electrochemical charging behavior of metal oxide films and that of a capacitor during the cyclic voltammetry experiments conducted in ruthenium oxide films.<sup>21</sup> Then, Conway and his co-workers reported pseudo-capacitance was involved in this type of metal oxide capacitor due to a Faradaic transfer of charge to the electrode surface from the electrolyte.<sup>22</sup> During the transfer process, there are more charges involved and stored than in the double layer alone, which can tremendously increase the capacitance of capacitors. However, the high cost of these materials cannot meet the economical demands for large-scale commercialization. Nickel oxide, cobalt oxide and manganese oxide have been reported to replace ruthenium oxide due to their low cost and similar pseudo capacitive behavior.<sup>23-25</sup>

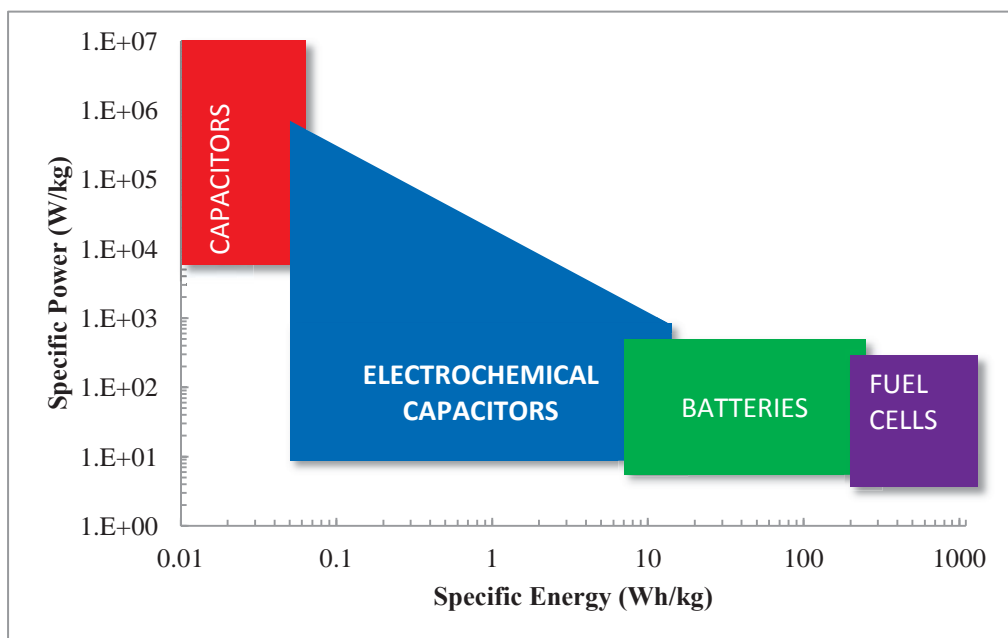


Fig. 2.1. Ragone plot of the specific power and specific energy capabilities of various electrochemical devices, including electrochemical capacitor.

There were only a few volts (1 to 3 V) rated for early designed ECs and the capacitance values were measured from  $10^{-2}$  F up to several F in 1980s.<sup>26</sup> Today, the EC has grown from the small milli-farad-size devices up to devices rated at hundreds of farads. The next step is to broaden the scope of EC application such as replacing batteries in some cases and complementing other energy sources (*e.g.*, solar cells and fuel cells). In the recently years, ECs are introduced into market and have many new applications. Under the most considered ones are electric vehicles (EVs), hybrid electric vehicles (HEVs) and fuel cell vehicles.

## 2.2 Advantages and Applications of ECs

In general, ECs have many advantages. First of all, ECs do not contain hazardous or toxic materials and are very easy to dispose of compared with batteries. Besides, ECs are

more beneficial than the batteries when attention turns to thermal management. HEVs are always involved in rapid charge/discharge cycles and high power levels. Due to the high charge/discharge efficiency, the energy lost to heat during each cycle relatively small and readily removed for ECs.<sup>26</sup> The comparison of a commercial lithium-ion battery with the EC is shown in Table 2.1.<sup>27</sup> Last but not least, the cycle life of the properly designed EC system is 500,000 cycles or higher.<sup>28</sup> Although great advances have been made to extend the cycle life of batteries, the chemical changes that take place suggest that their cycle life for deep discharge will always be limited.

Considering these benefits, an increasing number of companies have focused on developing them such as Maxwell Technologies, Siemens Matsushita, NEC, Panasonic, ELNA, and TOKIN.<sup>28</sup> There are many commercial ECs (*e.g.*, Maxwell, Siemens, and NEC) that have already stepped into the market. At present, ECs only have less than 1% of electric energy storage in the world market.<sup>29</sup> They show strongly growing market numbers. There are mainly two types of ECs applications. The first typical application of ECs is to serve as backup power during power failures or while charging batteries (see Table 2.2).<sup>28</sup> In load-leveling, ECs serve as the energy storage for hydro-electric, solar cell, and wind power generation. For example, on a day-night basis, the electric load is supplied, for example, by solar cell during the day. In the meantime, the solar cell also charges the EC. During the night, the power is delivered by the EC. In another applications, ECs are used as the main power source (see Table 2.3).<sup>28</sup>

In the recent market, the automotive and transportation businesses provide many opportunities for ECs. In the area of electric vehicles (EV), hybrid electric vehicles (HEV) and fuel cell vehicles, ECs serve as short time energy storage device with high power capability, and ECs can store the energy obtained from regenerative braking.<sup>30</sup> This energy can be applied to the next acceleration phase and boost the acceleration. Besides, the

application of ECs allows the reduction of the size of primary power source, which are batteries of EV, internal combustion engine of HEV, and keep these vehicles running at an optimized operation point.

Compared with conventional devices with more than 100 years in the market, ECs are very young and still face some challenges. First of all, the capacitance needs to be increased. Another challenge is the high voltage demanded for many applications. Due to the low voltage of a single cell, several dozens or hundreds of cells must be connected in series. And, one single damaged cell may destroy the performance of the whole capacitor system. However, taking the irreplaceable advantages of ECs into consideration, we are convinced that there should be a huge potential market for ECs in the future.

Table 2.1.  
Comparison of some important characteristics of the electrochemical capacitors and lithium-ion batteries.

<b>Characteristic</b>	<b>Lithium Ion Battery</b>	<b>Electrochemical Capacitor (Symmetric cell)</b>
Charge time	~3-5 minutes	~1 second
Discharge Time	~3-5 minutes	~1 second
Cycle life	<5,000 @ 1C rate	>500,000
Specific Energy (Wh/kg)	70-100	5
Specific power (kW/kg)	0.5 - 1	5 - 10
Cycle efficiency (%)	<50% to >90%	<75 to >95%
Cost/Wh	\$1-2/Wh	\$10-20/Wh
Cost/kW	\$75-150/kW	\$25-50/kW



Table 2.2.  
Applications of ECs which serve as backup power sources

<b>Applications</b>	<b>Functions</b>	<b>Durations</b>
Video recorders, TV satellite receivers	Recording times, and clock time; backup of TV-channel setting	Hours to weeks
Car audio system, taxi meter	Backup of radio station memory, taxi fare programs and accumulated fare data, when the car battery is disconnected	A few hours to a few days
Alarm clock radios, process controllers, bakery, coffee machines	Protect clocks and programmed functions from getting lost in case of temporary power outage.	Minutes to hours
Photo and video cameras, calculators, electronic agendas, mobile phones	Backup is provided during the replacement of the batteries	Seconds to minutes

Table 2.3.  
Applications of ECs which serve as main power sources

<b>Applications</b>	<b>Benefits</b>
Power tools and appliances	High power density
Fail-safe positioning in case of power failures	Smaller, cheaper and faster systems
Start/stop applications in cars	Smaller size and double the cycle life

## 2.3 Fundamental Theory of Electrochemical Capacitors

### 2.3.1 Basic Principles of the Electrochemical Capacitor

Traditionally, ECs have two identical electrodes separated by an electrolyte. These two electrodes are typically made with the same type materials and have the same weight and volume. Active carbons are the most common materials. The EC stores energy in the electrochemical double layer (Helmholtz layer) formed at an electrode/electrolyte interface. The double layer at the electrode surface can form and relax almost immediately, which does not involve chemical reaction. That is why the EC allows the rapid charge and discharge process. Generally, it is believed that the capacitance of an EC works similar to a traditional parallel plate capacitor as equation 2.1, where capacitance,  $C$ , is defined as the amount of electric charge stored,  $q$ , at a given potential,  $V$ . The capacitance is measured in Farads (F) which are equal to one coulomb per volt ( $1 \text{ F} = 1 \text{ C/V}$ ).  $\epsilon_r$  is the relative dielectric constant of the medium between the plates (for a vacuum,  $\epsilon_r = 1$ ), and  $\epsilon_0$  is the permittivity of free space ( $\epsilon_0 \approx 8.854 \times 10^{-12} \text{ F/m}$ ).  $A$  is the surface area ( $\text{m}^2$ ) of the electrodes, and  $d$  is the effective thickness of the electric double layer.<sup>2</sup>

$$C = \epsilon_r \epsilon_0 A/d \quad (2.1)$$

Basically, the capacitance of a single electrode can be estimated if the surface area of carbon is  $1500 \text{ m}^2/\text{g}$  and the double layer capacitance is  $10 \text{ } \mu\text{F}/\text{cm}^2$ .<sup>26</sup> It leads to a specific capacitance of  $150 \text{ F/g}$  for one electrode. For a capacitor with two electrodes, the weight is doubled and the total capacitance of the cell ( $C$ ) is half of an electrode capacitance ( $1/C = 1/C_1 + 1/C_2$ ,  $C_1 = C_2$ ). So the result is the specific capacitance of the cell is  $150/4 = 37.5 \text{ F/g}$  for this example. We can tell the difference between the electrode and cell specific capacitance is a factor of four. It should be noticed that whenever giving specifications for

an EC, one should indicate whether these values are for a single electrode or the whole capacitor cell. In order to get a higher capacitance, the electrode surface area is purposely increased by using porous electrodes with exceptional internal surface.

Fig. 2.3 shows the working principle of an EC loaded with electrolyte, which consists of two high surface area electrodes split by the separator. During the charge process, the positive and negative ionic charges are accumulated on the surfaces of negative and positive electrodes, respectively.<sup>28</sup> The thickness of the double layer depends on the concentration of the electrolyte.

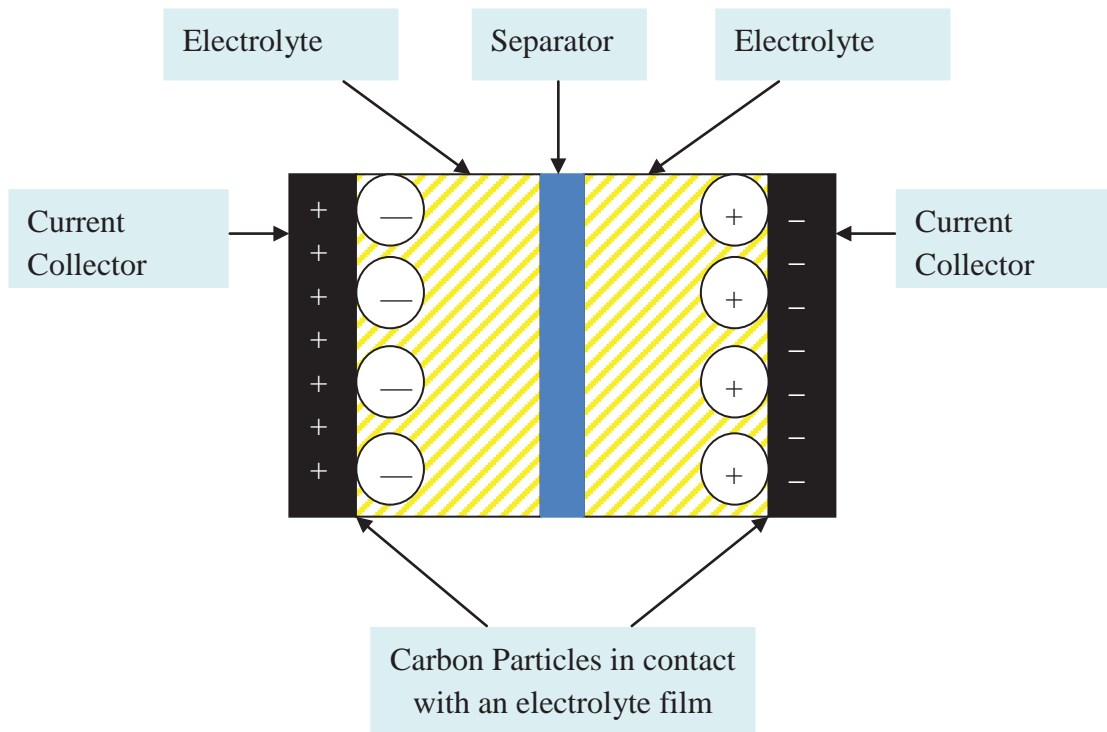


Fig. 2.2. Schematic diagram of a double-layer capacitor showing electrolyte film in contact with carbon particles.

### 2.3.2 Basic Principles of the Asymmetric Electrochemical Capacitor

In recent years, asymmetric or hybrid super capacitor are becoming a trend in ECs. Typically, an asymmetric EC consists of one double layer capacitor electrode and the other

a pseudo-capacitance electrode. By selecting proper electrode materials, an asymmetric EC can achieve a higher working voltage and much higher energy density. The overall capacitance of the series connected capacitor is given by equation 2.2.  $C_T$  is the total capacitance of the cell.  $C_1$  and  $C_2$  are the capacitances of the individual electrodes.

$$\frac{1}{C_T} = \frac{1}{C_1} + \frac{1}{C_2} \quad (2.2)$$

Assume  $C_1$  is the battery electrode involved with the faradic redox reaction, which is more than 10 times than that of  $C_2$ , an active carbon electrode with EC. For example,  $\text{Ni(OH)}_2$ , a substituted cathode for an asymmetric cell, the capacitance of  $\text{Ni(OH)}_2$ ,  $C_1$ , only equals  $1/10 C_2$  in equation 2.2. Obviously, the capacitance of the whole cell is extensively increased (doubled) ( $1/C_T = 1/10 C_2 + 1/C_2$  and  $C_T \approx C_2$ ). In addition, one can tell the asymmetric cell capacitance is controlled by the capacitance of the negative electrode. Fig. 2.4 shows charging and discharging processes of the  $\text{Ni(OH)}_2$ /carbon capacitor.<sup>31</sup>

During the charging process, the anode is the positive electrode, where a change of oxidation stage from the Faradaic process occurs. Equation 2.3 shows the reaction occurring on the positive electrode. The potential of the reaction 2.3 is  $-0.49 \text{ V}$  versus normal hydrogen electrode (NHE).<sup>32</sup> For the negative electrode,  $\text{K}^+/\text{H}^+$  cations from the electrolyte are physically absorbed onto the interface of the negative electrode. The reaction occurred on the negative electrode is shown by equation 2.4. The potential of the reaction 2.4 is  $-0.828 \text{ V}$  versus NHE.<sup>32</sup> The overall charge reaction can be obtained by adding equations 2.3 and 2.4, which gives equation 2.5. The overall potential of the reaction is  $-1.318 \text{ V}$  versus NHE.<sup>32</sup> During the discharge process, the opposite behavior will occur on positive and negative electrodes, respectively.

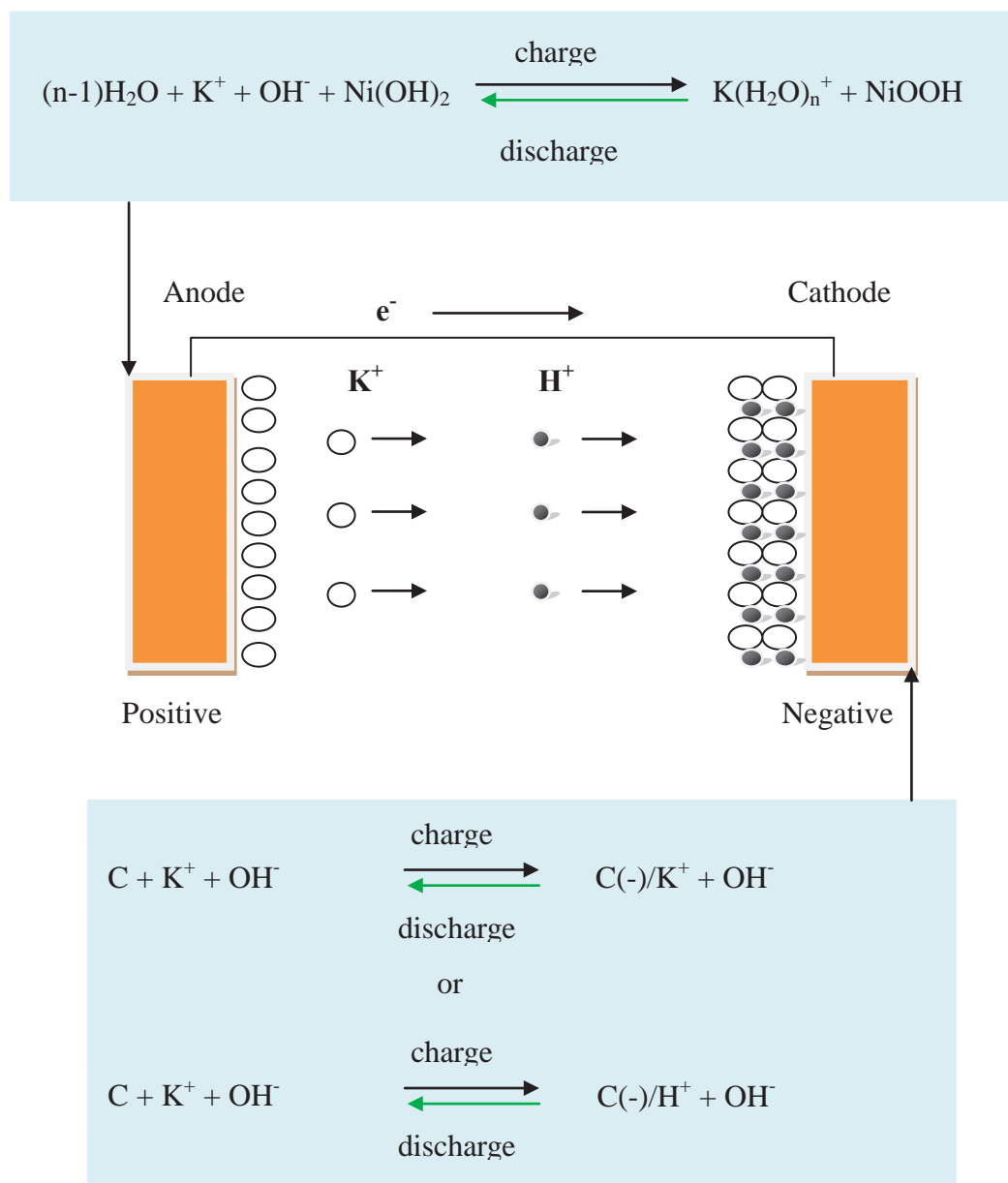
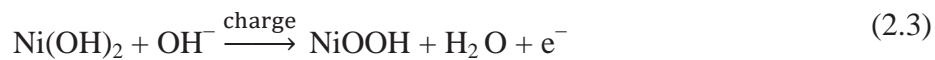


Fig. 2.3. Schematic diagram of ion movement during the charging process (C(-) indicates negative electrons within the surface of carbon electrode).



## 2.4 Ni(OH)<sub>2</sub>/ NiOOH Active Mass Structure

Based on careful Raman and XRD experiments, Cornilsen, *et al.*, have proposed a nonstoichiometric structural model to characterize changes in the nickel hydroxide electrode during cycling (see Fig. 2.5).<sup>33</sup> Fig. 2.5 gives a unique description of nickel hydroxide active mass and the precursors,  $\alpha$ -Ni(OH)<sub>2</sub> or  $\beta$ -Ni(OH)<sub>2</sub>. The structure of the cycled materials differs from the precursor  $\beta$ -Ni(OH)<sub>2</sub>.

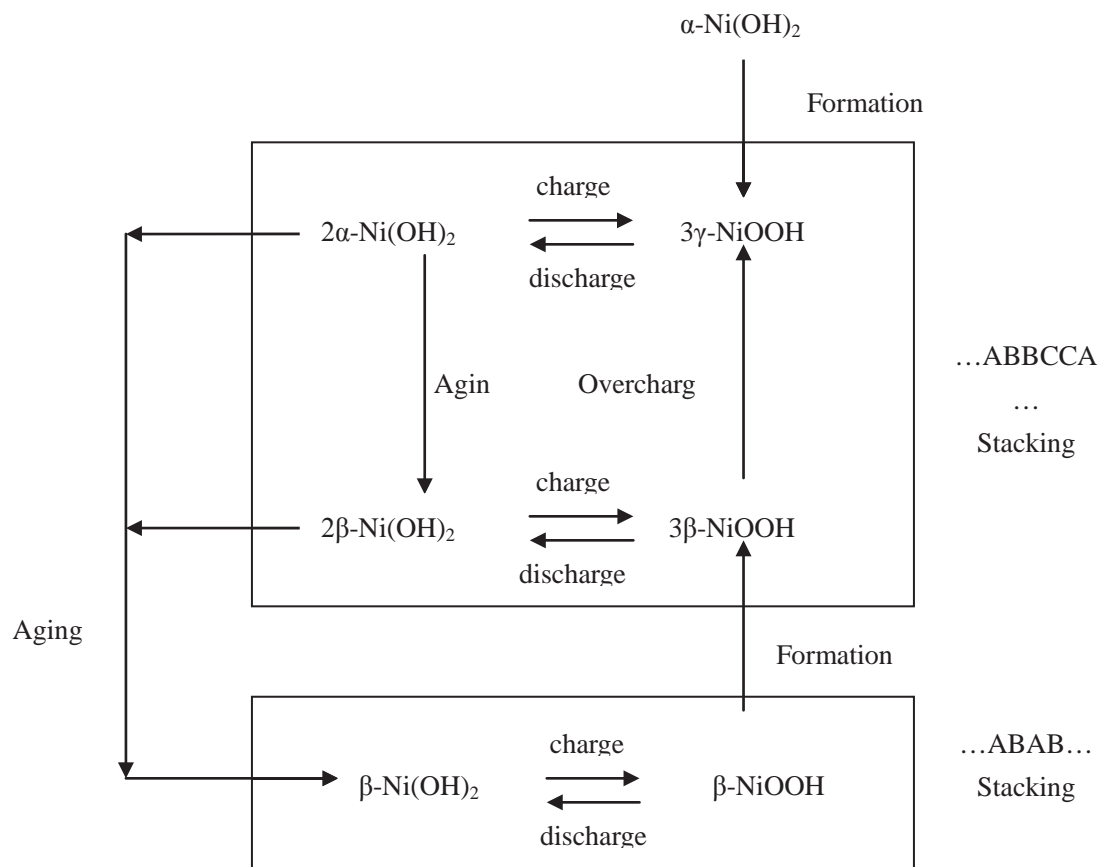


Fig. 2.4. The modified Body diagram.

Traditionally,  $\alpha$ -Ni(OH)<sub>2</sub> has been considered as a close packed, ABAB NiO<sub>2</sub> layer stacking, with water molecules between the NiO<sub>2</sub> layers.<sup>15</sup> The formula is Ni(OH)<sub>2</sub> • 2/3H<sub>2</sub>O. However, the XRD and Raman results are not consistent with this model, and they indicate the  $\alpha$ -Ni(OH)<sub>2</sub> has the same layer stacking as the  $\gamma$ -NiOOH. The

Raman spectra indicate that molecular water of the cathodic- $\alpha$  and chemical- $\alpha$  do exist before cycling.<sup>17-18, 34</sup> Besides, the Raman spectra also show that there are structural differences between the chemical- $\alpha$  and the discharged active mass ( $2\alpha$ ). The O-H stretching modes were seen in the Raman spectra of chemical  $\alpha$ -Ni(OH)<sub>2</sub>.<sup>16,17</sup> But the O-H stretching modes disappeared in Raman spectra of the discharged  $2\alpha$  active mass. This phenomenon suggests that no inter-layer or molecular water exists in the  $2\alpha$  phase.<sup>17-18, 34</sup>

Based on the Raman spectra, XRD patterns, and EXAFS analysis of active mass, Cornilsen, *et al.*, proposed a nonclose-packed structure (with ABBCCA stacking) for the active mass as a solid solution, single phase with a nonstoichiometric structure, [Ni<sub>1-x</sub>(K)<sub>y</sub>(nH)<sub>x-y</sub>]OOH<sub>2-z</sub> (x, y and n can vary). Table 2.3 shows the differences in nickel vacancy content, which result in the differences in electrochemical properties for the  $\alpha/\gamma$  and  $\beta/\beta$  cycles.<sup>35</sup> The defect representations of the undoped Ni(OH)<sub>2</sub> and NiOOH electrode are shown in Fig. 2.5.<sup>34</sup> Aging in aqueous KOH is known to take this active mass back to a disordered  $\beta$ -type material, that is, the ABBCCA stacked material ages to an ABAB stacked material.

Table 2.4.  
Comparison of empirical and nonstoichiometric formulae.<sup>35</sup>

Structural Designation	Typical empirical formula				Ref.	Nonstoichiometric Structure Formula
	Ni	O	H	K		
Ordered $\beta$ -Ni(OH) <sub>2</sub>	1.00	2.00	2.00		18	$\beta$ -Ni(OH) <sub>2</sub>
Disordered $\beta$ -Ni(OH) <sub>2</sub>	1.00	2.35	2.70		18	$\text{Ni}_{0.85}(\text{2H})_{0.15}(\text{OH})_{2.0}$
Cathodic $\alpha$ -Ni(OH) <sub>2</sub>	1.00	3.10	4.20		18	$\text{Ni}_{0.75}(\text{2H})_{0.25}\text{OOH}_{2.0} \cdot 0.33\text{H}_2\text{O}$
2 $\alpha$	1.00	2.67	3.09		<sup>36</sup>	$\text{Ni}_{0.75}(\text{2H})_{0.15}(\text{OH})_{2.1}$
3 $\gamma$	1.00	2.68	1.36	0.33	<sup>37</sup>	$\text{Ni}_{0.75}(\text{2H})_{0.15}(\text{OH})_{1.0}$
2 $\beta$	1.00	2.25	2.25		<sup>36</sup>	$\text{Ni}_{0.89}\text{V}_{0.11}\text{OOH}_{2.0}$
3 $\beta$	1.00	2.24	1.55	0.03	<sup>37</sup>	$\text{Ni}_{0.89}(\text{3H})_{0.08}(\text{K})_{0.03}\text{OOH}_{1.14}$



### Defect Representation of the Nickel Hydroxide Electrode



$$x = \frac{\text{total number of Ni vacancies}}{\text{total number of Ni lattice sites}}$$

$$y = \frac{\text{number of Ni vacancies occupied by K cation}}{\text{total number of Ni lattice sites}}$$

$$N = \frac{\text{number of H cation}}{\text{vacant Ni sites not occupied by K cation}}$$

$$X_w = \frac{\text{number of moles of water}}{\text{number of moles of nickel}}$$

$$2-z = \frac{\text{number of interlamellar protons}}{\text{total number of Ni lattice sites}}$$

Fig. 2.5. Defect representation of Nickel Hydroxide Electrode.

# CHAPTER 3

## METHODS AND CHARACTERIZATION TECHNIQUES

### 3.1 Instruments and Chemicals

An Arbin, 8 channel Potentiostat, MSTAT<sup>\*</sup>, was used to prepare the nickel hydroxide positive electrodes and characterize the electrochemical performance of carbon black symmetric cells and Ni(OH)<sub>2</sub>/carbon asymmetric cells through CV and constant current charge/discharge cycling. A Neslab® temperature bath<sup>†</sup> was employed during the electrochemical deposition of nickel hydroxide. An X-ray diffraction facility of the Scintag XDS2000 powder diffractometer<sup>‡</sup> was employed to characterize the nickel hydroxide electrodes before and during the cycling process. Brunauer-Emmett-Tellet (BET) surface areas of carbon black electrodes were examined by an ASAP2020 apparatus that was made by Micromeritics Instrument Corporation.<sup>§</sup> Carbon foams were obtained by Poco Graphite Inc.<sup>\*\*</sup> Separator materials were provided by Celgard®.<sup>††</sup> The perfluoroalkoxy fluorocarbon (PFA) compression tubes were purchased from McMaster-Carr<sup>‡‡</sup> to set up sealed cells. Stainless steel cylinders were obtained from machine shop of MTU.

Chemicals were purchased from Sigma Aldrich®<sup>§§</sup> Nickel(II) nitrate hexa-hydrate, Ni(NO<sub>3</sub>)<sub>2</sub>·6H<sub>2</sub>O (99% pure); cobalt (II) nitrate hexa-hydrate, Co(NO<sub>3</sub>)<sub>2</sub>·6H<sub>2</sub>O (99% pure); and potassium hydroxide, KOH, 85% pure, were obtained. The 50 wt% ethanol with de-ionized water was used for cleaning the received carbon foams. Carbon black

---

<sup>\*</sup>Arbin Instruments, 762 Peach Creek Cut Off Road, College station, TX-77845

<sup>†</sup>Thermo Fisher Scientific Inc., 81 Wyman Street, Waltham, MA 02454

<sup>‡</sup>Scintag Inc., 10040 Bubbb Road Cupertino, CA 95014

<sup>§</sup>Micromeritics Instrument Corporation, 4356 Communications Dr. Norcross, GA30093

<sup>\*\*</sup>Poco Graphite, Inc., 300 Old Greenwood Rd., Decatur, Texas 76234

<sup>††</sup>Celgard, LLC, 13800 South Lakes Dr, Charlotte, NC 28273

<sup>‡‡</sup>McMaster-Carr, 600N County Line Rd, Elmhurst, IL60126

<sup>§§</sup>Sigma Aldrich, PO Box : 14508, St. Louis, MO 63178

(Ketjenblack EC-600JD) was manufactured by Akzo Nobel Coatings Inc<sup>\*</sup>. PTFE, 60 wt. % dispersed in water (DuPont 6C<sup>†</sup>), was used as the binder.

## 3.2 Experiment Method

### 3.2.1 Positive Electrode Preparation for Asymmetric Cells

Positive electrodes used in asymmetric cells were prepared by Jinjin Wang and Matthew B. Chye using the electrochemical deposition method.<sup>32</sup> Carbon foam is a good current collector due to the light-weight, porous, and graphitic nature, which give the good electrical properties and the ability to be used as a current collector. Replacing heavier current collect (nickel plaque) with a low cost and readily available material, carbon foam, can reduce the mass of the asymmetric capacitors.

The following steps were designed and used to prepare nickel hydroxide electrodes: deposition, formation, and cycling (constant current charge/discharge).

#### Deposition

Before the chemical deposition process, Wen Nee Yeo and Matthew B. Chye applied electrochemical pretreatment on carbon foam by reversing the standard connections, which made the working electrode the anode and, counter electrode the cathode.<sup>32</sup> The carbon foam was held in deposition solution (1.8M Ni(NO<sub>3</sub>)<sub>2</sub> and 0.26M Co(NO<sub>3</sub>)<sub>2</sub>) for 45 minutes at a current density of 55 mA/cm<sup>2</sup>.

*Experimental Procedure for Deposition:* The carbon foams were sonicated for 30 minutes in 50 wt% ethanol aqueous solution. The deposition solution was prepared with 1.8 M Ni(NO<sub>3</sub>)<sub>2</sub> and 0.26M (12.5 wt%) Co(NO<sub>3</sub>)<sub>2</sub> in a 200 ml flask in a 45% ethanol aqueous

---

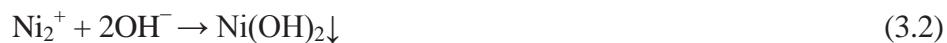
<sup>\*</sup> Akzo Nobel Coatings Inc, 20 Culvert Street, Nashville, Tennessee TN 37210

<sup>†</sup> Dupont, 1007 Market Street Wilmington, DE 19898

solution (0.87/0.13 mole ratio, Co/Ni). The temperature bath was set as 70°C during the deposition process. Two nickel plates were used as the counter electrodes. A 1cm thick, high density polypropylene plate was used (as designed by Matthew B. Chye) to hold the relative positions of the two counter electrodes on either side of the positive with the grooves in its surface.<sup>32</sup> A 250 ml translucent and chemically resistant polypropylene jar was used to assemble the flooded cell.<sup>31</sup> Fig. 3.1 shows the flooded cell and propylene plate.

The level of nickel hydroxide loaded into carbon foam can be indicated by the changing potential during an electrochemical deposition (see Fig.3.3). Generally, the deposition process is fully achieved when a constant voltage is reached. However, at that state, the surface and pores will be fully covered by the deposited nickel hydroxide, which is not favorable for cycling. For this reason, a cut off voltage (lowest) for deposition of -2.5 V is used. A constant current was applied for each nickel hydroxide deposition. Typically, the current densities are 50-100 mA/cm<sup>2</sup>. Fig. 3.2 shows a typical deposition voltage profile.

After deposition with nickel hydroxide, carbon foam was removed from the flooded cell and washed with de-ionized water, to remove the surface solution on the electrode. This washed electrode was ready for the next step – the formation process. During this electrochemical deposition, reactions 3.1 and 3.2 are involved.



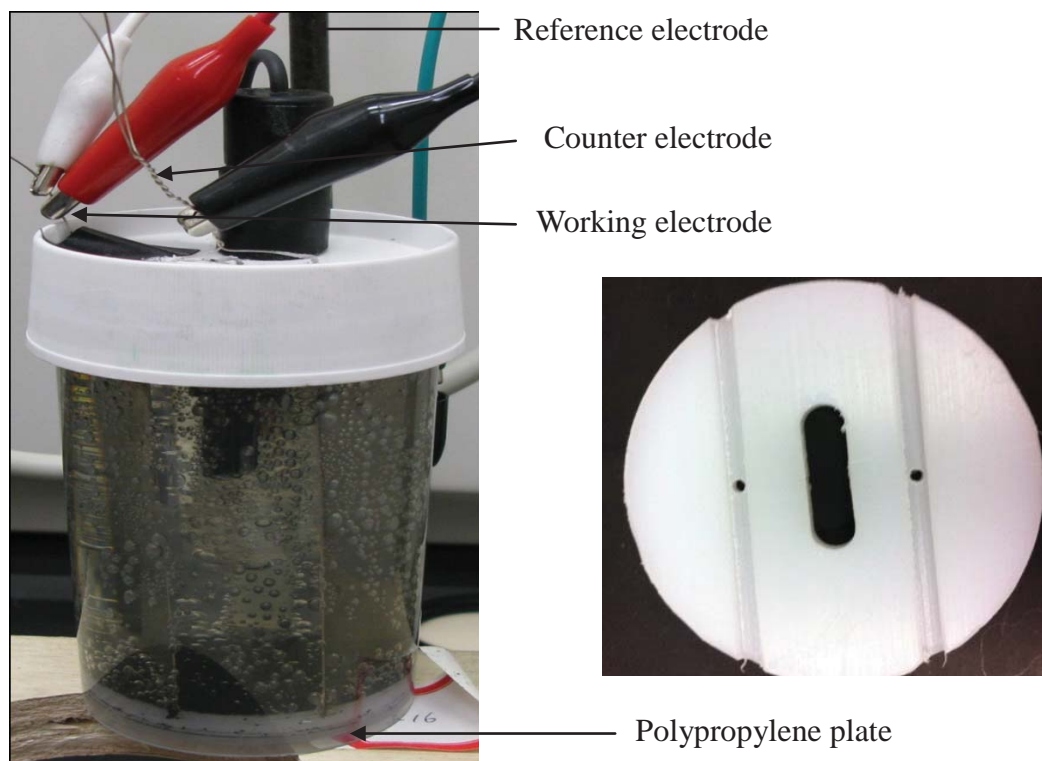


Fig. 3.1. Example of flooded cell (photos by the M. B. Chye and author).

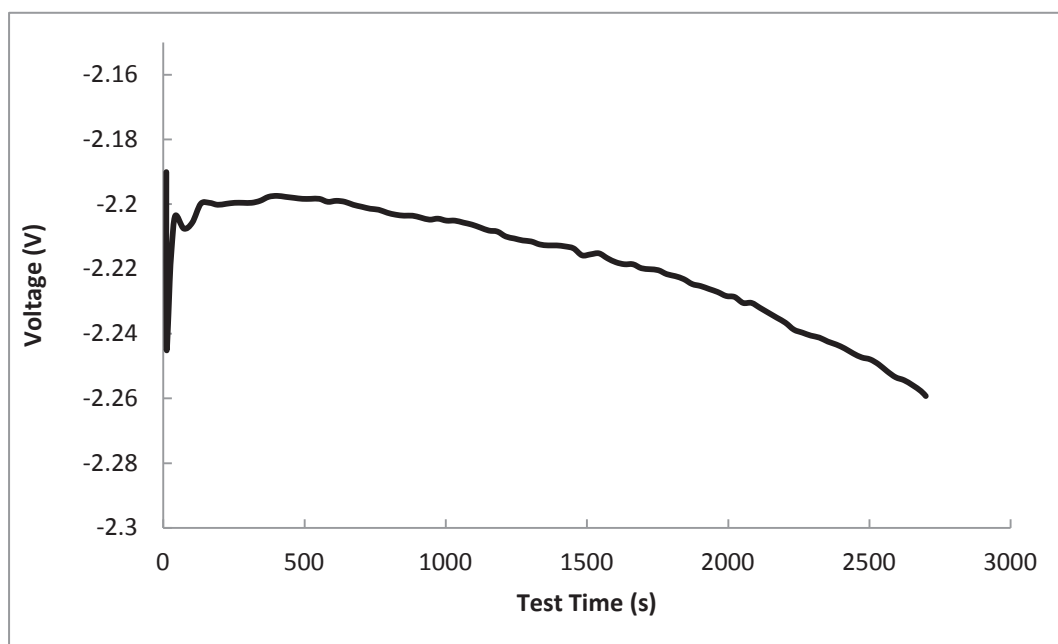


Fig. 3.2. Typical deposition profile ( $100 \text{ mA/cm}^2$ ).



Fig. 3.3. Example of 45 min deposited electrode (photo by M. B. Chye).

### Formation

After the deposition, the formation process was used to bring the active material up to the full capacity by the repeated oxidation-reduction. This process is the charge/discharge cycling process and will bring the deposited active mass up to the ultimate, stable performance. Besides, the formation process will remove loosely adhered particles as well as the impurities (*e.g.*, nitrate) from the deposition.

*Experimental Procedure for Formation:* The electrolyte solution was 26 wt% KOH. The reference electrode (Hg/HgO with 20 wt% KOH) was used during the cycling. There were in total 5 cycles included for the formation process, which were typically necessary to achieve a standard charge/discharge profile. The current densities were 70 mA/cm<sup>2</sup> for the first cycle and 20 mA/cm<sup>2</sup> for the following four cycles. The potential was used to indicate the level of charging and discharging. Once the constant voltage was reached during the charging process, the cell would be forced to start discharge process. Typically, the cut off voltage (highest) is 0.606 V for the current density of 70 mA/cm<sup>2</sup> and 0.505 V for 20 mA/cm<sup>2</sup>. Fig. 3.4 shows a complete formation process of an electrode. During this process, overcharging needs to be avoided to prevent the generation of oxygen.

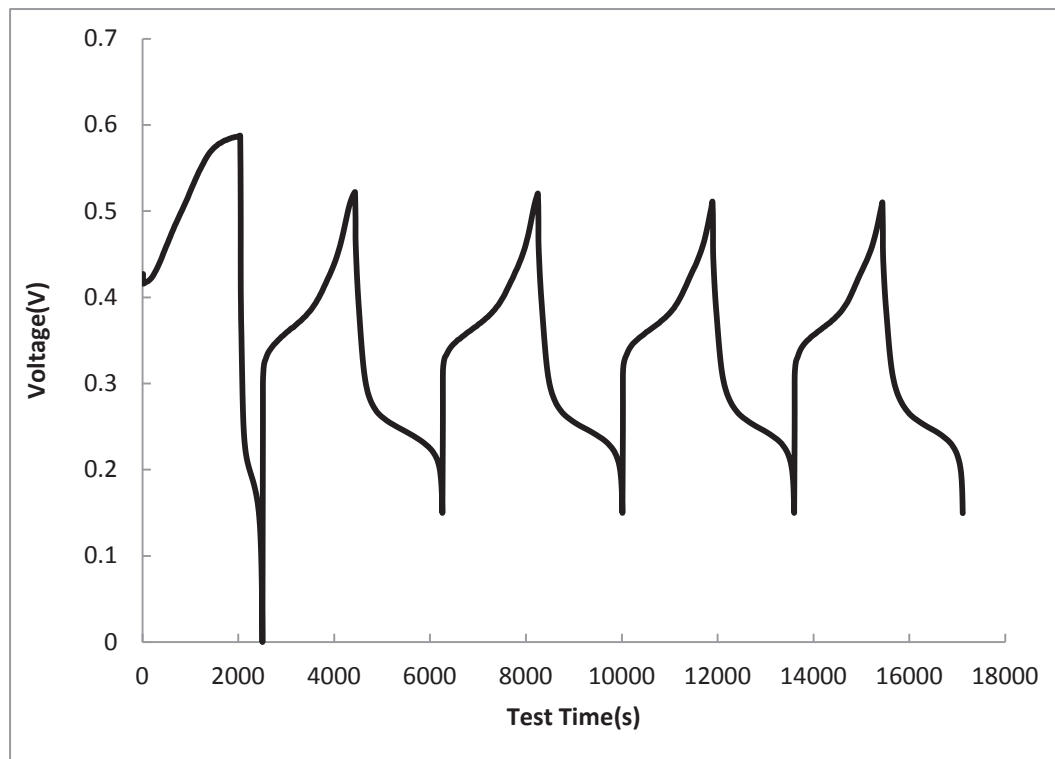


Fig. 3.4. Voltage profile of the formation process for a nickel hydroxide electrode relative to a Hg/HgO reference electrode.

### 3.2.2 Negative Electrodes Preparation and Characterization

Carbon black (Ketjenblack, EC-600JD) was selected and used to prepare the negative electrode due to its high conductivity and low resistance. In this study, the hand-made method was used to prepare the carbon black electrode. PTFE was used as the binder to hold carbon black particles together. The electronic resistance was conducted by Dr. Julia A. King. Heating process was employed in order to soften the mixture of carbon black and PTFE. Ethanol was used to increase the adhesiveness of carbon materials. Isopropanol was applied to enhance the flexibility of the carbon. Fig.3.5 shows the negative electrodes. The negative electrodes were made in a series of different proportions of carbon black and PTFE, as shown in Table 3.1. The electrochemical performance of these carbon black electrodes was examined using assembled symmetric cells (see section 4.1).



Fig. 3.5. Carbon black electrodes (3 wt% PTFE/CB and 97% Ketjenblack, EC-600JD) (photo by the author).

*Experimental Procedure for Negative Electrode Preparation:* The carbon black and PTFE are weighed based on the composition. Then mix these two materials together in a mortar. Grind the mixture until the PTFE is well dispersed in the carbon black powder. After grinding, the mortar is placed in the oven at 120°C for 30 minutes. The contents are taken out and ground again for 15 minutes. The 30 minutes heating and 15 minutes grinding process are repeated 3 times. Then 3 ml of isopropanol and 3 ml of ethanol were added to the mixture to aid the dough formation. The dough was flattened by a glass rod. Circular electrodes were punched out from the sheet and then dried in a vacuum for two hours remove alcohol.



Table 3.1.  
A series of negative electrodes.

<b>Batch Number</b>	<b>PTFE/Carbon wt%</b>	<b>Distribution</b>
B1	5%	Neg. electrodes for Matt Chye asymmetric cell (SW63)
B2	3%	BET surface area tests
B3	3%	Neg. electrodes for Jinjin Wang asymmetric cells J1 and J2; Electrodes for Jinjin Wang symmetric cell
B4	5%	Neg. electrodes for Matt Chye asymmetric cell (SW66) Electrodes for Jinjin Wang symmetric cell BET surface area test
B5	3%	Neg. electrodes for Jinjin's asymmetric cell J3
B6	5%	Electrodes for Jinjin's symmetric cell
B7	10%	Electrodes for P. Sasthan Kuttipillai symmetric cell Neg. electrodes for asymmetric cell for P. Sasthan Kuttipillai
B8	5%	Electrodes for Jinjin Wang symmetric cell

### 3.3 Assembly of Symmetric and Asymmetric Cells

All electrodes and separators were soaked in 26 wt% KOH for three days. After this treatment, symmetric and asymmetric cells were assembled using the PFA Swagelok-type fittings, and their electrochemical performance was characterized. Fig. 3.6 shows an assembled Swagelok cell. Table 3.2 shows the components used in these cells. A short circuit between the electrodes should be avoided in the assembling process. Stainless steel plates defined size and thickness were employed as current collectors (CC) for these cells

between each electrode and stainless steel cylinder.



Fig. 3.6. Swagelok cell connected for charge-discharge cycling (photo by the author).

Table 3.2.  
Components of symmetric and asymmetric cells.

Cell Number	Cells	<u>Components</u>
		<u>From left to right side</u>
1	Sym. 3 wt%	CC/ B3 neg./1 layer separator/ B3 neg./CC
2	Sym. 5 wt%	CC/ 2 layers of B4 neg./1 layer separator/ 2 layers of B4 neg./CC
J1	Asym. 3 wt% J1	CC/ 2 layers of B3 neg./2 layers separator/pos./CC
J2	Asym. 3 wt% J2	CC/ 2 layers of B3 neg./2 layers separator/pos./CC
J3	Asym. 3 wt% J3	CC/ 2 layers of B5 neg./2 layers separator/pos./CC

### 3.4 Symmetric and Asymmetric Cells Characterization

The capacitance behaviors of the 3 wt% and 5 wt% PTFE/CB symmetric cells were investigated by cyclic voltammetry using the Arbin MSTAT, respectively. The scan rates were varied from 1 to 100 mV/s, and the potential window was between  $-1$  V and  $+1$  V.

The integral capacitances of the symmetric and asymmetric cells, and their life stability were measured by charge/discharge experiments at a constant current density between  $5 \text{ mA/cm}^2$  to  $50 \text{ mA/cm}^2$  in 26 wt% KOH. The specific capacitance, energy density, and power density were calculated according to the equations 3.1 to 3.4. Where  $C$  is the system capacitance of a cell;  $V$  is the total voltage applied to the cell and  $\Delta V$  equals to  $V_{\max}$  substrates  $V_{\min}$ ;  $m$  is the total weight of both positive and negative electrodes.

$$\text{Capacitance} = \frac{\int i \Delta t}{\Delta V} = \frac{Q}{\Delta V} \quad (\text{F}) \quad (3.1)$$

$$\text{Specific capacitance} = \frac{C}{m} \quad (\text{F/g}) \quad (3.2)$$

$$\text{Energy Density} = \frac{1}{2} C (V_2^2 - V_1^2) \quad (\text{W} \cdot \text{h/kg}) \quad (3.3)$$

$$\text{Power Density} = \frac{\text{Energy Density}}{t} \quad (\text{W/kg}) \quad (3.4)$$

### 3.5 XRD Characterization of the Positive Electrodes

XRD is an extremely important tool to analyze the structure of solid materials. XRD can provide information about the crystal lattice of a material and characterize the crystalline phases present. The crystal structure defines the number of peaks, the peak positions ( $2\theta$ ), and the relative intensities. Peak positions are controlled by the

inter-atomic distances (d-spacing) and fractional coordinates. Peak intensities are determined by the arrangement of the atoms and peak overlap. XRD requires long range order in the lattice, and a reduction in symmetry (*e.g.*, disorder) can reduce the intensities as peaks are broadened. For example, amorphous materials often present a single broad band. Cation vacancies or layer stacking disorder can broaden peaks and reduce peak intensities. The observed powder pattern is often a sum of broadened, over-lapping peaks.

The XRD patterns can be predicted theoretically, and then compared with the experimental ones. Even though XRD patterns are weakened or broadened by the disorder, structural information can be extracted. Peak broadening can be predicted by an empirical formula and varied to fit the experimental pattern. The calculation of the XRD powder pattern can be conducted by assuming a structural model (space group, lattice parameters, fractional coordinates, and thermal parameters) and by defining peak broadening as a function of  $2\theta$  (half-width is defined at two experimental  $2\theta$  positions). The proposed structural model will be supported by good agreement between calculated and experimental patterns.

### 3.5.1 XRD Sample Preparation

Six nickel electrodes supported by the carbon foams were electrochemically prepared as the same procedures as chapter 3, section 1. A current density of  $10 \text{ mA/cm}^2$  was used for the constant current charge/discharge of the electrodes. All samples characterized by XRD are described in Table 3.3.

Table 3.3.  
Electrodes used for XRD characterization.

<b>Samples Number</b>	<b>Electrochemical State</b>	<b>Preparation</b>
a	As deposition	Washed and dried after deposition.
b	As formed	Washed and dried after formation process.
c	Charged, cycle 1	The electrode was charged once after formation, stopped, and dried.
d	Discharged, cycle 1	The electrode was cycled once after formation, stopped after the first discharge, and dried.
e	Charged, cycle 10	The electrode was cycled 9 times after formation, stopped after the 10 <sup>th</sup> charge, and dried.
f	Discharged, cycle 10	The electrode was cycled 10 times after formation, stopped after the 10 <sup>th</sup> discharge, and dried.

### 3.5.2 XRD Powder Pattern Collection

XRD powder patterns were collected on the Scintag XDS2000 powder diffractometer and Cu K $\alpha$  at 1.540562Å at Michigan Technological University. XRD powder patterns were collected over a range of 2° to 85° 2 $\theta$  under the operation condition at 45 KeV and 35 mA. XRD samples were measured by put the whole nickel electrodes supported by carbon foam onto the rectangular glass slide. The step size and rest time were 0.03° 2 $\theta$  and 2 seconds for all the samples.

### 3.5.3 XRD Powder Pattern Calculation

A program from the online Database of Zeolite Structures was used to calculate the XRD powder patterns; it has been approved by the Structure Commission of the International Zeolite Association (IZA-SC).<sup>38</sup> This program calculates peak positions, intensities, and a theoretical pattern. The overlap of adjacent peaks, which causes peak broadening, can be defined by the half-width ( $2\theta$  dependence). By adjusting the variable (half-width), there will be a good match between experimental and calculated XRD powder patterns. The calculated pattern can be exported into the ASCII file, which then is plotted using Microsoft EXCEL. Powder pattern indexing has been done using the LSQ82 program written by Hubbard, *et. al.*<sup>39</sup>

## CHAPTER 4

### RESULTS

#### 4.1 Electrochemical Characterization of Symmetric Capacitors

##### 4.1.1 Cyclic Voltammetry Measurements

For the 3 wt% symmetric cell, 1 layer of carbon black sheet (B3<sup>\*</sup>) was used for each electrode. The sheet had a diameter of 1.839 cm and a mass of 0.0549 g. The area for the electrode was 2.656 cm<sup>2</sup>. The scan rates of 1 mV/s, 5 mV/s, 10 mV/s, 25 mV/s and 100 mV/s were employed to investigate the CV performance. Fig. 4.1 shows the potential vs. current response of the cell. Table 4.1 summarizes the specific capacitance, as well as the columbic efficiency. The calculations of specific capacitances for electrode materials were based on equations 3.1 and 3.2, where the discharge capacity was obtained from the Arbin file and  $\Delta V$  is equal to 2V in this case.

The 5 wt% symmetric cell had 2 layers of carbon black sheets (B4<sup>\*</sup>) in each electrode. Each layer of these sheets had a diameter of 1.839 cm and a mass of 0.0300 g. The area for this electrode was 2.656 cm<sup>2</sup>. The same scan rates were used to investigate the CV performance. Fig. 4.2 shows the potential vs. current response of the cell. Table 4.2 summarizes the specific capacitance and columbic efficiency using equation 3.1 and 3.2.

---

<sup>\*</sup>Batch B3 and B4, See Table 3.2

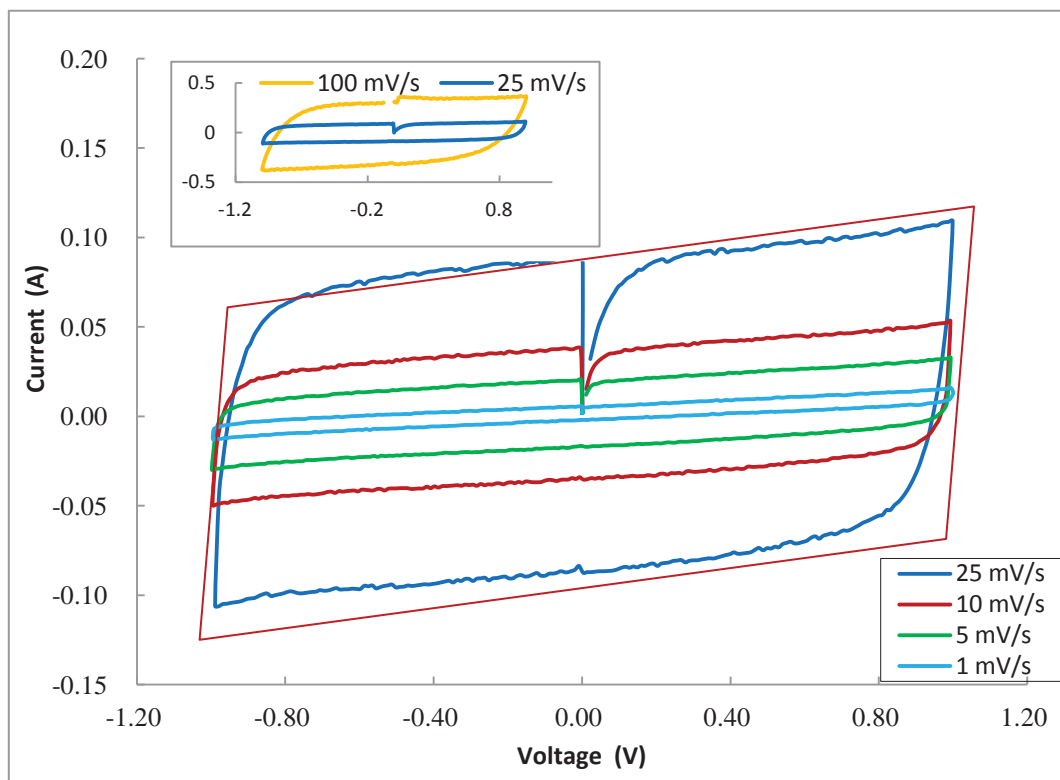


Fig. 4.1. CV plot obtained at different scan rates in the 3 wt% symmetric capacitor (Swagelok-type PFA cell, Celgard 3501 separator, 3 wt% PTFE/CB).



Table 4.1.  
Cell specific capacitance and columbic efficiency calculated for the 3 wt% symmetric capacitor, at five different CV scan rates (same cell as Fig. 4.1).

<b>Scan Rate (mV/s)</b>	<b>Charge Cap. (F)</b>	<b>Discharge Cap. (F)</b>	<b>Single Electrode Specific Cap. (F/g)</b>	<b>Columbic Efficiency (%)</b>
1	11.90	8.02	146.14	67.4
5	8.06	6.66	121.26	82.6
10	7.44	6.75	123.01	90.7
25	6.89	6.58	119.93	95.5
100	5.77	5.78	105.23	100.2

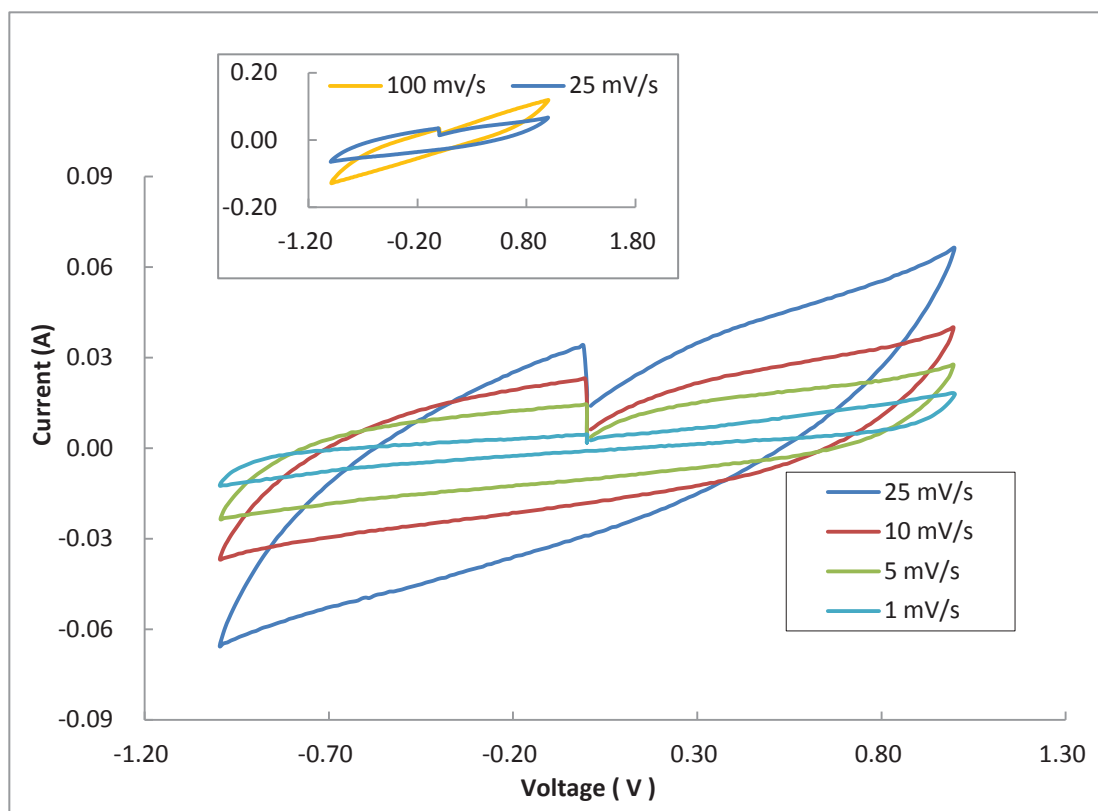


Fig. 4.2. CV plot obtained at different scan rates in the 5 wt% symmetric capacitor (Swagelok-type PFA cell, Celgard 3501 separator, 5 wt% PTFE/CB).

Table 4.2.  
Cell specific capacitance and columbic efficiency calculated for the 5 wt% symmetric capacitor, at five different CV scan rates (same cell as Fig. 4.2).

<b>Scan Rate (mV/s)</b>	<b>Charge Cap. (F)</b>	<b>Discharge Cap. (F)</b>	<b>Single Electrode Specific Cap. (F/g)</b>	<b>Columbic Efficiency (%)</b>
1	8.88	5.97	99.6	67.3
5	6.18	4.46	74.3	72.1
10	4.48	3.78	62.9	84.2
25	2.84	2.66	44.4	93.9
100	1.26	1.19	19.9	94.5

#### 4.1.2 Constant Charge / Discharge Cycling

Constant current charge/discharge cycling was used to investigate the capacitance performance of carbon black electrodes during the cycling process. The constant cycling was conducted between 1V to 0 V for the symmetric cells. For the 3 wt% symmetric cell, 30.0 mA/cm<sup>2</sup> current density was selected to characterize the cell. The potential vs. time response of this cell is shown in Fig. 4.3. Fig.4.4. compares the potential vs. time response of the 1<sup>st</sup> and the 300<sup>th</sup> cycles during the cycle life test. Fig. 4.5.shows the discharge capacity and efficiency vs. function of cycle number over 300 cycles.

The current density of 18.8 mA/cm<sup>2</sup> was applied to characterize the 5 wt% symmetric cell. Fig. 4.6 shows the potential vs. time response of the 5 wt% cell and Fig.4.7 compares the potential vs. time response of the 1<sup>st</sup> and the 300<sup>th</sup> cycles during the cycle life

test. The discharge capacity and efficiency vs. function of cycle number over 300 cycles is shown in Fig. 4.8.

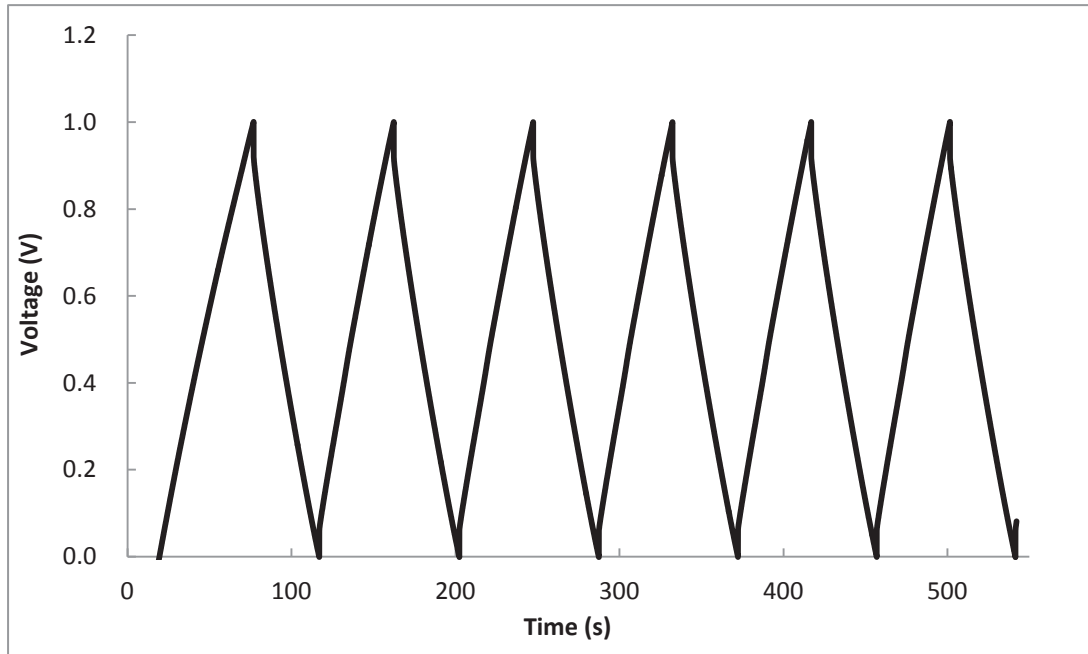


Fig. 4.3. Potential vs. time response of the 3 wt% symmetric capacitor at  $30.0 \text{ mA/cm}^2$  current density for first 6 cycles (same cell as Fig. 4.1).

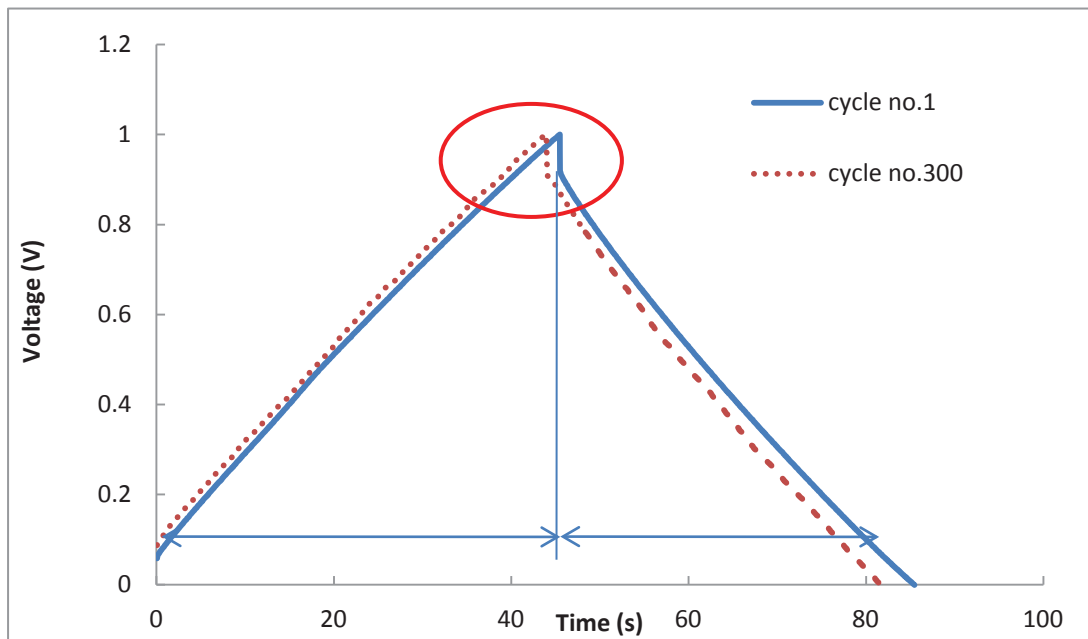


Fig. 4.4. Potential vs. time response for the 3 wt% symmetric capacitor at 1<sup>st</sup> and 300<sup>th</sup> cycle numbers with  $30.0 \text{ mA/cm}^2$  current density (same cell as Fig. 4.1).

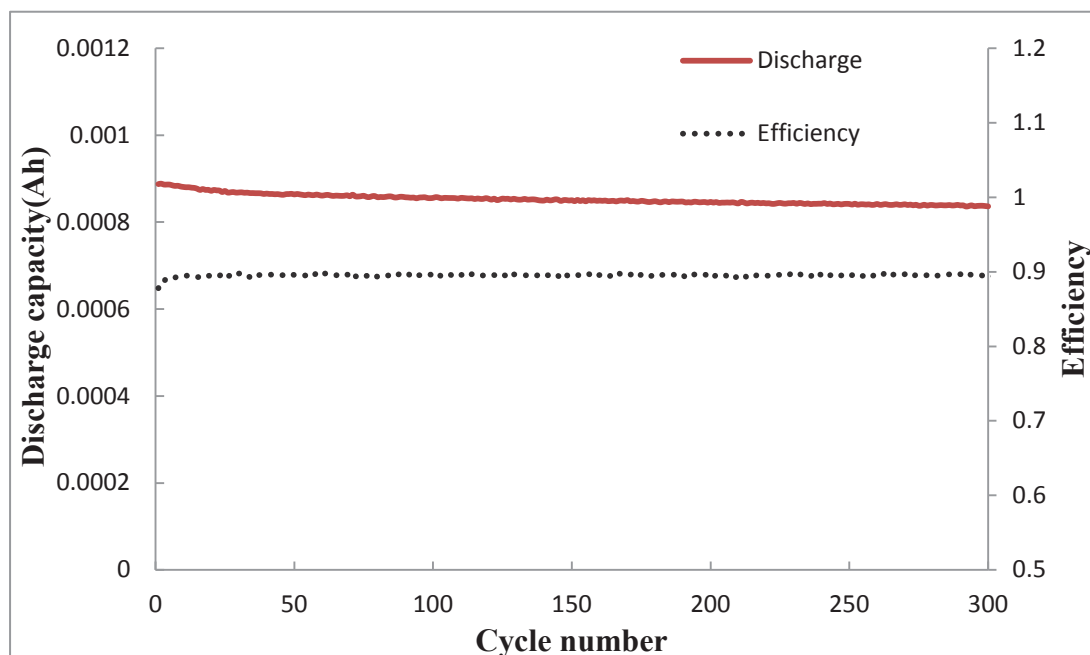


Fig. 4.5. The discharge capacity and efficiency vs. function of cycle number of the 3 wt% symmetric capacitor at  $30.0 \text{ mA/cm}^2$  over 300 cycles (same cell as Fig. 4.1).

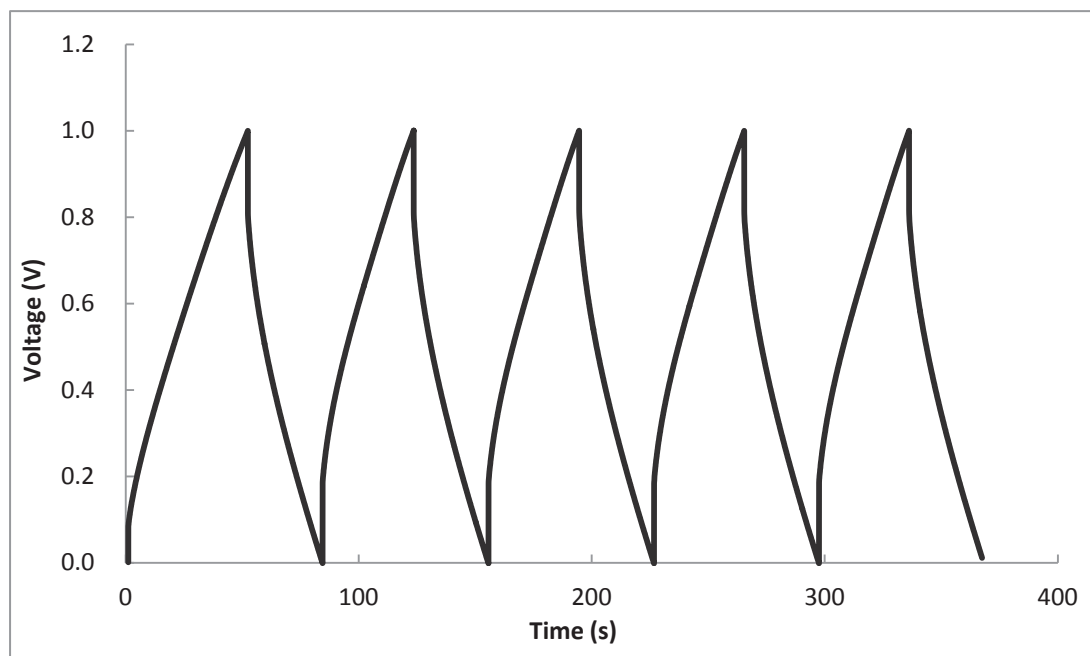


Fig. 4.6. Potential vs. time response of the 5 wt% symmetric capacitor at  $18.8 \text{ mA/cm}^2$  current density for first 5 cycles (same cell as Fig. 4.2).

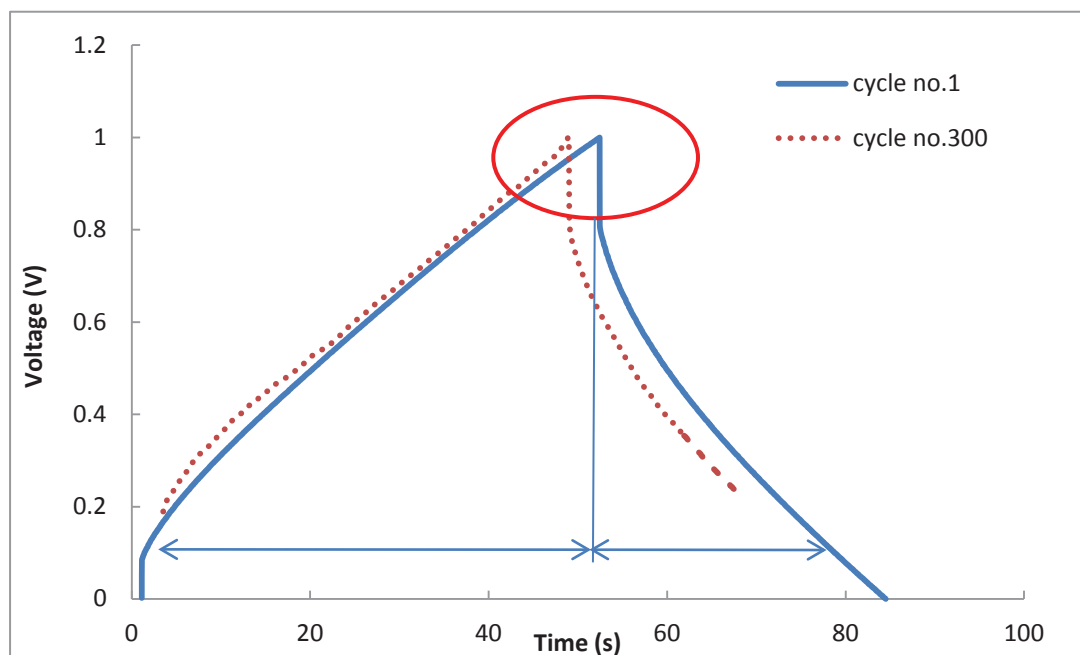


Fig. 4.7. Potential vs. time response for the 5 wt% symmetric capacitor at 1<sup>st</sup> and 300<sup>th</sup> cycle numbers with 18.8 mA/cm<sup>2</sup> current density (same cell as Fig. 4.2).

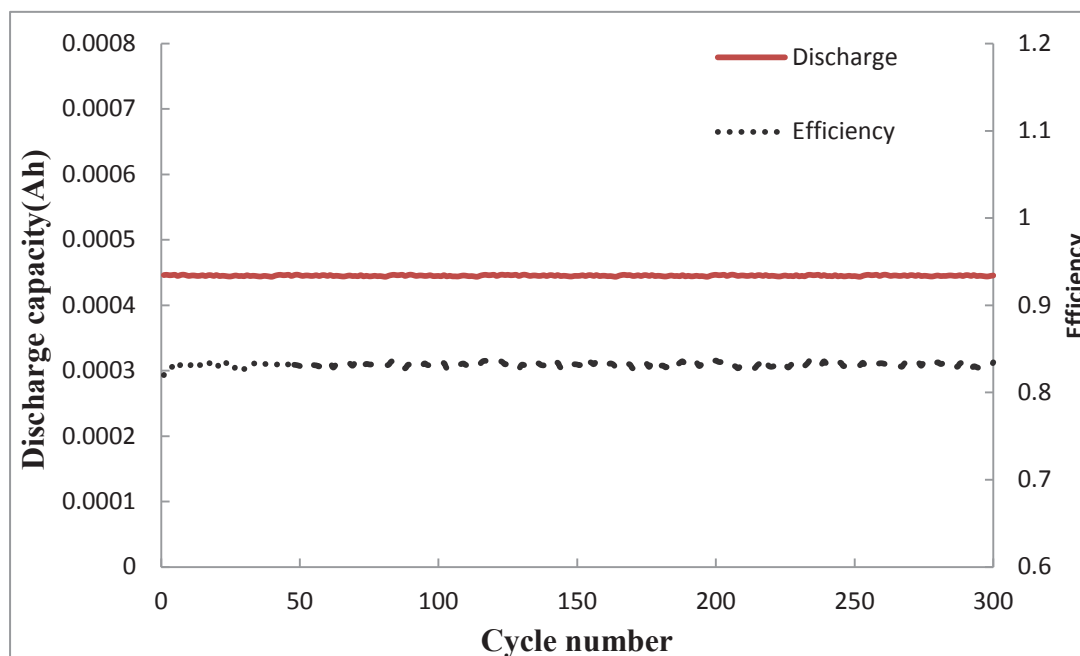


Fig. 4.8. The discharge capacity and efficiency vs. function of cycle number of the 5 wt% symmetric capacitor at 18.8 mA/cm<sup>2</sup> over 300 cycles (same cell as Fig. 4.2).

### 4.1.3 Comparison of CV and Cycling Performance

Fig. 4.9 compares the CV performance of the 5 wt% symmetric cell with the 3 wt% cell at 100 mV/s scan rate. Table 4.3 summarizes the capacitance, specific capacitance, energy density, and power density for the 3 wt%, 5 wt%, and 10 wt% symmetric cells (The data of the 10 wt% was obtained from P. Sasthan Kuttipillai).<sup>40</sup> Fig. 4.10 shows a Ragone plot for the 3 wt%, 5 wt%, and the 10 wt% cells. Energy density and power density were calculated using equations 3.3 and 3.4, where the average discharge time was 38.4 s and 32.0 s for the 3 wt% and 5 wt% symmetric cells, respectively.

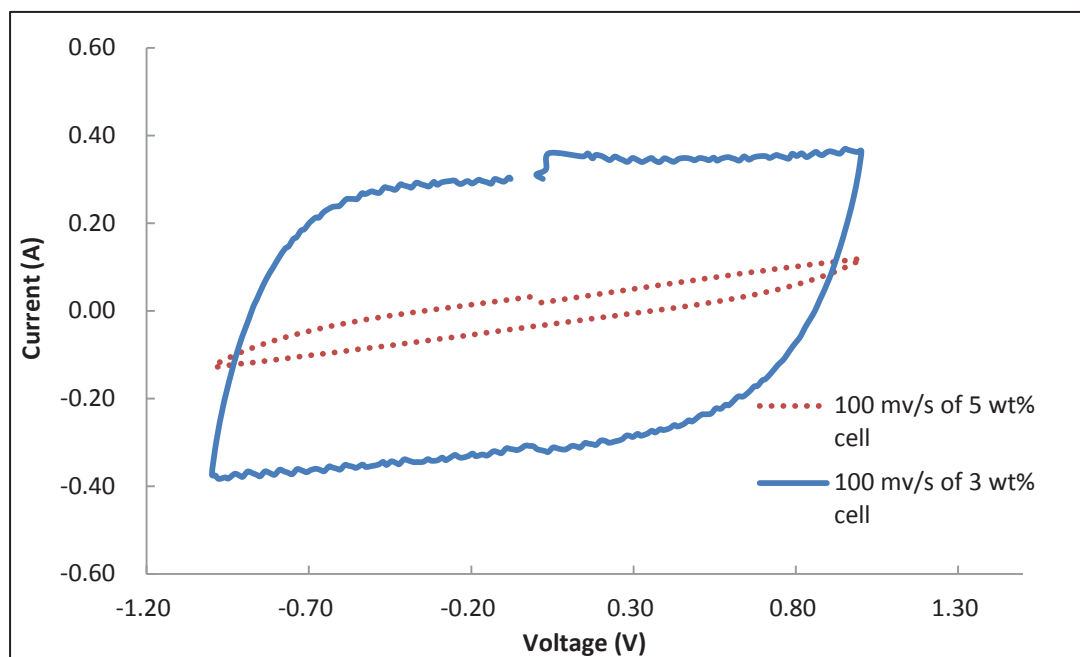


Fig. 4.9. Comparison of the CV performance of the 3 wt% and 5 wt% symmetric cells at the 100 mV/s scan rate.

Table 4.3.

Comparison of cell specific capacitances, energy, and power densities for the 3 wt%, 5 wt% and 10 wt% symmetric capacitors (data shown are average over 300 cycles for the 3 wt% and 5 wt% cells).<sup>40</sup>

<b>Cell</b>	<b>Charge Cap. (F)</b>	<b>Discharge Cap. (F)</b>	<b>Single Electrode Specific Cap. (F/g)</b>	<b>Columbic Efficiency (%)</b>	<b>Energy Density (Wh/kg)</b>	<b>Power Density (W/kg)</b>
3 wt%	3.43	3.07	121.8	89.5	6.44	604.1
5 wt%	1.93	1.60	66.7	83.1	2.39	269.2
10 wt% <sup>†</sup>	0.858	0.756	10.1	88.1	0.774	3.68

<sup>†</sup> from P. Sasthan Kuttipillai best performing 10 wt% symmetric cell at 0.35 mA/cm<sup>2</sup>.<sup>40</sup>



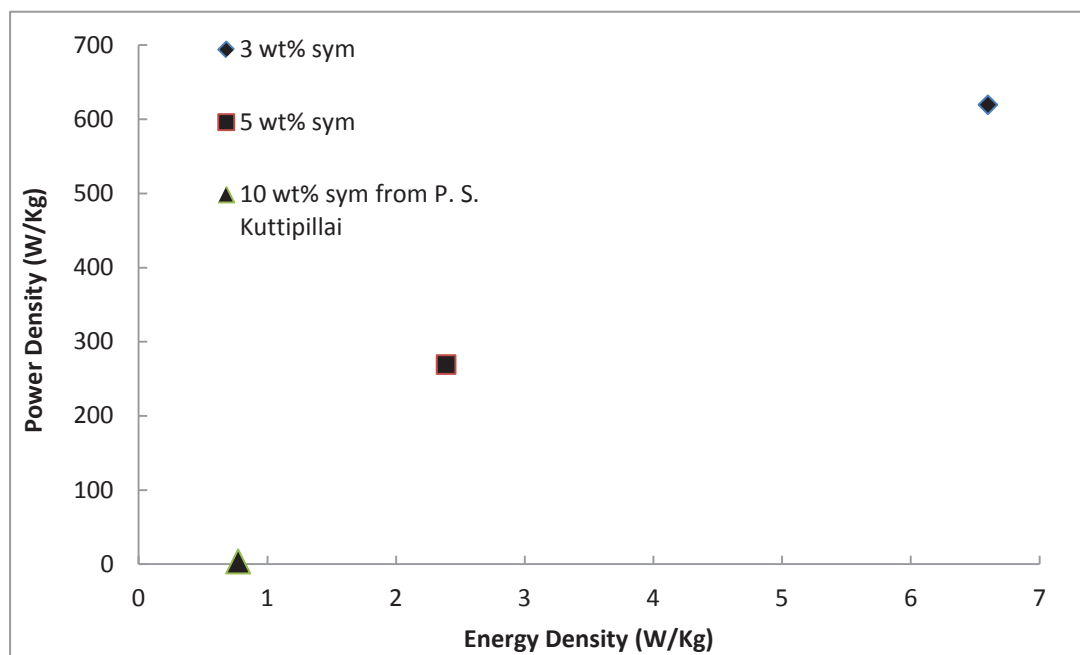


Fig. 4.10. Ragone plot for the 3 wt%, 5 wt%, and 10 wt% symmetric capacitors.

## 4.2 BET Surface Area and Resistivity Measurements for Negative Electrodes

The BET surface areas of PTFE/CB electrodes were determined by the measurements of N<sub>2</sub> adsorption/desorption isotherms at 77K. Table 4.4 shows the BET surface area of the 3 wt%, 5 wt%, and 10 wt% PTFE/CB electrodes (BET surface area of the 10 wt% electrode was tested by Wen Nee Yeo).<sup>41</sup> The 3 wt% and 5 wt% PTFE/CB electrodes are from batches B2 and B4, respectively (see Table 3.2).

Table 4.4.  
BET surface areas of 3 wt% and 5 wt% PTFE/CB electrodes.

<b>Electrodes</b>	<b>Sample Mass (g)</b>	<b>BET m<sup>2</sup>/g</b>	<b>Single point surface area at P/Po (m<sup>2</sup>/g)</b>
3 wt% PTFE/CB	0.0216	1239	1295
5 wt% PTFE/CB	0.0202	1237	1198
10 wt% PTFE/CB*	-	967	-

\* from Wen Nee Yeo.<sup>41</sup>

The effective resistivity (ER) of the 3 wt%, 5 wt% and 10 wt% PTFE/CB sheets was measured on four bars which were cut sheets from batches B3 (3 wt%), B4 (5 wt%) and B7 (10 wt%), respectively. (see Table 3.2) This measurement was accomplished by Dr. Julie King (2-probe ER test, Keithley 2400 source meter, Ag on ends). Table 4.5 displays the ER test results for 3 wt%, 5 wt% and 10 wt% PTFE/CB sheets. Fig. 4.11 depicts ER as a function of the PTFE/CB wt%. Fig. 4.12 shows the energy density and power density as a function of the ER for the 3 wt%, 5 wt% and 10 wt% cells. The ER was calculated using equation 4.1, where  $\Delta V$  is the voltage applied to the bar; W is the width, T is the thickness and L is the length of the bar; i is the current flowing through the circuit when  $\Delta V$  was applied to the bar.

$$ER = (\Delta V * W * T) / (i * L) \quad (4.1)$$

Table 4.5.

Effective resistance, ER for 3 wt%, 5 wt% and 10 wt% PTFE/CB electrodes at  $\Delta V = 0.0010$  V.

Sample	Length (mm)	Width (mm)	Thickness (mm)	Volts (V)	Microamps ( $\mu$ A)	Resistance (ohm/cm)
97% CB    3% PTFE    6-4-2010						
1	19.06	2.00	2.04	0.001	55	0.389
2	19.45	1.73	2.12	0.001	56	0.337
3	18.57	2.10	2.09	0.001	63	0.375
4	19.06	1.75	1.96	0.001	52	0.346
Average ER						0.3618
95% CB    5% PTFE    6-27-2010						
1	21.60	2.13	1.92	0.001	48.2	0.3928
2	21.00	2.09	1.71	0.001	47.1	0.3613
3	21.36	2.08	1.80	0.001	44.5	0.3939
4	20.86	1.94	1.75	0.001	37.5	0.4340
5	21.01	2.06	1.80	0.001	48.8	0.3617
Average ER						0.3887
90% CB    10% PTFE    6-27-2010						
1	21.10	2.08	1.63	0.001	45.5	0.3531
2	21.35	2.14	1.60	0.001	44.0	0.3645
3	21.16	2.28	1.59	0.001	31.0	0.5527
4	21.61	2.14	1.81	0.001	40.5	0.4426
5	21.53	2.17	1.70	0.001	49.0	0.3497
Average ER						0.4125

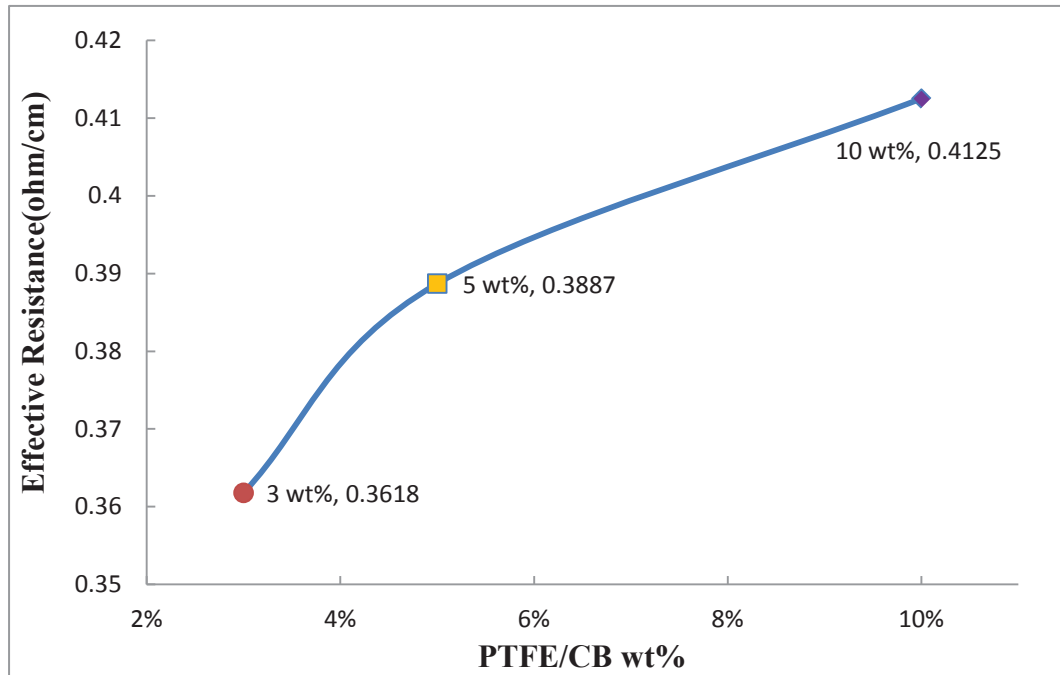


Fig. 4.11. ER as a function of the PTFE/CB wt%.

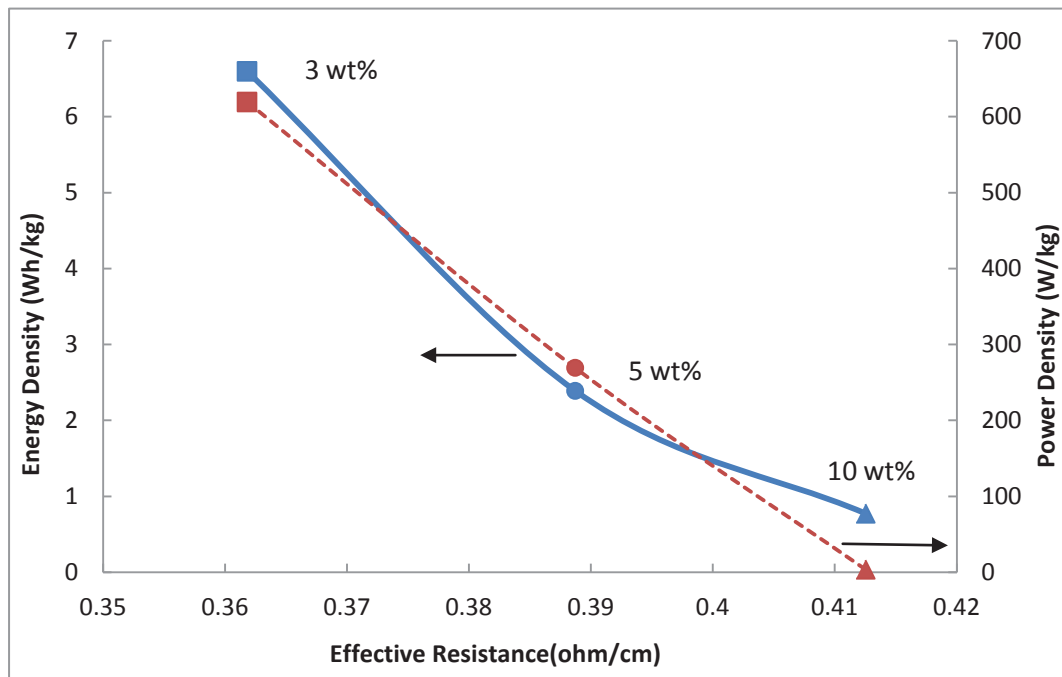


Fig. 4.12. The energy and power density as the function of ER for the 3 wt%, 5 wt% and 10 wt% symmetric cells.

## 4.3 Electrochemical Characterization of Asymmetric Capacitors

### 4.3.1 Constant Current Experiment

An asymmetric capacitor (J2) with two layers of 3 wt% PTFE/CB as the negative electrode and a nickel positive electrode supported on carbon foam (see sections 3.2.1& 3.2.2) has been constructed.<sup>42</sup> The mass of the positive and negative electrode was 0.1469 g and 0.1349 g, respectively. The area for the electrodes is 2.656 cm<sup>2</sup>. The constant current cycling at three current densities, 31.16 mA/cm<sup>2</sup>, 20.46 mA/cm<sup>2</sup> and 7.79 mA/cm<sup>2</sup>, was applied sequentially to test the electrochemical performance of J2 (1000 cycles for each current density). After the second current density measurement, a 25-days self-discharge test was conducted. The voltage is from 1.4 V to 0 V. Fig. 4.13 displays the discharge capacity as a function of cycle life. Fig. 4.14 shows the Ragone plot for J2. Table 4.6 compares the cell capacitance, power and energy density at three current densities. Fig. 4.15 compares the potential vs. time response of the representative four or five cycles during cycling at three current densities, respectively.

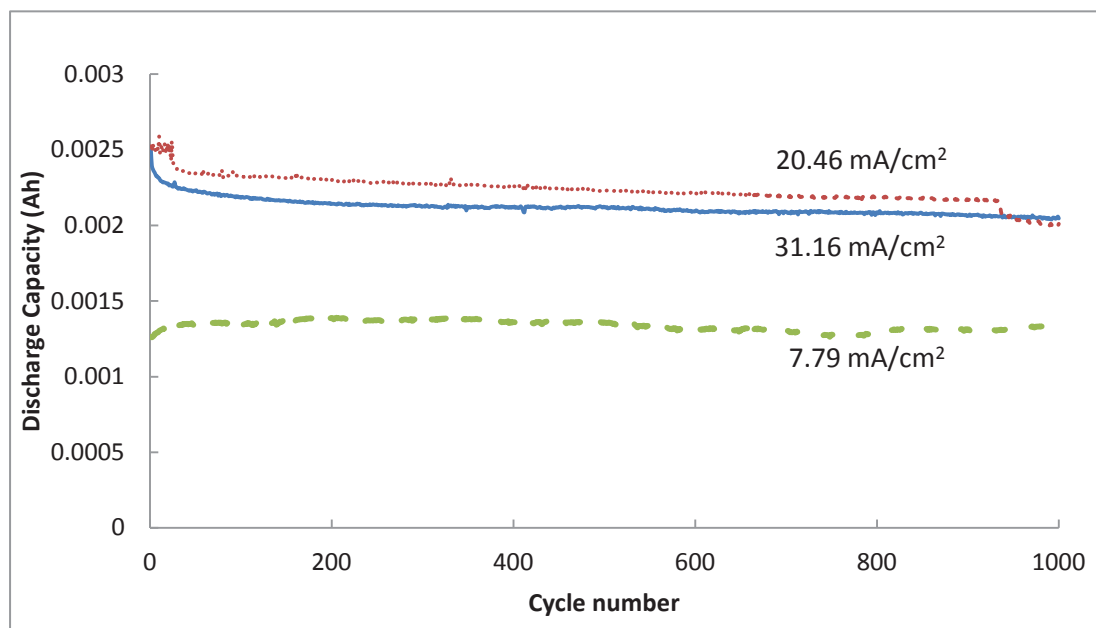


Fig. 4.13. Discharge capacity as a function of cycle life at three current densities.

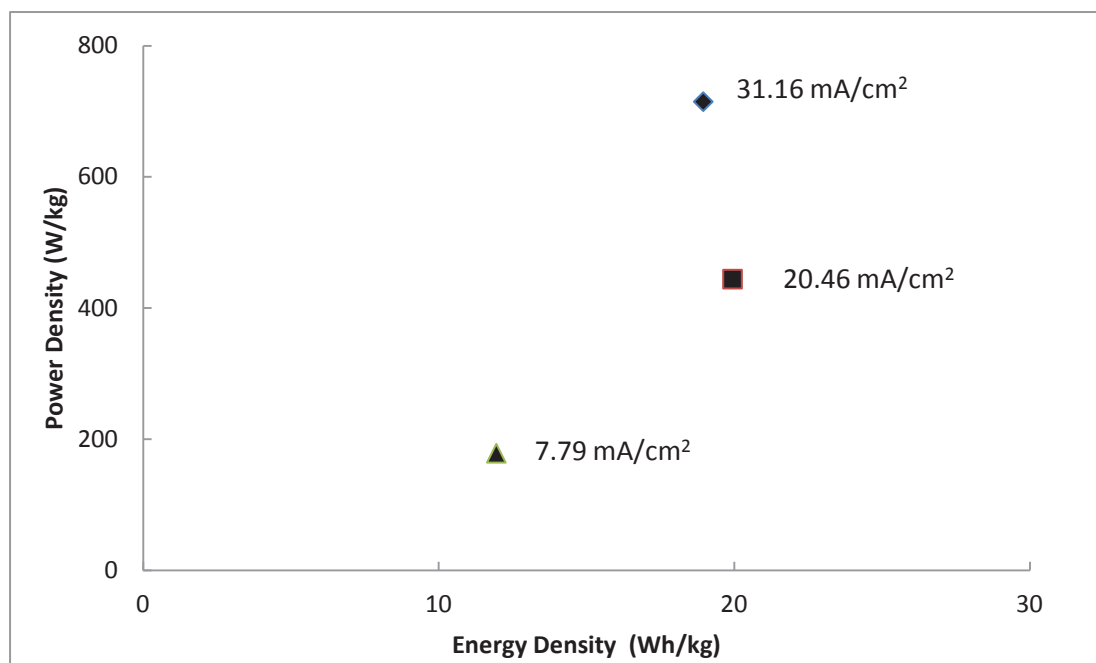
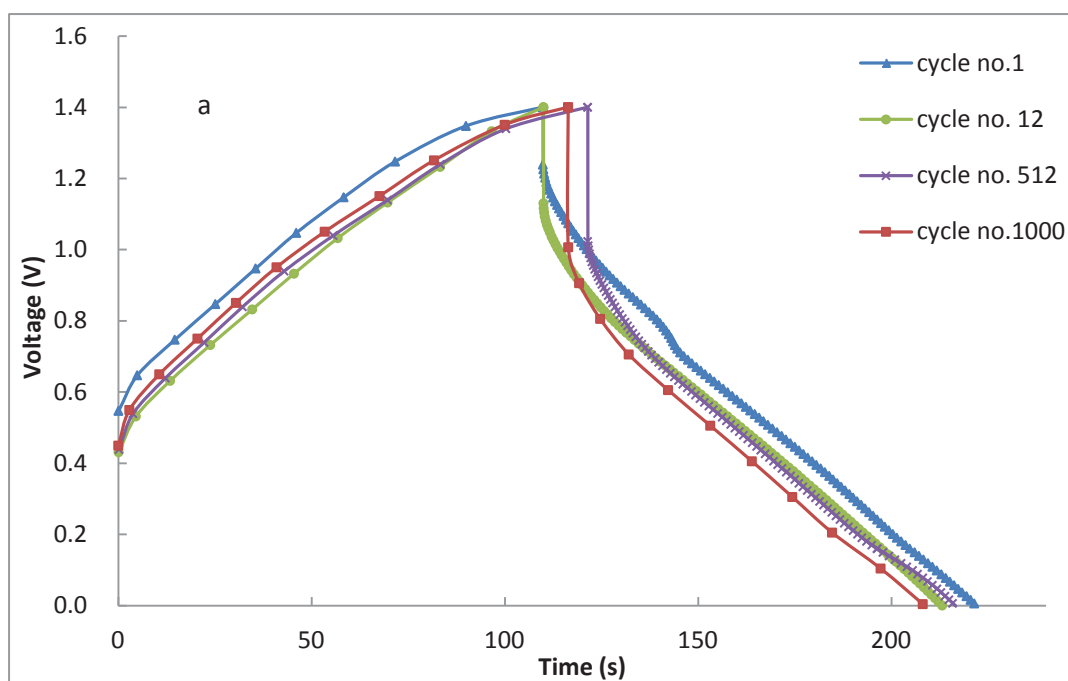


Fig. 4.14. Ragone plot for the J2 asymmetric capacitor at three current densities.

Table 4.6.

Comparison of the average specific capacitance, energy and power density of asymmetric capacitor (J2) as a function of the current density (data shown are average of 1000 cycles).

Current Density (mA/cm <sup>2</sup> )	Cycle Number	Discharge Cap. (F)	cell Specific Cap. (F/g)	Coulomb Efficiency (%)	Energy Density (Wh/kg)	Power Density (W/kg)
31.16	1-1000	5.449	19.34	81.78	18.95	714.8
20.46	1001-2000	5.734	20.35	89.56	19.94	444.1
7.79	2001-3000	3.437	12.20	79.01	11.95	178.5



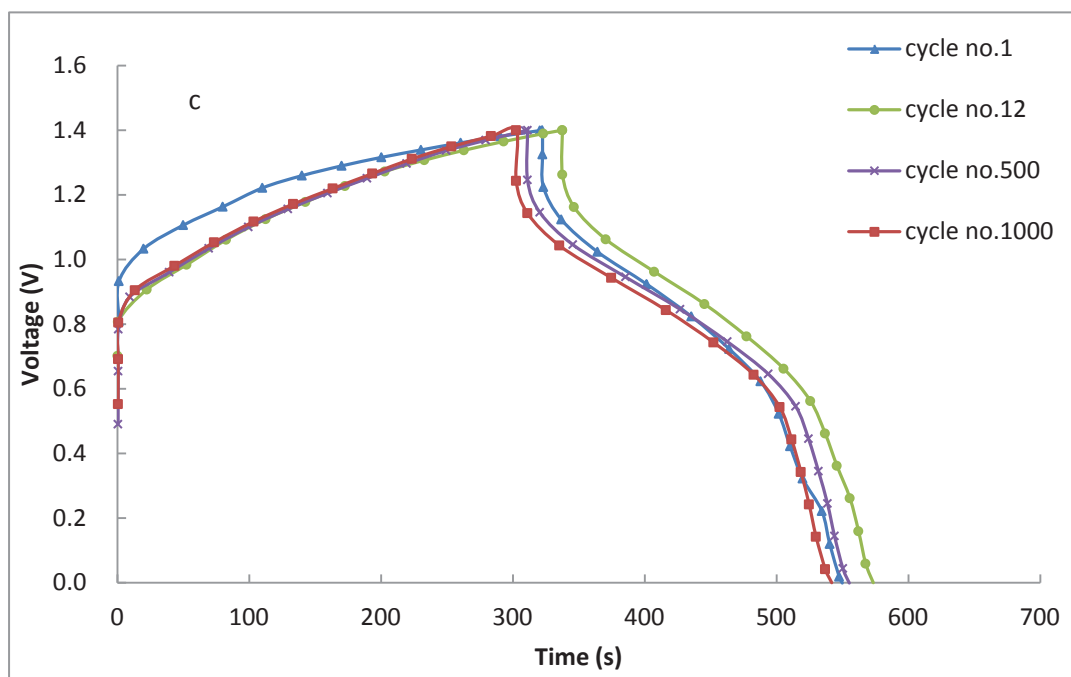
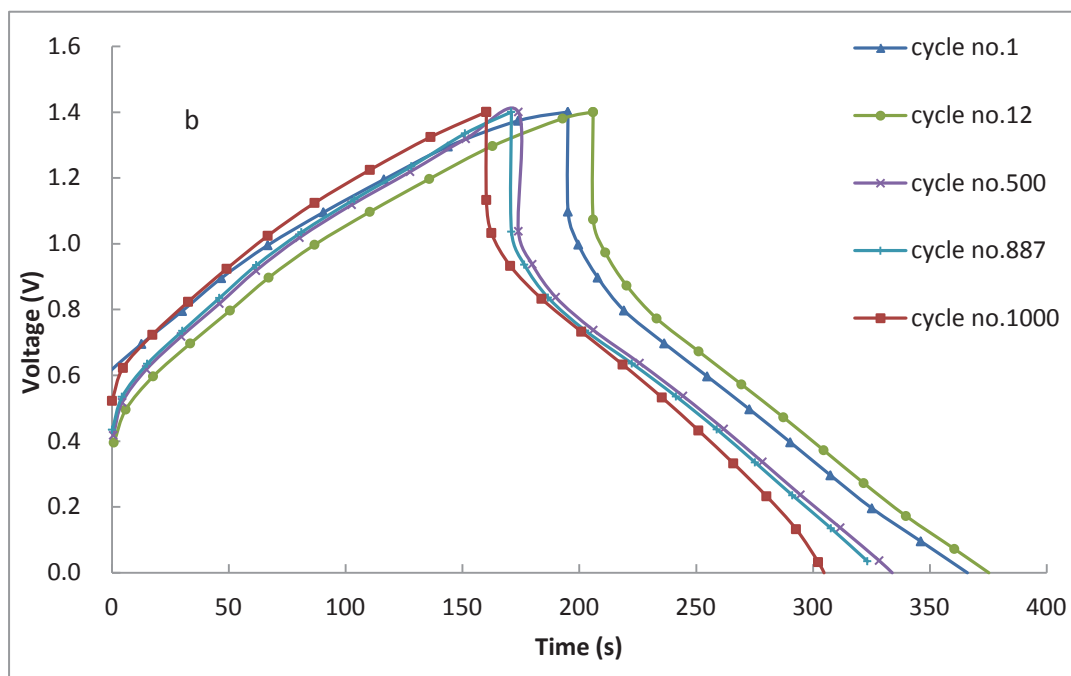


Fig. 4.15. Comparison of the potential vs. time response between the first, middle and last cycles for the asymmetric capacitor (J2) at three different current densities (a is at 31.16 mA/cm<sup>2</sup>, b is at 20.46 mA/cm<sup>2</sup>, c is at 7.79 mA/cm<sup>2</sup> ).



### 4.3.2 Cycle Life Test

In order to investigate the cycle life of the asymmetric cell with the 3 wt% PTFE/CB negative electrode and nickel hydroxide positive electrode, the asymmetric J1, J2, and J3 were cycled at constant current of 31.16, 7.79, and 5.85 mA/cm<sup>2</sup>, respectively. The cycle life is counted until the discharge capacity reduced to 80% of the initial capacity defined at 150<sup>th</sup> cycle for these three cells. Fig. 4.16 shows the discharge capacity with the cycle number. Table 4.7 compares the cycle life, the cell capacitance, power, and energy density as well as the efficiency for the asymmetric J1, J2, and J3. Fig. 4.17 compares the cell specific capacitance of the three asymmetric cells. Fig. 4.18 shows the Ragone plot for three cells.

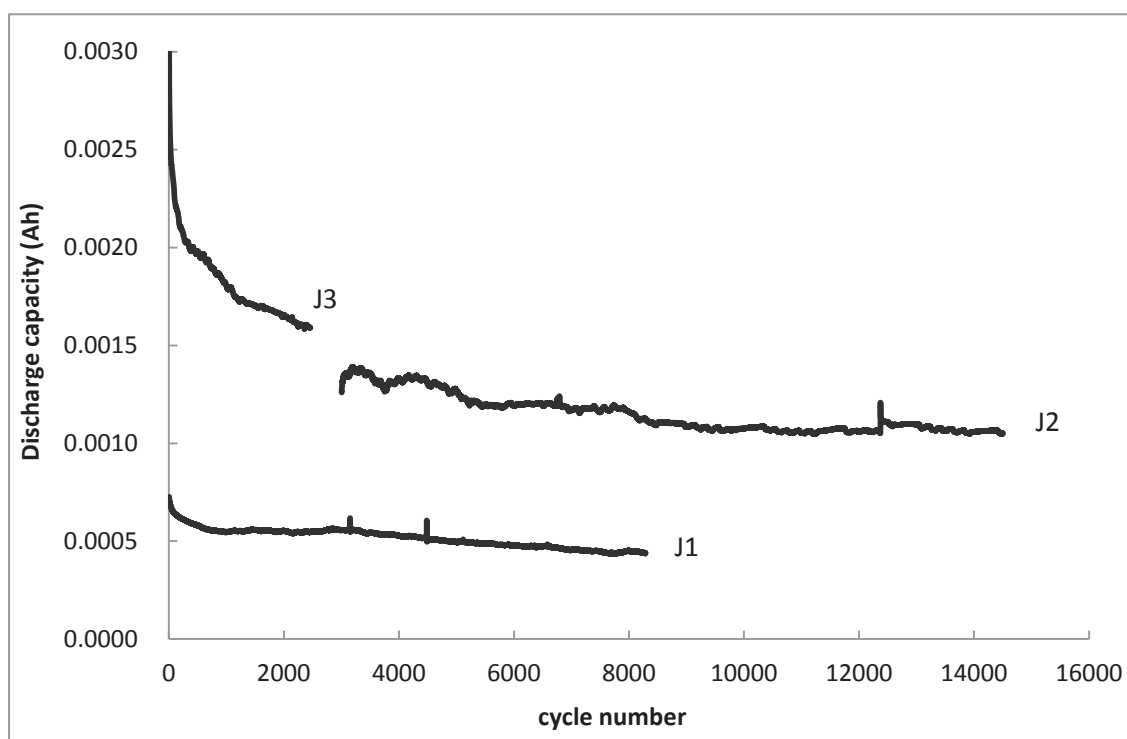


Fig. 4.16. Discharge capacity as a function of cycle life for asymmetric J1, J2, and J3 at 31.16, 7.79, and 5.85 mA/cm<sup>2</sup>, respectively.

Table 4.7.

Comparison of cycle life, cell specific capacitance, energy and power density of asymmetric capacitor J1, J2, and J3 (data shown are average over the cycle life).

Cells	Current Density (mA/cm <sup>2</sup> )	Cycle life	Discharge Cap. (F)	Cell Specific Cap (F/g)	Coulomb Efficiency (%)	Energy Density (Wh/kg)	Power Density (W/kg)
J1	31.16	8,292	2.323	8.079	82.75	3.999	618.9
J2	7.79	11,505	6.731	16.65	79.27	14.35	250.1
J3	5.58	2,457	6.540	25.48	97.10	24.84	286.2

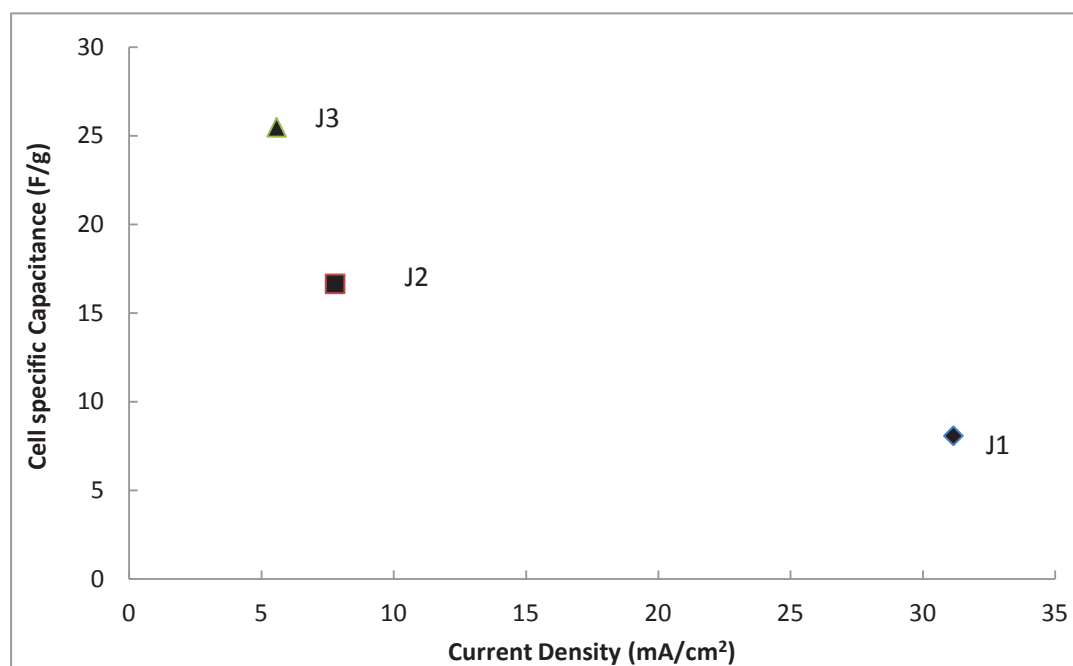


Fig. 4.17. Comparison of the cell specific capacitance of the J1, J2 and J3 asymmetric capacitors.

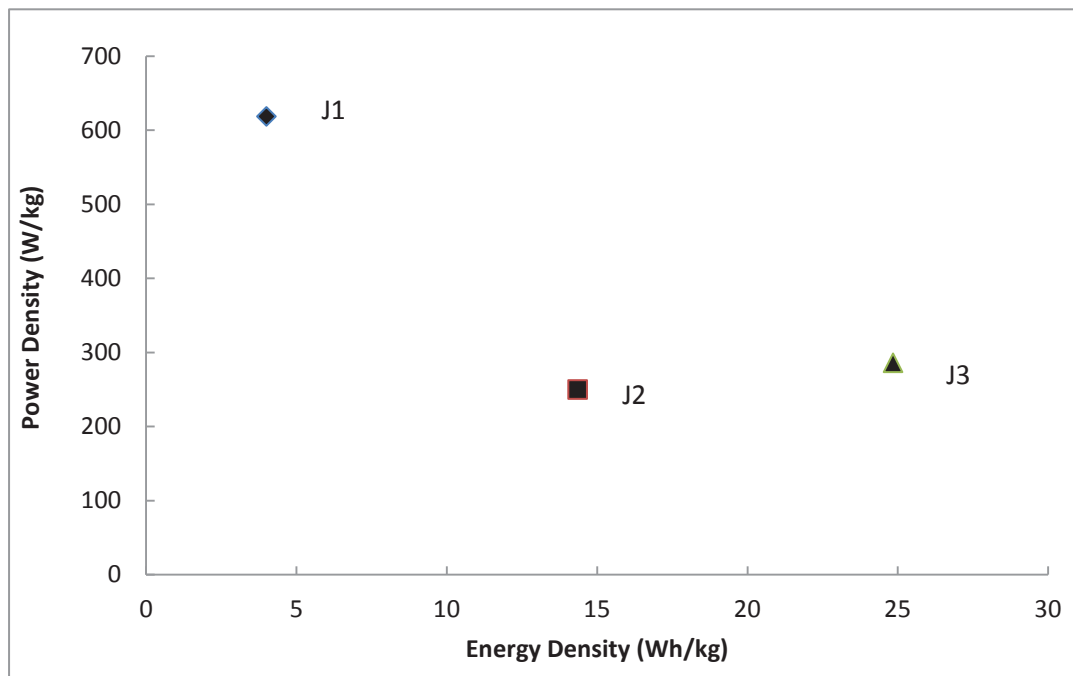


Fig. 4.18. Ragone plot for the J1, J2 and J3 asymmetric capacitor.

## 4.4 XRD Characterization of Nickel Hydroxide Electrodes

### 4.4.1 The Electrochemical Performance of Nickel Hydroxide Electrodes

The formation process of the formed electrode was shown in Fig. 4.19. The 10 mA/cm<sup>2</sup> current density was used to charge and discharge the four electrodes with a Hg/HgO reference electrode. Fig. 4.20 and Fig. 4.21 show the potential vs. time response of the charged 1x and discharged 1x electrodes, respectively. Fig. 4.22 shows the potential vs. time response of a typical cycle and the entire cycle of the charged 10x. Fig. 4.23 shows the potential vs. time response of a typical cycle, the first overcharging cycle and the entire cycle of the discharged 10 x.

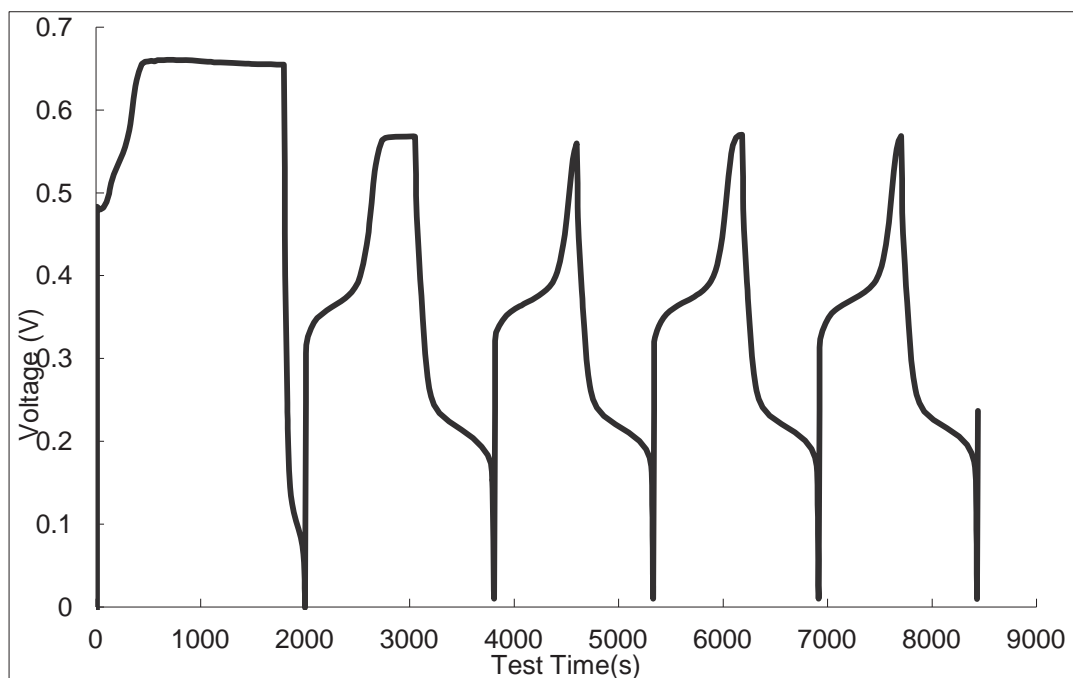


Fig. 4.19. Potential vs. time response of the formed electrode  $70 \text{ mA/cm}^2$  for first cycle,  $20 \text{ mA/cm}^2$  for 2<sup>nd</sup> to 5<sup>th</sup> cycle with a Hg/HgO reference electrode.

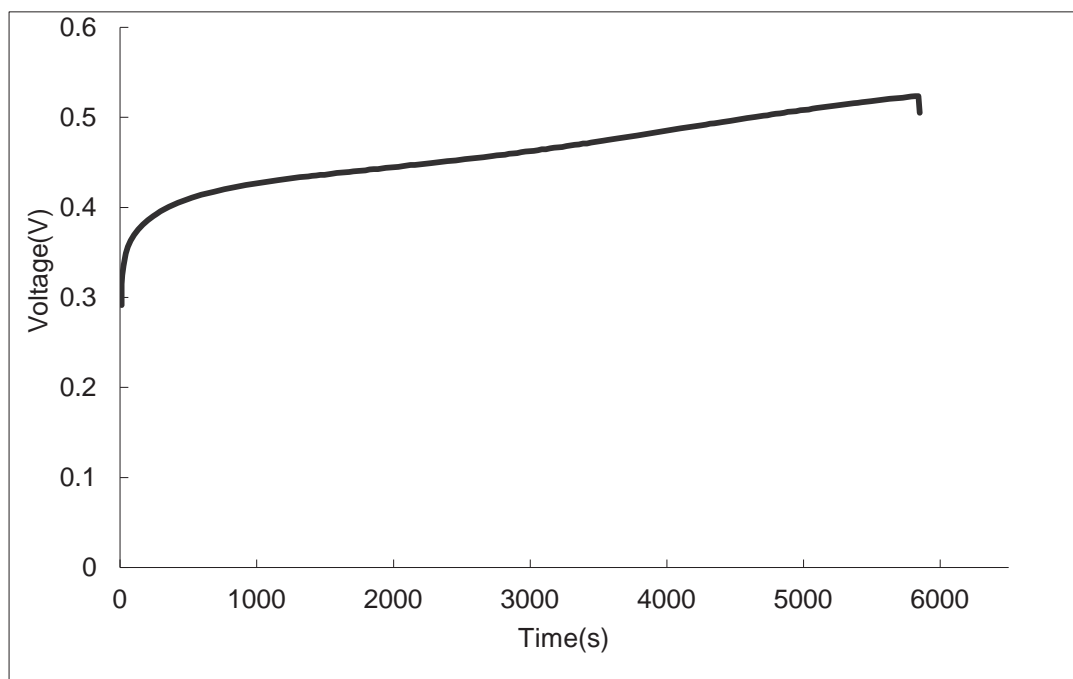


Fig. 4.20. Potential vs. time response of the charged 1x at  $10 \text{ mA/cm}^2$  with a Hg/HgO reference electrode.

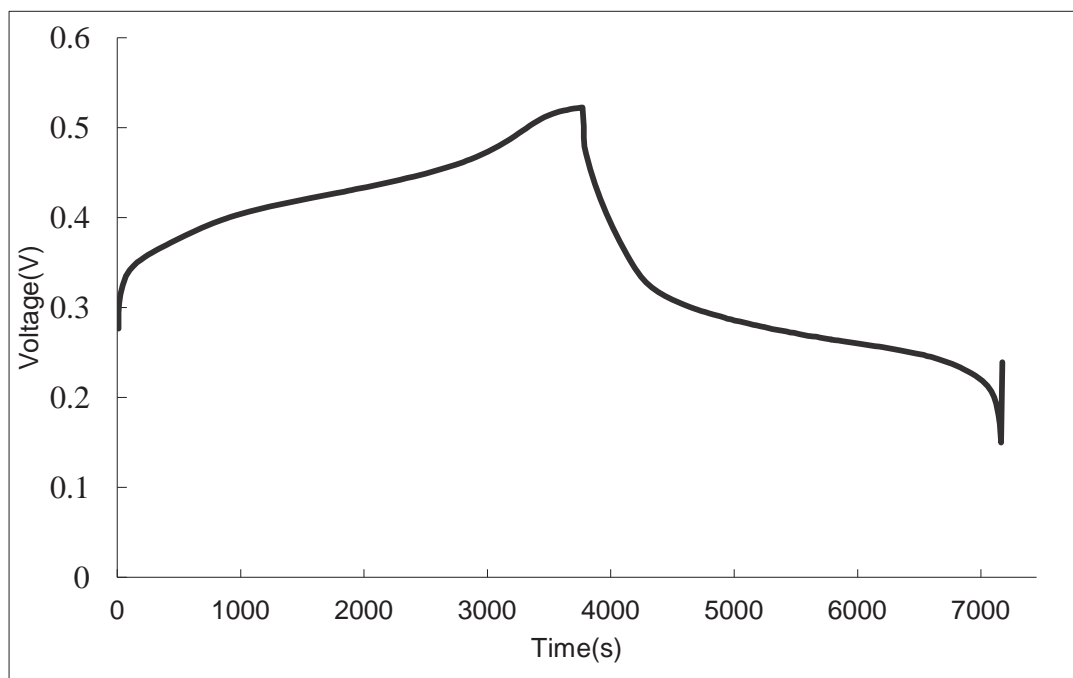
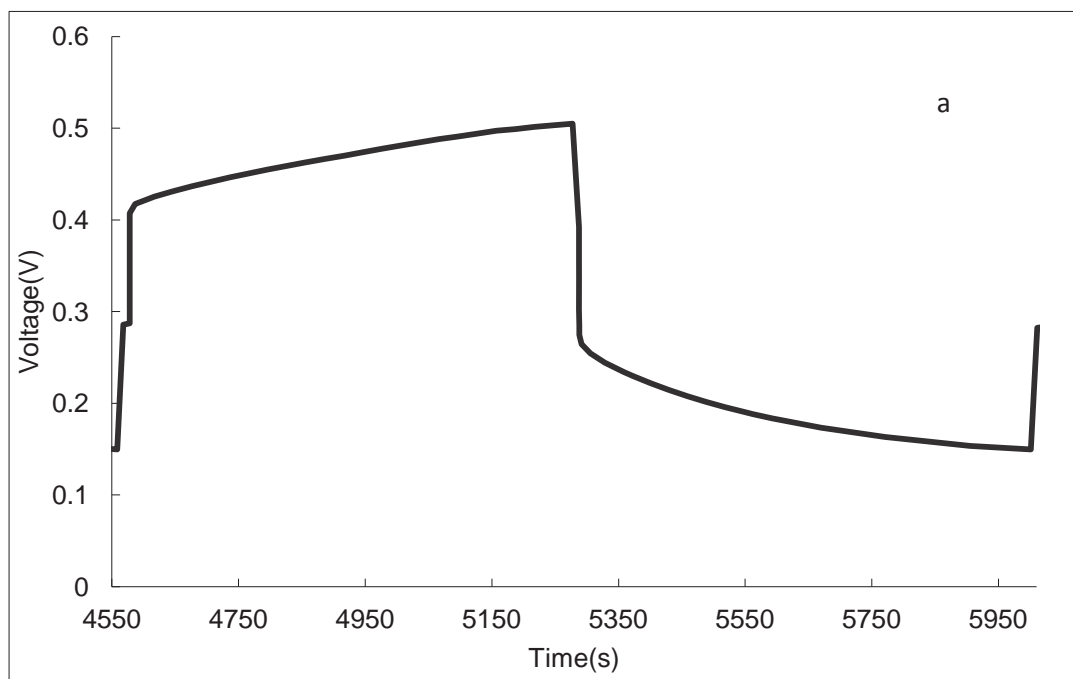


Fig. 4.21. Potential vs. time response of the discharged 1x at  $10 \text{ mA/cm}^2$  with a Hg/HgO reference electrode.



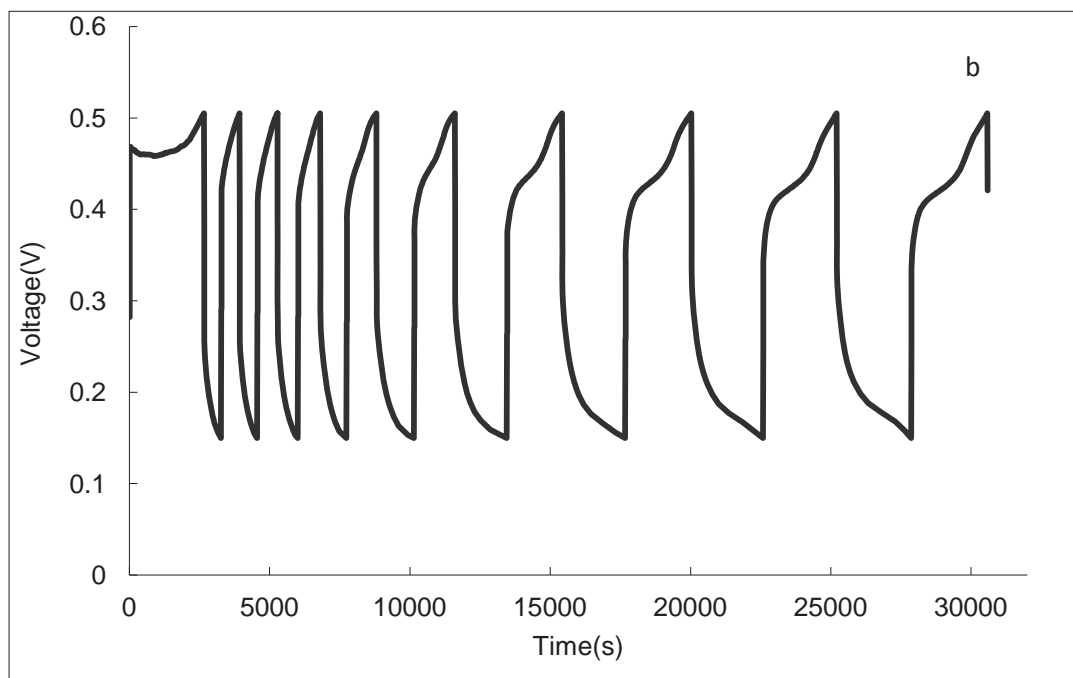
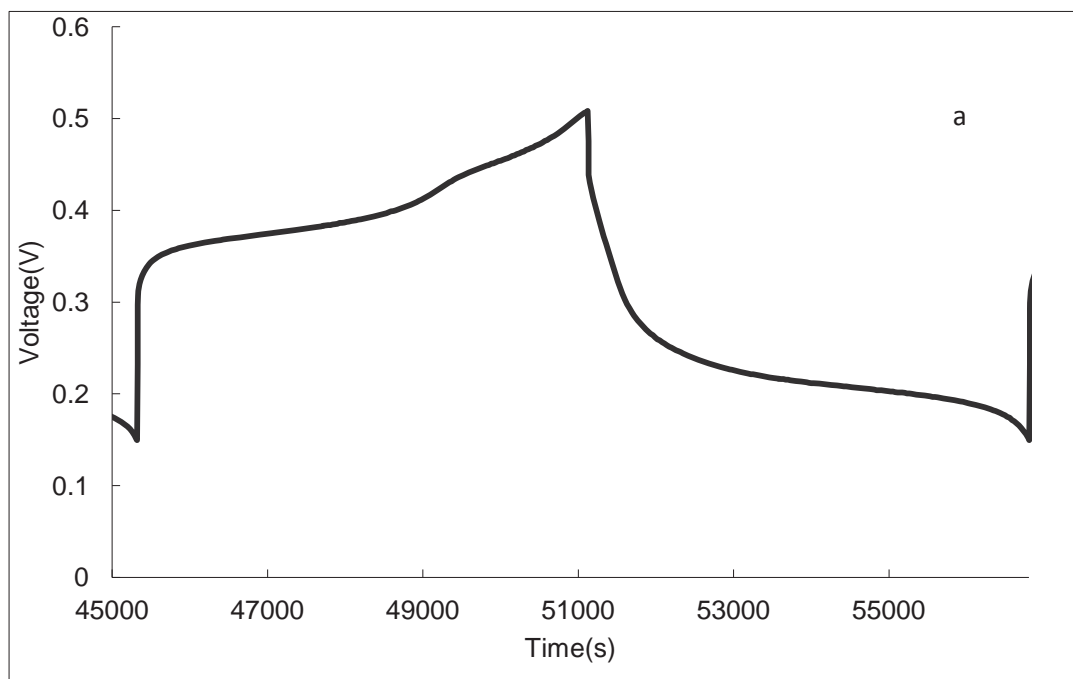


Fig. 4.22. Potential vs. time response of a typical cycle (a), the entire cycle of the charged 10x (b), at  $10 \text{ mA/cm}^2$  with a Hg/HgO reference electrode.



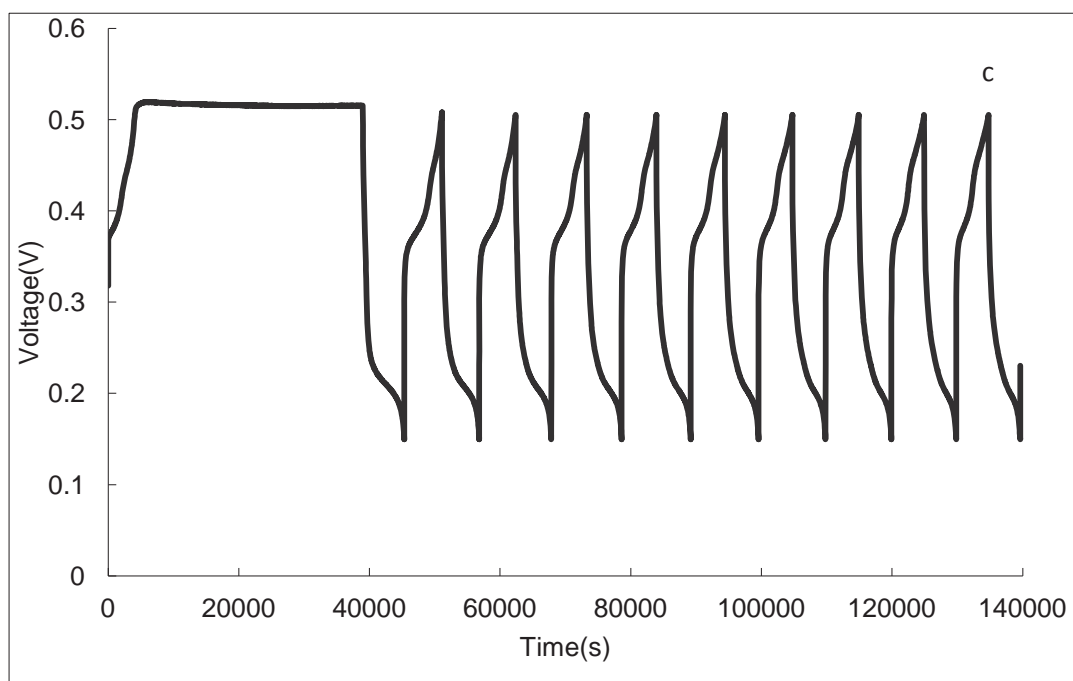
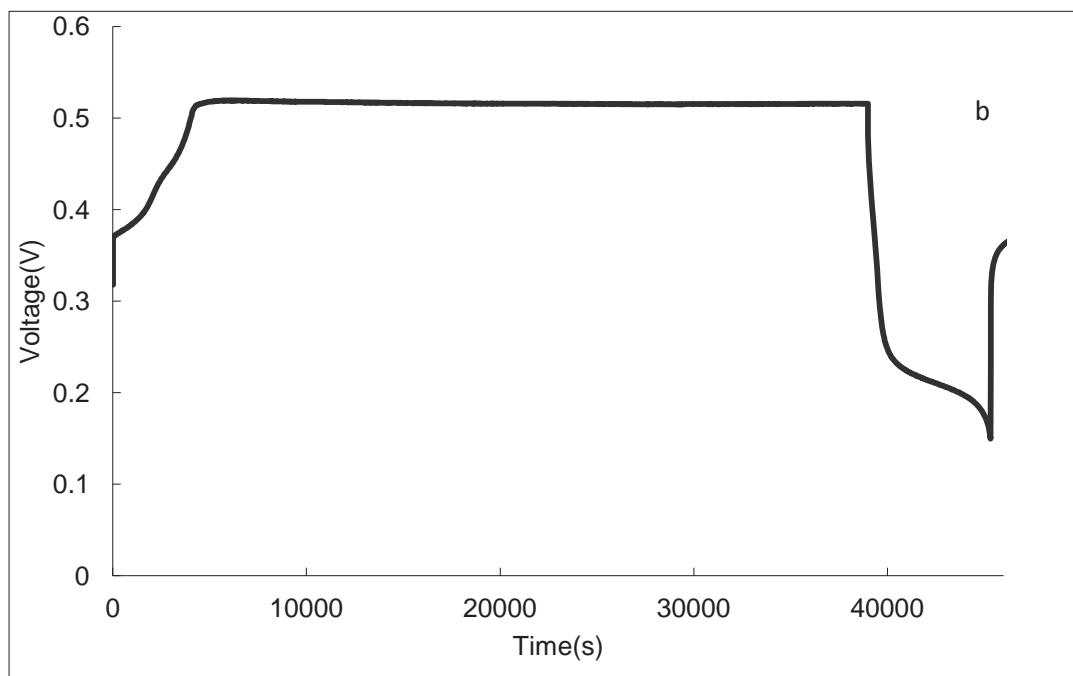


Fig. 4.23. Potential vs. time response of a typical cycle, cycle 2 (a), the first cycle showing extensive overcharging (b), the entire set of 10 cycles through the 10<sup>th</sup> discharge (c), at 10 mA/cm<sup>2</sup> with a Hg/HgO reference electrode.

#### 4.4.2 The XRD Patterns of Six Samples

XRD was employed on a Scintag XRS2000 powder diffractometer with Cu K $\alpha$  radiation ( $\lambda = 1.5406 \text{ \AA}$ ) operating at 45 kV and 35 mA to characterize a series of positive electrodes (see Table 3.1). The  $2\theta$  range for all these XRD patterns is from 5 to 85 degree. Fig. 4.24 shows the XRD patterns of all these electrodes. Fig. 4.25 compares the XRD patterns of a charged 1x electrode (c) and a charged 10x electrode (e). Fig. 4.26 compares the XRD patterns of a deposited electrode (a), a formed electrode (b), a discharged 1x electrode (d) and a discharged 10x electrode (f). The peaks of the compounds are identified in Table 4.8. The star marked sharp peaks are from carbon foam.

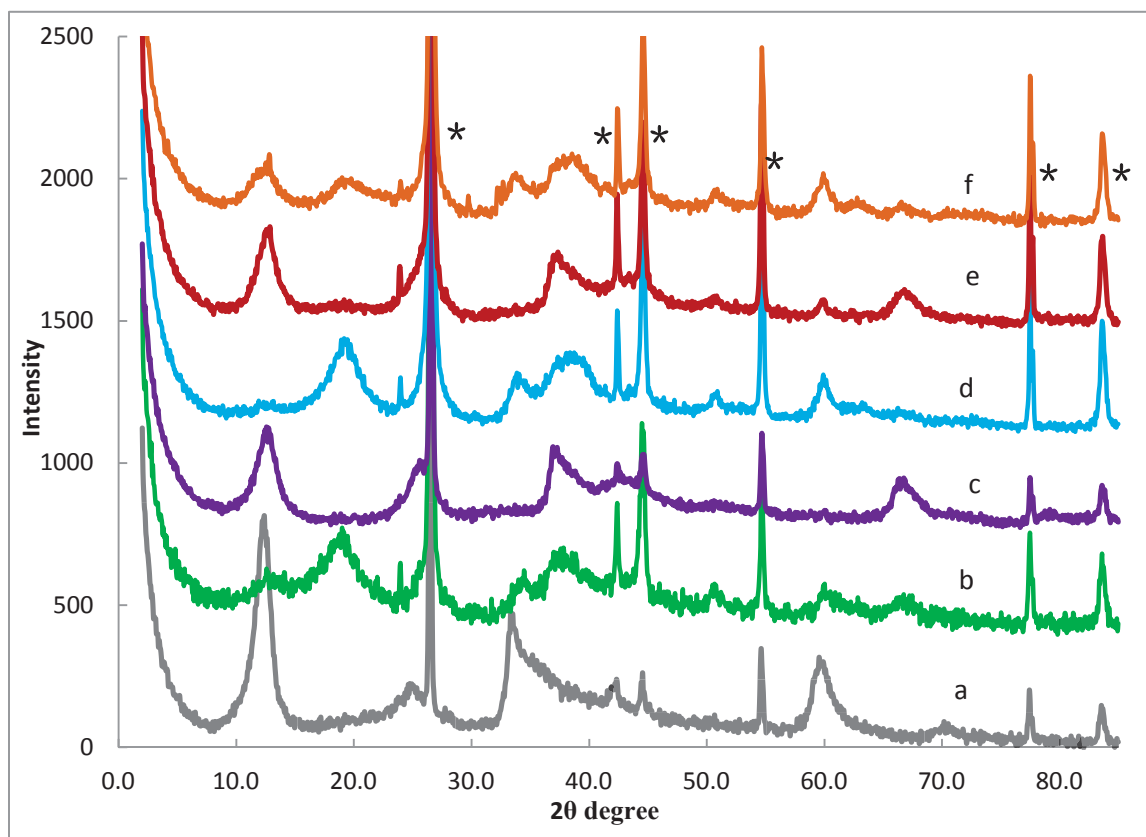


Fig. 4.24. Comparison of the XRD powder patterns of deposited (a), formed (b), charged 1x (c) and discharged 1x (d), charged 10x (e) and discharged 10x (f) electrodes (\* peaks are from carbon foam).



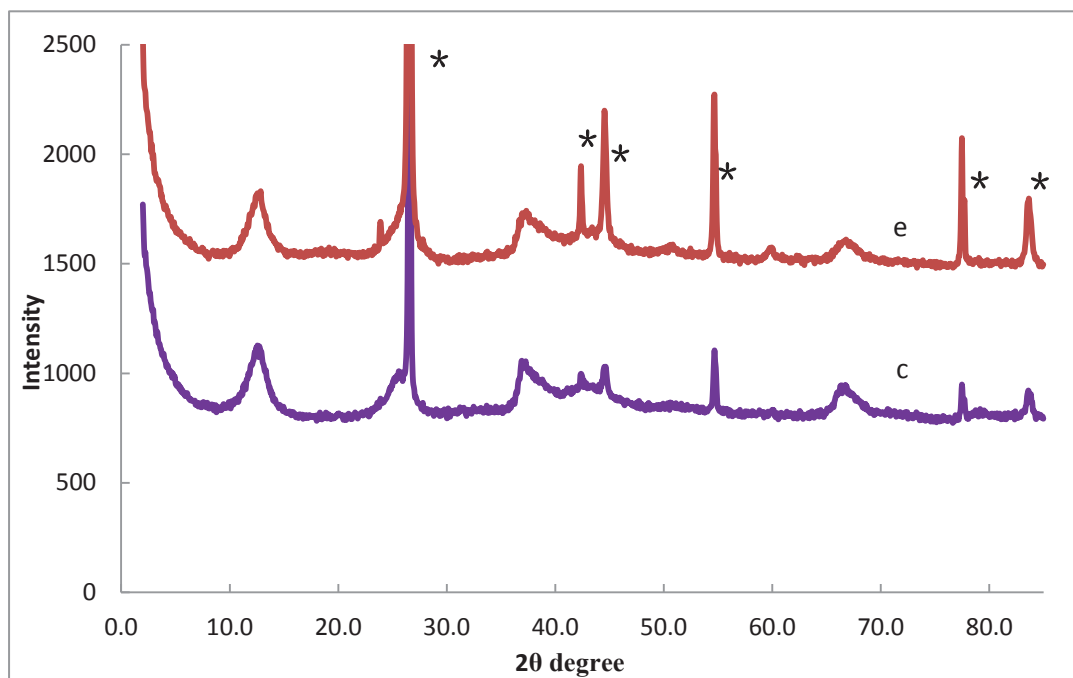


Fig. 4.25. Comparison of the XRD patterns of the charged 1x (c) and charged 10x (e) electrodes (\* peaks are from carbon foam).

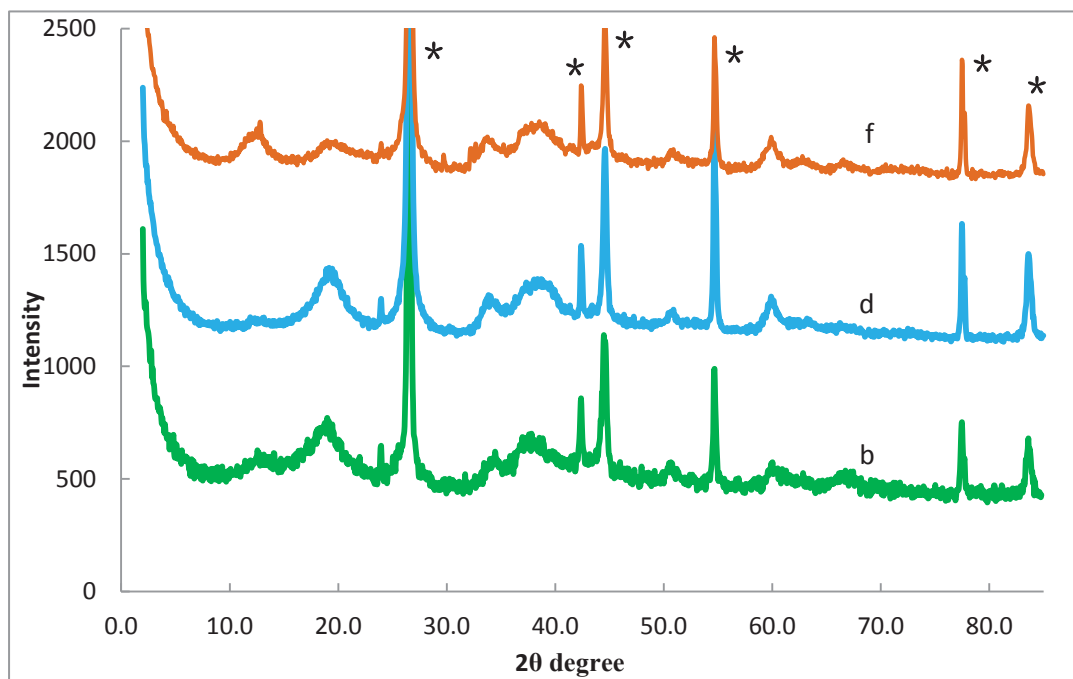


Fig. 4.26. Comparison of the XRD patterns of the formed (b), discharged 1x (d), and discharged 10x (f) electrodes (\* peaks are from carbon foam).

Table 4.8.  
Experimental XRD patterns of six samples.

<b>a</b> <b>Deposited</b>		<b>b</b> <b>Formed</b>		<b>c</b> <b>Charged</b> <b>1x</b>		<b>d</b> <b>Discharged</b> <b>1x</b>		<b>e</b> <b>Charged 10x</b>		<b>f</b> <b>Discharged</b> <b>10x</b>	
<b><u>2<math>\theta</math></u></b>	<b><u>d (Å)</u></b>	<b><u>2<math>\theta</math></u></b>	<b><u>d (Å)</u></b>	<b><u>2<math>\theta</math></u></b>	<b><u>d (Å)</u></b>	<b><u>2<math>\theta</math></u></b>	<b><u>d (Å)</u></b>	<b><u>2<math>\theta</math></u></b>	<b><u>d (Å)</u></b>	<b><u>2<math>\theta</math></u></b>	<b><u>d (Å)</u></b>
12.32	7.178	12.68	6.975	12.68	6.975	12.68*	6.975	12.68	6.975	12.68	6.975
24.92	3.570	19.02	4.662	25.52	3.488	19.02	4.662	25.52	3.488	19.02	4.662
33.60	2.665	34.28	2.614	36.82	2.439	33.78	2.654	36.82	2.439	33.78	2.654
33.72	2.656	37.45	2.399	37.40	2.403	38.47	2.338	37.40	2.403	38.47	2.338
37.38	2.404	50.62	1.802	42.86	2.108	50.72	1.798	42.86	2.108	50.72	1.798
59.54	1.551	59.92	1.542	50.83	1.795	59.92	1.542	50.83	1.795	59.92	1.542
60.02	1.540	66.68	1.402	66.68	1.402	62.96	1.475	60.02	1.540	62.96	1.475
						66.68	1.402	66.68	1.402	66.68	1.402

$\lambda = 1.540562\text{Å}$ ; \* very weak peak.

## CHAPTER 5

### DISCUSSION

#### 5.1 Evaluation of Symmetric Capacitors

Cyclic voltammetry is a standard method for evaluating the quality of a double layer capacitor. An ideal symmetric capacitor has a rectangular shaped CV curve and does not contain any redox peaks. CVs of 3 wt% and 5 wt% PTFE/CB symmetric cells are compared. A constant current charge/discharge measurement is then used to examine the stability of the symmetric cells, and to investigate their specific capacitance, energy density and power density. Results of the 3 wt% and 5 wt% PTFE/CB cells are compared with the 10 wt% symmetric cell data to identify which PTFE/CB electrode has the highest specific capacitance, energy density and power density.

##### 5.1.1 Evaluation of the 3 wt% Symmetric Capacitor

The perfectly rectangular CV curves of the 3 wt% symmetric cell are shown in Fig. 4.1, which demonstrate there was no redox reaction occurring. The current reached 0.36 A at the 100 mV/s scan rate. This means the 3 wt% PTFE/CB electrode is capable of ionic transport, which should respond very well during the charge and discharge. Note that the current rapidly increased as the increased scan rate. The cell specific capacitance was calculated at each scan rate and is shown in Table 4.1. The highest specific capacitance of the 3 wt% PTFE/CB carbon black sheet was 146.14 F/g, which was obtained from the slowest CV at the 1 mV/s scan rate. Table 4.1 shows that the specific capacitance decreases with increasing scan rate. This can be explained because the ions may not have enough time to penetrate into the pores and access all surface area, which limited the capacitance.

The constant current charge and discharge ( $30 \text{ mA/cm}^2$ ) behavior of the 3 wt% symmetric cell is depicted in Fig. 4.3, and these curves show a typical symmetric charge/discharge behavior. Fig. 4.4 compares charge/discharge curves at the 1<sup>st</sup> and 300<sup>th</sup> cycles, and shows the internal resistance increased very slightly after 300 cycles. Fig. 4.5 depicts the discharge capacity and the efficiency of the cell over 300 cycles. The cell has the average discharge capacitance of 3.07 F with an average efficiency of 89.5% over the 300 cycles, ranging from 89.9% to 88.8%. This demonstrates that the 3 wt% symmetric cell has a very steady performance during the charge/discharge. The average single electrode specific capacitance of 300 cycles was 121.8 F/g, which was 16.22 F/g higher than the best result reported by Wee Nee Yeo – 105.58 F/g single electrode specific capacitance of 95 wt% RP-20 at  $5 \text{ mA/cm}^2$ .<sup>41</sup> At the same current density as the 3 wt% symmetric cell, 95 wt% RP-20 has 62.5 F/g single electrode specific capacitance as estimated. The higher weight percentage of the binder in the RP-20 cell was the main reason for the specific capacitance decrease. Because the more binder added, the more resistance was brought in (see Fig. 4.11). Above all, the 3 wt% symmetric cell is a typical double layer capacitor and has a quite stable performance and high specific capacitance over the cycle life.

#### 5.1.2 Evaluation of the 5 wt% Symmetric Capacitor

The CV curves of the 5 wt% symmetric cell were not a perfect rectangular shape, but they did not have any redox peaks. This means that the current increased rapidly with the increasing voltage. Table 4.2 shows the calculated specific capacitance at different scan rates, and that the highest one was 99.6 F/g at the 1 mV/s scan rate. The 5 wt% symmetric cell lost capacitance for the same reason as the 3 wt% cell, which was limited time to access all surface area. The charge/discharge behavior depicted in Fig. 4.6 was not a

perfectly symmetric curve due to more internal resistance in the cell as compared with the 3 wt% cell. The charge/discharge behavior of the 1<sup>st</sup> and 300<sup>th</sup> cycles is plotted in Fig. 4.7, which shows that the 300<sup>th</sup> cycle has more resistance and less discharge time compared to the 1<sup>st</sup> cycle. Fig. 4.8 shows the discharge capacity and the efficiency as a function of the cycle life. The average discharge capacitance was 1.60 F and the efficiency was above 83.1% over the 300 cycles ranging from 82.0% to 83.5%. The average single electrode specific capacitance of 300 cycles was 66.7 F/g (see Table 4.2), which was slightly lower than 70.08 F/g of 95 wt% RP-20 at 20 mA/cm<sup>2</sup> by Wee Nee Yeo.<sup>41</sup> This may be caused by the different assembly technique. The 5 wt% cell might not be tightened very well, which could cause some energy loss between the current collectors and electrodes. In short, the 5 wt% cell has a stable electrochemical performance but relatively more resistance when compared with the 3 wt% cell.

### 5.1.3 Comparison of the 3 wt%, 5 wt%, and 10 wt% Symmetric Capacitors

The comparison of the CV performance of the 3 wt% and 5 wt% symmetric cells at the 100 mV/s scan rate is shown in Fig.4.9. As shown in this figure, the 3 wt% cell reached 0.36 A, which was much higher than 0.12 A for the 5 wt% cell. This indicates that the 3 wt% symmetric cell had a smaller effective resistance (ER) than the 5 wt% cell. The comparison of energy density vs. power density of the 3 wt%, 5 wt%, and 10 wt% (from P. Sasthan Kuttipillai) symmetric cells is shown in Fig.4.10 and Table 4.3. The 3 wt% cell had the highest energy density (6.44 Wh/kg) and power density (619 W/kg), followed by the 5 wt% (2.39 Wh/kg and 269.2 W/kg), with the 10 wt% having the lowest results (0.774 Wh/kg and 3.68 W/kg). This can be explained by the following:

- 1) The 3 wt% PTFE/CB sheet had the lowest ER, 0.3618 ohm/cm (see Table 4.5), and the 10 wt% sheet had the highest ER, 0.4125 ohm/cm (12% more than the ER of the 3

wt% one). Fig. 4.11, (PTFE wt% vs. ER), clearly shows that the ER of the carbon sheet is increasing as the PTFE weight percentage was increased. Fig. 4.12, (energy density vs. ER and power density vs. ER), indicates that the energy density and power density are decreasing as ER was increased in the 3 wt%, 5 wt%, and 10 wt% cells. Due to the poor conductivity of PTFE, as more binder is added, the resistance of the electrode increased. The poor conductivity of the 10 wt% sheet requires more energy to charge and discharge the cell, which can contribute to a low energy density.

2) The lower BET surface area can also contribute to the lower energy density. As Table 4.4 shows, the 3 wt% sheet had the highest area, 1239 m<sup>2</sup>/g, followed by the 5 wt%, 1237 m<sup>2</sup>/g, while the 10 wt% only had 967 m<sup>2</sup>/g (22% less than the 3 wt%). This reduced BET surface area was mainly due to the addition of PTFE. Larger particles of PTFE can block off the pores within carbon black, which reduces the area available within the carbon black to absorb the ions in electrolyte. Consequently, it would reduce the available area of the double layer on the carbon surface, which is a very important parameter for the capacitance of the cell (see equation 2.1). According to equation 3.3 and 3.4, the energy density and power density are calculated from the discharge capacitance. Both the energy and power densities will decrease as the capacitance is reduced.

## 5.2 Evaluation of the Asymmetric Capacitor J2

The asymmetric capacitors, J1, J2, and J3 were successfully fabricated with a 3 wt% PTFE/CB negative electrode and nickel hydroxide positive electrode. The constant current charge/discharge at 31.16 mA/cm<sup>2</sup>, 20.46 mA/cm<sup>2</sup>, and 7.79 mA/cm<sup>2</sup> were sequentially applied to examine the electrochemical performance as well as to investigate the energy and power density of the asymmetric capacitor J2 (1000 cycles for each current density).

After the second current density measurement, a self-discharge test was conducted. This perturbed the results for the cell specific capacitance and energy density at the third, 7.79 mA/cm<sup>2</sup> current density. Besides, the cycle life of the asymmetric cells, J1, J2, and J3, were studied at 31.16 mA/cm<sup>2</sup>, 7.79 mA/cm<sup>2</sup>, and 5.58 mA/cm<sup>2</sup>, respectively.

#### 5.2.1 Evaluation of the Asymmetric Capacitor J2 at 31.16 mA/cm<sup>2</sup> Current Density

The discharge capacity vs. cycle number is shown in Fig.4.13 (the solid line). The discharge capacity dropped very quickly in the first 200 cycles, then became stable until the 700<sup>th</sup> cycle, and was followed by a slow drop to the 1000<sup>th</sup> cycle. The Table 4.6 calculates the average cell capacitance, efficiency, energy density and power density over 1000 cycles at this current density. The cell has the average cell specific capacitance 19.34 F/g ranging from 22.75 F/g to 18.72 F/g with the average efficiency 81.78% ranging from 102.2% to 80.12%, which indicates that electrochemical performance of the cell is not stable at 31.16 mA/cm<sup>2</sup>. Fig. 4.14, (Ragone plot), shows that the J2 has the highest power density (714.8 W/kg) and relatively higher energy density (18.95 Wh/kg) at 31.16 mA/cm<sup>2</sup> among the three current densities.

In order to further understand the performance degradation, the first, the 12<sup>th</sup>, the 512<sup>th</sup>, and the 1000<sup>th</sup> charge/discharge profiles of the cell at 31.16 mA/cm<sup>2</sup> are compared in Fig. 4.15 (a). Table 5.1 shows the constant current charge/discharge times, voltage drop caused by internal resistance (IR), cell specific capacitances, efficiencies, energy, and power densities for these cycles.

Table 5.1.

Comparison of the constant current charge/discharge times,  $\Delta V_{IR}$ , cell capacitances, efficiencies, energy, and power densities for the cycles at 31.16 mA/cm<sup>2</sup>.

<b>Cycle number</b>	<b>Charge Time (s)</b>	<b>Discharge Time (s)</b>	<b><math>\Delta V_{IR}</math> (V)</b>	<b>Columbic Efficiency (%)</b>	<b>Energy Density (Wh/kg)</b>	<b>Power Density (W/kg)</b>
1	109.8	112.3	0.1612	102.2	22.29	714.8
12	103.2	109.9	0.2698	93.55	20.50	671.3
512	121.2	95.10	0.3768	78.22	18.89	714.9
1000	115.3	92.35	0.3933	80.12	18.34	715.0

From Fig. 4.15 (a) and Table 5.1, the  $\Delta V_{IR}$  was increased rapidly and the  $\Delta V_{IR}$  at the 1000<sup>th</sup> cycle is 2.5 times that of the first cycle, which indicates considerable internal resistance was gained over the 1000 cycles at this current density. When comparing the 1000<sup>th</sup> cycle with the first cycle, the discharge time decreased 14.76% while the charge time increased 5.50%. The cell specific capacitance was dropped 17.72%, hence the energy density was decreased 17.72%, which is caused by the significantly increased internal resistance.

The average energy density of the asymmetric cell J2 at 31.16 mA/cm<sup>2</sup> was almost 3 times that of the 3 wt% symmetric cell (6.44 Wh/kg) and was 5.11 Wh/kg lower than the best asymmetric cells result (SW 104 at 5.0 mA/cm<sup>2</sup>) of Wen Nee Yeo.<sup>41</sup> As estimated, energy density of SW 104 was 16.6 Wh/kg at 31.16 mA/cm<sup>2</sup>. The huge increase as compared to the symmetric cell is due to the faradaic electrode in the cell which was the nickel oxyhydroxide electrode in this case. The minor decrease as compared to Wen Nee Yeo is because of the relatively high current density (31.16 mA/cm<sup>2</sup>) as compared with 5.0



mA/cm<sup>2</sup> of SW 104 (see equation 3.3). At the same time, the power density of the asymmetric cell was 110.7 W/kg higher than the 3 wt% symmetric cell (604.1 W/kg) and 106.1 W/kg higher than that of the best result (SW 104 at 50.0 mA/cm<sup>2</sup>) of Wen Nee Yeo.<sup>41</sup> The power density was 342.8 W/kg of SW 104 at 31.16 mA/cm<sup>2</sup>. The increased voltage range ( $\Delta V = 1.4$  V for J2 and 1.0 for SW 104) is the main reason for the increases in the power density.

Above all, the asymmetric cell J2 at 31.16 mA/cm<sup>2</sup> has a relatively higher energy density and the highest average power density over 1000 cycles among three current densities. This means this current density can be selected when high power density is required for Ni(OH)<sub>2</sub>/CB asymmetric cells. On the other hand, the cell was not stable due to rapidly increasing internal resistance.

#### 5.2.2 Evaluation of the Asymmetric Capacitor J2 at 20.46 mA/cm<sup>2</sup> Current Density

The discharge capacity vs. cycle number is shown in Fig.4.13 (the dotted line). The discharge capacity has one sudden drop after the first 50 cycles followed by a slow drop and then gradually decreased until the 900<sup>th</sup> cycle, where another sudden drop occurred. From the 900<sup>th</sup> to 1000<sup>th</sup> cycles, the discharge capacity at 20.46 mA/cm<sup>2</sup> was less than at 31.16 mA/cm<sup>2</sup>. The average cell specific capacitance, efficiency, energy density and power density are calculated in Table 4.6. The cell has the average cell specific capacitance of 20.35 F/g, ranging from 21.39 F/g to 18.35 F/g, and the average efficiency of 89.56%, ranging from 91.71% to 81.67%, which suggests that electrochemical performance at 20.46 mA/cm<sup>2</sup> is not stable over the 1000 cycle life. Fig. 4.14, (Ragone plot), shows that J2 has the highest energy density (19.94 Wh/kg) and relatively higher power density (383.5 W/kg) at 20.46 mA/cm<sup>2</sup> of the three current densities.

The 1001<sup>st</sup>, the 1012<sup>th</sup>, the 1500<sup>th</sup>, the 1887<sup>th</sup> and the 2000<sup>th</sup> charge/discharge profiles of the cell at 20.46 mA/cm<sup>2</sup> were depicted in Fig. 4.15 (b) to investigate what

happened to the cell over 1000 cycles. Table 5.2 shows the constant current charge/discharge times,  $\Delta V_{IR}$ , cell specific capacitances, efficiencies, energy, and power densities for these cycles.

Table 5.2.

Comparison of the constant current charge/discharge times,  $\Delta V_{IR}$ , cell capacitances, efficiencies, energy, and power densities for the cycles at 20.46 mA/cm<sup>2</sup>.

<b>Cycle number</b>	<b>Charge Time (s)</b>	<b>Discharge Time (s)</b>	<b><math>\Delta V_{IR}</math> (V)</b>	<b>Columbic Efficiency (%)</b>	<b>Energy Density (Wh/kg)</b>	<b>Power Density (W/kg)</b>
1001	215.0	170.9	0.2906	81.67	20.96	441.6
1012	205.0	169.3	0.3266	81.81	20.91	444.5
1500	173.3	160.0	0.3597	91.01	19.91	448.0
1887	170.8	152.4	0.3637	90.33	18.58	438.9
2000	160.2	144.5	0.2676	87.27	17.98	448.1

From the Fig. 4.15 (b) and Table 5.2, the  $\Delta V_{IR}$  increased significantly from the 1001<sup>st</sup> cycle to the 1887<sup>th</sup> cycle, which demonstrates the cell gained considerable internal resistance over the 900 cycles at this current density. The decrease  $\Delta V_{IR}$  at the 2000<sup>th</sup> cycle may be caused by the slowing in the discharge process. As compared to the 1001<sup>st</sup> cycle, the charge time of the 2000<sup>th</sup> cycle reduced 25.49% and discharge time decreased 15.45%, which indicates the charge performance of the cell has been significantly degraded after 1000 cycles. The cell specific capacitance was dropped 14.21% as well as the energy density, which is mainly caused by the significantly increased internal resistance.

The energy density at 20.46 mA/cm<sup>2</sup> was three times that of the 3 wt% symmetric

cell (6.44 Wh/kg) and was 4.51 Wh/kg lower than the best result (SW 104 at 5.0 mA/cm<sup>2</sup>) Wen Nee Yeo.<sup>41</sup> The increase as compared to the symmetric cell is due to the faradaic electrode in the cell, which has the same reason as the increase at 31.16 mA/cm<sup>2</sup>. The slight decrease as compared to Wen Nee Yeo is also because of the relatively high current density (see equation 3.3). At 20.46 mA/cm<sup>2</sup>, SW 104 as estimated had 18.8 Wh/kg energy density. The power density of the asymmetric cell was 160.6 W/kg less than the 3 wt% symmetric cell (604.1 W/kg), which is due to the greater discharge time used for the asymmetric cell. The power density was 40.0 W/kg less than the best result (SW 104 at 50.0 mA/cm<sup>2</sup>) of Wen Nee Yeo due to the relatively lower current density, 20.46 mA/cm<sup>2</sup>, as compared to 50.0 mA/cm<sup>2</sup>.<sup>41</sup> The power density of SW 104 at 20.46 mA/cm<sup>2</sup> was 246.8 W/kg as estimated.

In summary, the asymmetric cell J2 at 20.46 mA/cm<sup>2</sup> has the highest energy density (19.94 Wh/kg) and relatively higher power density (383.5 W/kg) over 1000 cycles. On the other hand, the cell is still not stable at this current density over the cycle life due to increasing internal resistance. Beside, the charge performance of the cell has been degraded over the cycles. The cell has experienced a rapid drop in the energy density.

### 5.2.2 Evaluation of the Asymmetric Capacitor J2 at 7.79 mA/cm<sup>2</sup> Current Density

The discharge capacity vs. cycle number is shown in Fig.4.14 (the broken line). The discharge capacity increased slowly over the first 20 cycles, and then became very stable over the 1000 cycles. The average cell specific capacitance, efficiency, energy density and power density over 1000 cycles at 7.79 mA/cm<sup>2</sup> are shown in Table 4.6. The cell has the average cell specific capacitance of 12.20 F/g, ranging from 11.53 F/g to 12.26 F/g with the average efficiency of 79.01% ranging from 70.72% to 81.18%. The cell specific capacitance and efficiency were increased as a function of cycle life, which indicates that electrochemical performance of J2 was enhanced at 7.79 mA/cm<sup>2</sup> over the 1000 cycle life.

In Fig. 4.14, (Ragone plot at three current densities), J2 is shown the lowest energy density (11.95 Wh/kg) and the lowest power density (178.5 W/kg) at 7.79 mA/cm<sup>2</sup>. Theoretically, the capacitance should increase as the current density decreases under the same conditions, such as the increase at 20.46 mA/cm<sup>2</sup>. As expected, J2 at 7.79 mA/cm<sup>2</sup> should obtain the highest cell specific capacitance as well as the energy density. However, the self-discharge test conducted after the 20.46 mA/cm<sup>2</sup> cycling showed a long duration discharge of twenty-five days, which caused some of the electrolyte to be dried out. This would cause the diffusion resistance to increase significantly. The self-discharge measurement should be responsible for the perturbed energy density and the cell specific capacitance results.

Fig. 4.15 (c) shows the 2000<sup>th</sup>, the 2012<sup>th</sup>, the 2512<sup>th</sup>, the 2887<sup>th</sup> and the 3000<sup>th</sup> charge/discharge profiles of the cell at 7.79 mA/cm<sup>2</sup>. Table 5.3 shows the constant current charge/discharge times,  $\Delta V_{IR}$ , cell specific capacitances, efficiencies, energy and power densities for these cycles.

From the Fig. 4.15 (c) and Table 5.2, the  $\Delta V_{IR}$  at 2012<sup>th</sup> cycle was almost 2 times that of the first cycle (2001<sup>th</sup>), and then increased slightly from the 2012<sup>th</sup> cycle to the 3000<sup>th</sup> cycle, which indicates the internal resistance generally remained stable at this current density over the cycle life. As compared with the drastically increased  $\Delta V_{IR}$  at 31.16 mA/cm<sup>2</sup> and 20.46 mA/cm<sup>2</sup>, J2 showed a more stable performance at 7.79 mA/cm<sup>2</sup> over the cycle life. The charge time of the last cycle slightly decreased (6.03%) while the discharge time increased 5.23% as compared with the first cycle, which causes the increases in the cell specific capacitance and efficiency. These increases also demonstrate that the performance of the cell was gradually enhanced over 1000 cycles at 7.79 mA/cm<sup>2</sup>.

Table 5.3.

Comparison of the constant current charge/discharge times,  $\Delta V_{IR}$ , cell capacitances, efficiencies, energy, and power densities for the cycles at 7.79 mA/cm<sup>2</sup>.

Cycle number	Charge Time (s)	Discharge Time (s)	$\Delta V_{IR}$ (V)	Columbic Efficiency (%)	Energy Density (Wh/kg)	Power Density (W/kg)
1001	215.0	170.9	0.2906	81.67	20.96	441.6
1012	205.0	169.3	0.3266	81.81	20.91	444.5
1500	173.3	160.0	0.3597	91.01	19.91	448.0
1887	170.8	152.4	0.3637	90.33	18.58	438.9
2000	160.2	144.5	0.2676	87.27	17.98	448.1

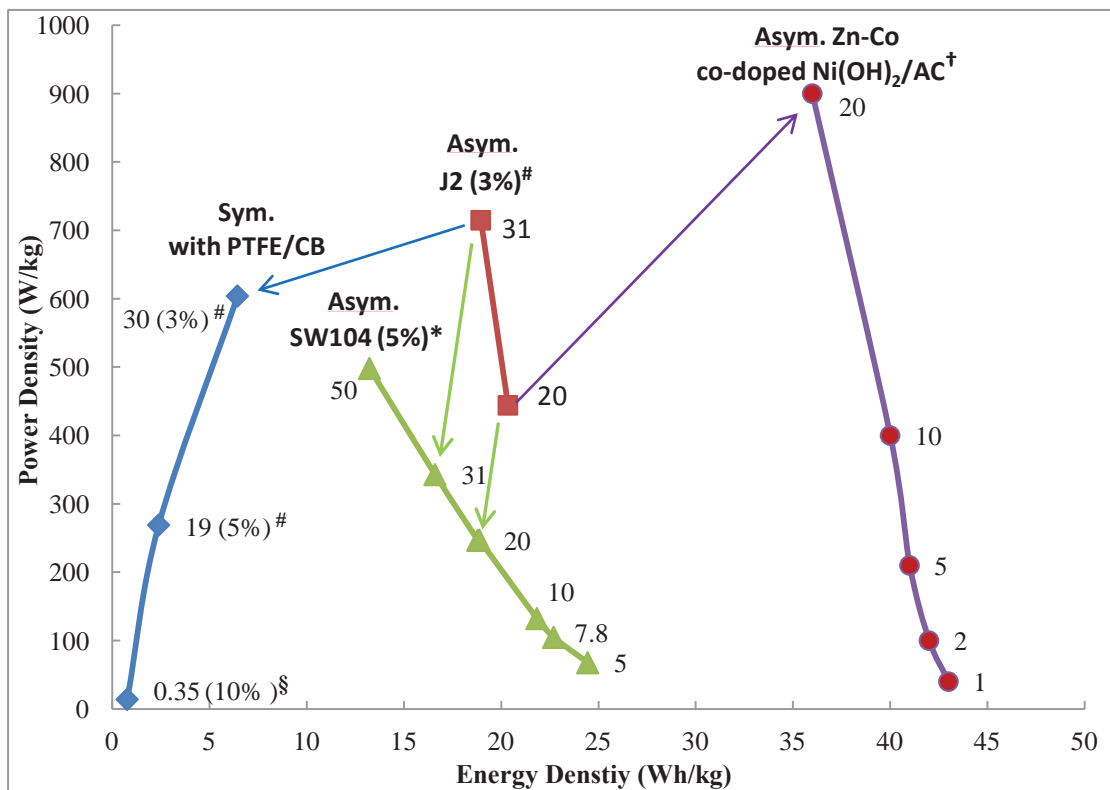
Because the self-discharge test interfered with the constant current density at 7.79 mA/cm<sup>2</sup>, the energy density at this current density was 1.9 times that of the 3 wt% symmetric cell (6.44 Wh/kg) and was only half of the best result (SW 104 at 5.0 mA/cm<sup>2</sup>) of Wen Nee Yeo.<sup>41</sup> The energy density of SW 104 at 7.79 was 22.7 Wh/kg. The power density was only one fourth of the 3 wt% symmetric cell (604.1 W/kg) and one third of the best result (SW 104 at 50.0 mA/cm<sup>2</sup>) of Wen Nee Yeo.<sup>41</sup> Because the relatively lower current density, 7.79 mA/cm<sup>2</sup>, as compared to 30.0 mA/cm<sup>2</sup> for the 3 wt% symmetric cell and 50.0 mA/cm<sup>2</sup> for the SW 104. The SW 104 as estimated had 104.8 W/kg power density at 7.79 mA/cm<sup>2</sup>.

In short, the lower current density should lead to improved properties. This perturbed performance at 7.79 mA/cm<sup>2</sup> is because of the self-discharge test and substantial internal resistance gained over 2000 cycles at relatively high current densities. On the other hand, the cycling performance at this relatively low current density was quite stable, which

can be used in the long cycle life test.

### 5.3 Comparison of Cell J2 with Previous Work and Literature

Energy densities and power densities for asymmetric cell J2 are compared with those of the 3 wt% symmetric capacitor and previous asymmetric literature values (see Fig. 5.1).



# this work, 3 and 5 wt% PTFE/CB symmetric cells (see Table 4.3); and asymmetric cell J2 (see Table 4.6).

§ from P. Sasthan Kuttipillai,<sup>40</sup>.

\* from W. N. Yeo,<sup>41</sup>.

† from J. H. Park, *et al.*<sup>14</sup>

Fig. 5.1. Ragone plot for the 3 wt% symmetric cell, asymmetric Ni(OH)<sub>2</sub>/AC cells, J2, SW 104, and Zn-Co co-doped Ni(OH)<sub>2</sub>/AC (numbers next to each point are the current densities, the PTFE/CB weight percentages are in parentheses).

As compared with the 3 wt% symmetric capacitor, asymmetric cell J2 has a much higher energy density – almost 3 times that of the symmetric cell, and a relatively higher

power density at a current density of 31 mA/cm<sup>2</sup> (see blue arrow). As compared with cell SW104, J2 has relatively higher power densities and comparable energy densities at the same current densities (see green arrows). As compared with the asymmetric capacitor data reported by Park, et al., cell J2 has a relatively lower energy density and power density – only half of that literature data at the same current density (see purple arrow). This is controlled by the negative electrode material, not the positive. The active carbon used in the Park, et al. cell, is expected to have a much higher specific capacitance as compared with the carbon black.

#### **5.4 Evaluation of the Cycle Life Testing of the Asymmetric Cells**

The discharge capacity as a function of cycle life for the asymmetric cells is depicted in Fig. 4.16. Table 4.7 summarizes the effective cycle life (cycled to 80% of rated capacity) as well as the average cell capacitance, energy and power density. When the 80% of initial discharge capacity was used to cut off the cycling, the asymmetric J2 has the longest cycle life of 11,505 cycles, followed by J1 with 8,292 cycles, while J3 has shortest cycle life of 2,457 cycles. Although J2 has the longest cycle life, the average efficiency was relatively lower as compared with J1 and J3. This low efficiency is mainly caused by the substantial internal resistance gained over the cycles at 31.16 mA/cm<sup>2</sup> and 20.46 mA/cm<sup>2</sup> (see the  $\Delta V_{IR}$  in Table 5.1 and 5.2). Because of the relatively high current, the J1 cell gained internal resistance more quickly, which of course will reduce the cycle life. Theoretically, the J3 cell is expected to have the longest cycle life because of the relatively low current density. However, J3 has the shortest cycle life and the discharge capacity decreased very rapidly even with the average efficiency of 97.10%. There are two possible reasons for this rapid discharge drop. The negative electrode for J3 was from batch B5 while J1 and J2 used negative electrodes from batch B3. The 3 wt% negative electrode of

B5 may be less stable than B3. The inadequate grinding or uneven PTFE dispersal can lead to variable performance of the PTFE/CB sheets. The various manual operations of the assembly process could also contribute to variations in cell performance.

Fig. 4.17 compares the average cell specific capacitance of J1, J2, and J3 at 5.58 mA/cm<sup>2</sup>, 7.79 mA/cm<sup>2</sup>, and 31.16 mA/cm<sup>2</sup>, respectively. J3 has the highest average cell specific capacitance of 25.48 F/g, followed by J2 16.65 F/g, and J1 has the lowest capacitance 8.079 F/g. This is because J3 used the lowest current density of 5.58 mA/cm<sup>2</sup> and J1 used the highest current density of 31.16 mA/cm<sup>2</sup>. The Ragone plot of J1, J2, and J3 is shown in Fig. 4.18. Among the three cells, J1 has the highest power density (618.9 W/kg) but lowest energy density (3.999 Wh/kg) because 31.16 mA/cm<sup>2</sup>, the highest current density, was applied. J3 has the highest energy density (24.84 Wh/kg) and intermediate power density (286.2 W/kg), which is mainly due to the high cell capacitance at 5.58 mA/cm<sup>2</sup>, the lowest current density. J2 has an intermediate energy density (14.35 Wh/kg) and the lowest power density (250.1 W/kg).

The 80% rated cycle lives of these three asymmetric cells (J1, J2, and J3) are much less than the SW66, which has 76,400 cycles.<sup>32</sup> The variations in manual assembling are the main reason for the reduced cycle life in the test.

## 5.5 Evaluation of XRD Characterization of Nickel Electrode

It has previously been shown by Raman spectroscopy that  $\alpha$ - and  $\gamma$ -nickel hydroxide have the same  $\alpha$ -type structure, that is, ABBCCA stacking (non-close packed).<sup>18</sup> Thus, it should be possible to interpret the XRD powder patterns in terms of this non-closed packed model, as opposed to the close packed,  $\beta$ -model. The observed XRD patterns will be predicted assuming several alternative structural models. Favorable comparison of calculated patterns with experimental patterns will then verify the proposed structures.



The experimental XRD patterns of seven compounds are shown in Fig. 4.24 and the peak positions are identified in Table 4.7. These 7 powder patterns can be interpreted in terms of 3 distinct patterns (deposited, charged, and discharged, including formed). The pattern of the deposited material is unique. The XRD patterns of the charged 1x and 10x samples are compared in Fig. 4.25, which shows that these two XRD patterns are almost identical. Fig. 4.26 compares XRD patterns of three discharged samples: formed, discharged 1x, and discharged 10x. The discharged 1x and 10x XRD patterns are almost the same except for the intensities of the  $12.68^\circ$  and  $19.02^\circ 2\theta$  peaks. The  $12.68^\circ 2\theta$  peak is very weak in the XRD pattern of discharged 1x, but is relatively strong in discharged 10x. On the contrary, the peak at  $19.02^\circ 2\theta$  has a higher relative intensity in the XRD pattern of the discharged 1x than the discharged 10x pattern. The peaks at  $12.68^\circ$  and  $66.68^\circ 2\theta$  in the discharged XRD patterns exactly match the peaks in the charged XRD patterns (Fig. 4.25), which indicates that the formed and discharged electrodes are not fully discharged at the 0.15 V cut-off discharge voltage.

In order to prove the  $12.68^\circ$  and  $66.68^\circ 2\theta$  peaks are from incomplete discharge, a 50% discharged sample was prepared and measured under the same conditions. The charge/discharge capacities and the XRD pattern of this sample are shown in Appendix A (Table A.1). The XRD pattern of the 50% discharged electrode is almost identical to the patterns of the discharged electrodes (Fig. A.2) except it exhibits increased intensities for the  $12.68^\circ$  and  $66.68^\circ 2\theta$  peaks. If these peaks are from the charged phase, a 50% discharge should present increased intensities. This is, therefore, consistent with the interpretation that these additional peaks are caused by the charged phase.

#### 5.5.1 Evaluation of the XRD Pattern for the Deposited Electrode

The calculation of the XRD pattern can be conducted by the assumption of a structural model and by defining the peak broadening at two experimental  $2\theta$  positions. For

the crystal structure definition, the following parameters should be defined (see Table 5.4): space group, lattice parameters, fractional coordinates and thermal parameters.

Electrochemically deposited nickel hydroxides are known to be  $\alpha$ -type materials. Comparison of the deposited electrode powder pattern and the JCPDS 22-444 standard card shows they have similar patterns.<sup>16</sup> Fig. 5.2 shows an example of how to verify the structure for the deposited electrode. An experimental pattern (black line) and two calculated patterns (red and blue lines) are compared in Fig. 5.2. The red pattern assumes small line broadening (0.005 at  $3^\circ 2\theta$  and 0.08 at  $40^\circ 2\theta$ ) and defines the unique position for each hkl diffraction line. The experimental pattern is clearly composed of broadened peaks which overlap (see section 3.5). The blue pattern uses greater broadening parameters (Table 5.4).

The question is, what is the structure of this  $\alpha$ -nickel hydroxide material? The proposed model is  $R\bar{3}m$ , non-close packed with the ABBCCA stacking. The proposed structural model will be supported by the good agreement between calculated and experimental patterns.

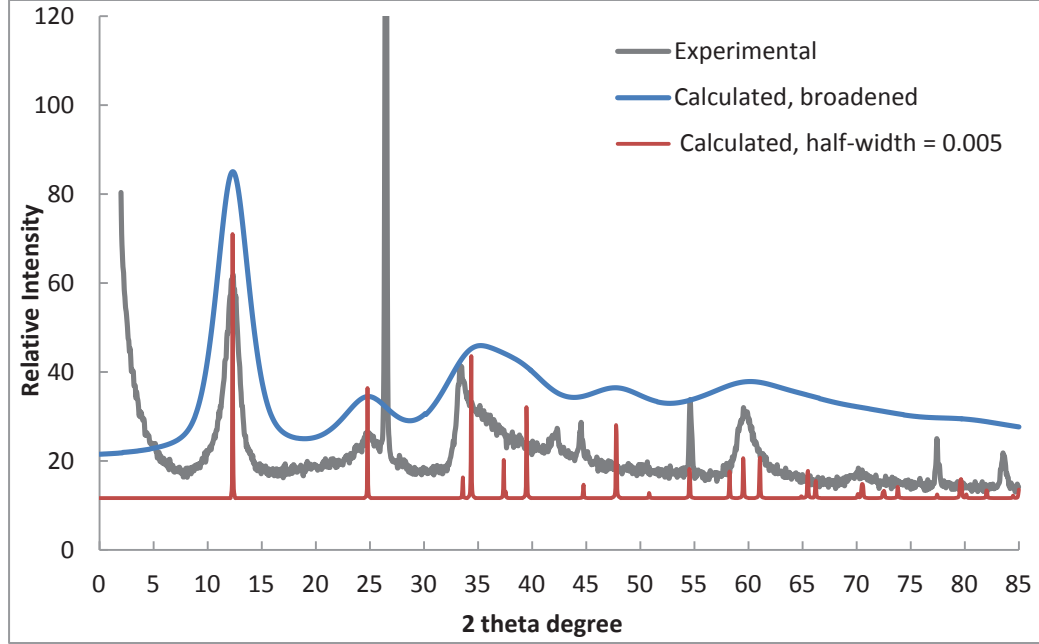


Fig. 5.2. XRD Powder Pattern Calculation (deposited,  $\alpha$ -material, ABBCCA stacking).

The  $R\bar{3}m$  space group can be defined in rhombohedral or hexagonal unit cells. The non-close packed,  $R\bar{3}m$  cell (ABBCCA stacking), has one formula unit per rhombohedral unit cell or three formula units per hexagonal cell. The lattice parameters with the rhombohedral cell ( $a_r$  and  $\alpha$ ) can be converted to the corresponding hexagonal axes ( $a_h$  and  $c_h$ ) by equations 5.1 to 5.4. Table 5.4 gives the input parameters for the XRD calculation. Fig. 5.3 shows experimental and calculated XRD patterns. Table 5.5 compares experimental and calculated  $2\theta$ ,  $hkl$ , and the relative intensities of the active mass in the deposited electrode.

$$a_h = 2a_r \sin \frac{\alpha}{2} \quad (5.1)$$

$$c_h = a_r \sqrt{9 - 12 \sin^2 \frac{\alpha}{2}} \quad (5.2)$$

$$a_r = \frac{1}{3} \sqrt{3a_h^2 + c_h^2} \quad (5.3)$$

$$\sin \frac{\alpha}{2} = \frac{3}{2 \sqrt{3 + \left(\frac{c_h}{a_h}\right)^2}} \quad (5.4)$$

The major peaks at  $12.32^\circ$ ,  $24.92^\circ$ ,  $33.72^\circ$ , and  $59.54^\circ$   $2\theta$  are fit very well (see black lines). The peak at  $47.79^\circ$   $2\theta$  of the calculated pattern was not seen or resolved in the experimental pattern (see red line). This broadened peak may be lost in the noise and background, perhaps worsened by the porous carbon foam. Otherwise, this  $R\bar{3}m$  model gives good agreement with experiment. This is consistent with the deposited sample,  $\alpha$ -Ni(OH)<sub>2</sub>, having the  $R\bar{3}m$  structure with ABBCCA stacking.

Table 5.4.

Input parameters for the  $R\bar{3}m$  structural model of the deposited electrode for the XRD powder pattern calculation.

Atom	Site Symmetry	Population Parameter	(x, y, z)	Thermal Parameter
Ni	1a	1	(0, 0, 0)	0.174
O(H)	2c	1	(0, 0, 0.377)	0.763
O(H <sub>2</sub> )	1b	0.667	(0, 0, 0.5)	0.763
Hexagonal: $a_h = 3.1027 \text{ \AA}$ , $c_h = 21.5352 \text{ \AA}$				
Rhombohedral: $a_r = 7.3986 \text{ \AA}$ , $\alpha = 24.2077^\circ$				
Space Group: $R\bar{3}m$ ( $D_{3d}^5$ )				
FWHM*: $1^\circ$ at $3^\circ$ $2\theta$ ; $8^\circ$ at $50^\circ$ $2\theta$				

\* FWHM: Full-Width at Half-Maximum

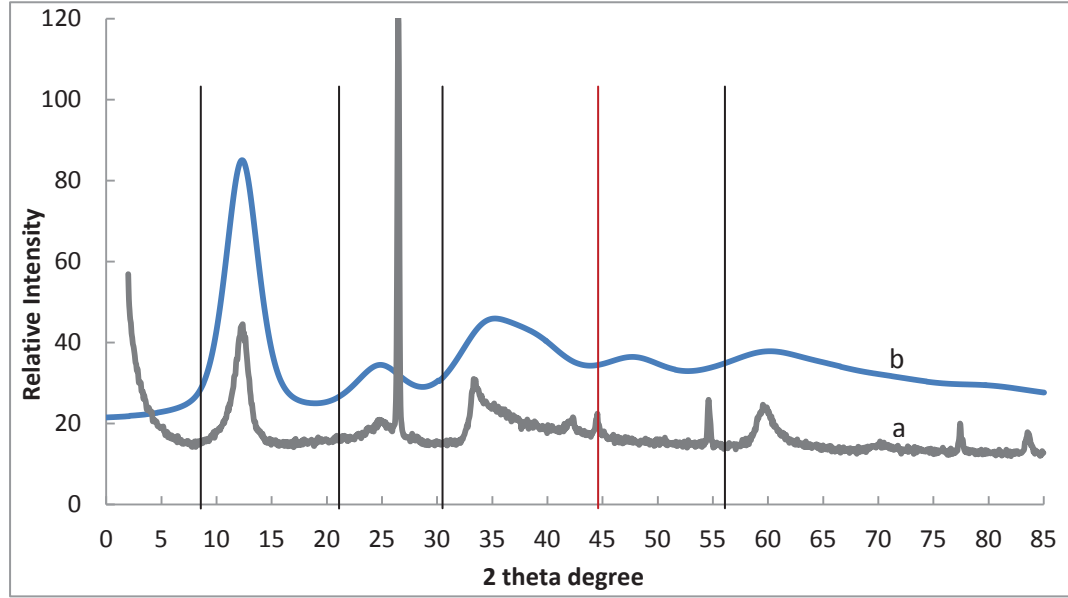


Fig. 5.3. Comparison of experimental XRD pattern of the deposited electrode (a) and the calculated XRD pattern (b) with  $R\bar{3}m$  structure.

Table 5.5.

The experimental XRD pattern of the deposited electrode and the calculated pattern with  $R\bar{3}m$  structure (see Table 5.4).

Experimental		Calculated with $R\bar{3}m$ structure			
2 $\theta$	d(Å)	2 $\theta$	d(Å)	A	h k l
12.32	7.178	12.32	7.178	100	0 0 3
24.92	3.570	24.79	3.589	17.69	0 0 6
33.60	2.665	33.58	2.666	4.02	1 0 1
33.72	2.656	34.37	2.607	23.87	0 1 2
37.38	2.404	37.37	2.404	6.15	1 0 4
		47.79	1.902	16.25	0 1 8
		59.54	1.551	7.33	1 1 0
60.02	1.540	61.06	1.516	7.41	1 1 3
70.38	1.336	70.48	1.335	1.98	1 1 4

### 5.5.2 Evaluation of the XRD Patterns for Charged 1x and Charged 10x Electrodes

The experimental XRD patterns of charged 1x and charged 10x electrodes are almost the same (see Fig. 4.25). This pattern is similar to literature  $\gamma$ -phase patterns. The  $3\gamma$ -NiOOH is known to be non-close packed (ABBCCA stacking), which has the  $R\bar{3}m$  structure.<sup>17</sup> The crystallographic input for these two samples is given in Table 5.6. Fig. 5.4 plots experimental and calculated XRD patterns. Table 5.7 summarizes experimental and calculated  $2\theta$ , hkl, and the relative intensities of the charged 1x and 10x electrodes.

The four major peaks at  $12.68^\circ$ ,  $25.52^\circ$ ,  $37.40^\circ$  and  $42.86^\circ$   $2\theta$  agree well with the calculated peaks —  $12.68^\circ$ ,  $25.52^\circ$ ,  $37.65^\circ$  and  $42.71^\circ$   $2\theta$  (see black lines in Fig. 5.4). Even the weak peaks at  $36.82^\circ$  and  $50.83^\circ$   $2\theta$  fit very well. From the calculation, it is found that the peak at  $66.68^\circ$   $2\theta$  is made up of two peaks ( $65.93^\circ$  and  $67.64^\circ$   $2\theta$ ). Overall, the calculated pattern matches the experimental pattern quite well, although the calculated peak at  $51.01^\circ$   $2\theta$  has more intensity than the corresponding peak at  $50.83^\circ$   $2\theta$  in the experimental pattern.

Thus, the charged 1x and 10x samples are  $3\gamma$ -NiOOH, having the  $R\bar{3}m$  structure. The deposited  $\alpha$ -phase is known to form  $3\gamma$  upon charge. These electrodes also experienced extensive overcharge (see Fig. 4.20 and 4.22); formation of the  $3\gamma$ -NiOOH phase is consistent with this overcharge.

Table 5.6.

Input parameters for  $R\bar{3}m$  structural model of the charged 1x and 10x electrodes in XRD calculation.

Atom	Site Symmetry	Population Parameter	(x, y, z)	Thermal Parameter
Ni	1a	1	(0, 0, 0)	0.174
O(H)	2c	1	(0, 0, 0.377)	0.763
O(H <sub>2</sub> )	1b	0.667	(0, 0, 0.5)	0.763
Hexagonal: $a_h = 2.8311 \text{ \AA}$ , $c_h = 20.9262 \text{ \AA}$				
Rhombohedral: $a_r = 7.1644 \text{ \AA}$ , $\alpha = 22.7912^\circ$				
Space Group: $R\bar{3}m$ ( $D_{3d}^5$ )				
FWHM*: $1^\circ$ at $3^\circ 2\theta$ ; $4^\circ$ at $50^\circ 2\theta$				

\* FWHM: Full-Width at Half-Maximum

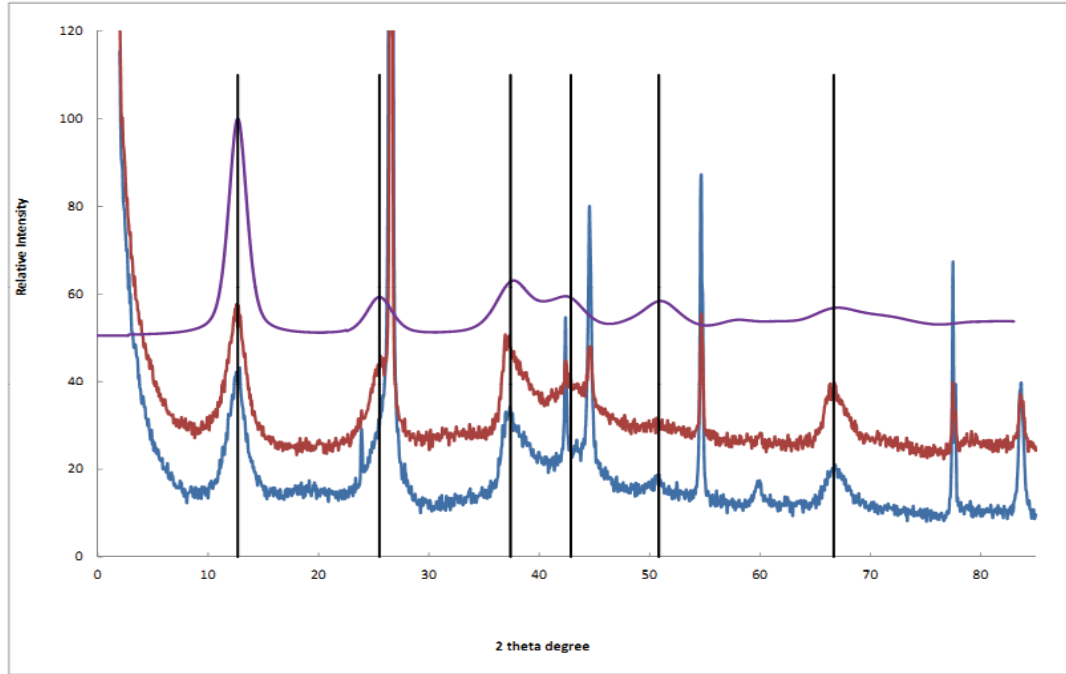


Fig. 5.4. Comparison of experimental XRD patterns of the charged 1x (a) and 10x (b) electrodes and calculated XRD pattern (c) with  $R\bar{3}m$  structure.

Table 5.7.

The experimental XRD pattern of the charged 1x and 10x electrodes and the calculated pattern with  $R\bar{3}m$  structure.

Experimental				Calculated with $R\bar{3}m$ structure			
Charged 1x		Charged 10x					
<u>2<math>\theta</math></u>	<u>d(Å)</u>	<u>2<math>\theta</math></u>	<u>d(Å)</u>	<u>2<math>\theta</math></u>	<u>d(Å)</u>	<u>A</u>	<u>h k l</u>
12.68	6.975	12.68	6.975	12.68	6.975	100	0 0 3
25.52	3.488	25.52	3.488	25.52	3.488	17.48	0 0 6
36.82	2.439	36.82	2.439	36.88	2.435	3.51	1 0 1
37.40	2.403	37.40	2.403	37.65	2.387	19.46	0 1 2
42.86	2.108	42.86	2.108	42.71	2.116	13.73	1 0 5
50.83	1.795	50.83	1.795	51.01	1.789	13.73	0 1 8
		60.02	1.540				
				65.93	1.416	5.34	1 1 0
66.68	1.402	66.68	1.402	67.46	1.387	5.58	1 1 3

### 5.5.3 Evaluation of the XRD Pattern for Discharged Electrodes

The powder patterns of the discharged electrodes contain peaks that are similar to the charged patterns, as well as additional peaks caused by the discharge. Incomplete discharge is indicated. The analysis of these patterns is complicated by the possibility of a discharged material aging to a  $\beta'$ -material.  $\beta'$  is a material formed by aging the discharged material in aqueous KOH. There are three possible combinations of materials that could be produced upon incomplete discharge: mixtures of  $2\alpha + 3\gamma$ , or  $2\beta + 3\beta$ , or  $\beta' + 3\gamma$ . In the first case, the active mass maintains the  $2\alpha/3\gamma$  cycle, with no aging. The discharge generates  $2\alpha$  and some  $3\gamma$  from the charge process still remains in the electrode. In the



second case, the active mass stays in the  $2\beta/3\beta$  cycle. The electrode will have  $2\beta$  and  $3\beta$  mixed when incompletely discharged, with no aging. In the third case, the electrode produces  $3\gamma$  due to the overcharging process. Some of the  $3\gamma$  turns to  $2\alpha$  in the discharge process, and then  $2\alpha$  is aged to  $\beta'$ . Consequently, the discharged electrode would contain the aged material ( $\beta'$ ) and remnant  $3\gamma$ . The second alternative ( $2\beta + 3\beta$ ) can be eliminated because the charged material is a  $3\gamma$  (see section 5.5.2). Crystal structure models are needed for the  $\beta'$ ,  $2\alpha$ , and  $3\gamma$  materials. The remnant  $3\gamma$  pattern is similar to the charged electrode  $3\gamma$  pattern, with  $R\bar{3}m$  symmetry and ABBCCA stacking (see section 5.5.2). A similar non-close packed model will be considered for  $2\alpha$ , a model which is similar to the  $\alpha$  model of section 5.5.1. A model with  $P\bar{3}m$  (ABAB stacking) will be considered for the aged material ( $\beta'$ ).

#### 5.3.3.1 Calculated XRD Pattern for the Formed Electrodes

The experimental XRD pattern of the formed sample (b) is shown in Fig. 4.24 and Fig. 4.26. The major 3 peaks at  $19.02^\circ$ ,  $34.28^\circ$  and  $38.56^\circ 2\theta$  agree with the JCPDS 72-2075 standard XRD card for the  $\beta'$ -Ni(OH)<sub>2</sub>.<sup>43</sup> The peaks in the XRD pattern of the formed sample are exactly same as the 50% discharged pattern except that the intensities of  $12.68^\circ$  and  $66.68^\circ 2\theta$  are different (see Table A.3 and Fig. A.3). A  $P\bar{3}m$  structural model is proposed; it has a close packed lattice (ABAB NiO<sub>2</sub> layer stacking).<sup>44</sup> Because the  $12.68^\circ$  and  $66.68^\circ 2\theta$  match peaks in the charged patterns (see Table 5.7), with the  $R\bar{3}m$  structure, these are assigned to un-discharged  $3\gamma$  (calculated in Table 5.6). The input files for the formed material with a  $P\bar{3}m$  structure are shown in Table 5.8. The experimental and calculated XRD patterns are plotted in Fig. 5.5. Table 5.9 compares experimental and calculated  $2\theta$ , hkl, and the relative intensities of the formed electrode.

The two peaks at  $19.02^\circ$  and  $59.92^\circ 2\theta$  match very well with the calculated  $\beta'$ -pattern (see black lines in Fig. 5.5). But the peaks at  $34.28^\circ$  and  $37.45^\circ 2\theta$  are shifted  $0.78^\circ$  and  $1.35^\circ 2\theta$  from the calculated  $33.50^\circ$  and  $38.80^\circ 2\theta$ , respectively (possibly because of

overlap with  $3\gamma$  peaks). Also, a calculated peak at  $52.02^\circ 2\theta$  was not seen in the experimental pattern. The  $3\gamma$  peaks at  $12.68^\circ$ ,  $25.52^\circ$ ,  $51.01^\circ$  and  $67.46^\circ 2\theta$  fit well with the calculated  $3\gamma$  peaks with the  $R\bar{3}m$  structure (see red lines in Fig. 5.5).

In short, the formed sample is a mixture of the aged  $\beta'$  and remnant  $3\gamma$ . The  $3\gamma$  remains because of incomplete discharge (see Fig. 4.19). After discharge, some of the  $3\gamma$  active mass transformed to  $2\alpha$ , which was aged to  $\beta'$  in the KOH environment. So the formed electrode has  $\beta'$  and  $3\gamma$  remnant. The overcharge is seen to be important because it assures return to the  $3\gamma$  from the  $\beta'$ .

Table 5.8.

Input parameters for the  $P\bar{3}m$  structural model of the formed electrode for the XRD powder pattern calculation.

Atom	Site Symmetry	Population Parameter	(x, y, z)	Thermal Parameter
Ni	1a	1	(0, 0, 0)	0.173
O	2d	1	(0.333, 0.667, 0.234)	0.764
Hexagonal: $a_h = 3.0849 \text{ \AA}$ , $c_h = 4.6620 \text{ \AA}$				
Space Group: $P\bar{3}m$ ( $D_{3d}^1$ )				
FWHM*: $1^\circ$ at $3^\circ 2\theta$ ; $4^\circ$ at $50^\circ 2\theta$				

\* FWHM: Full-Width at Half-Maximum.

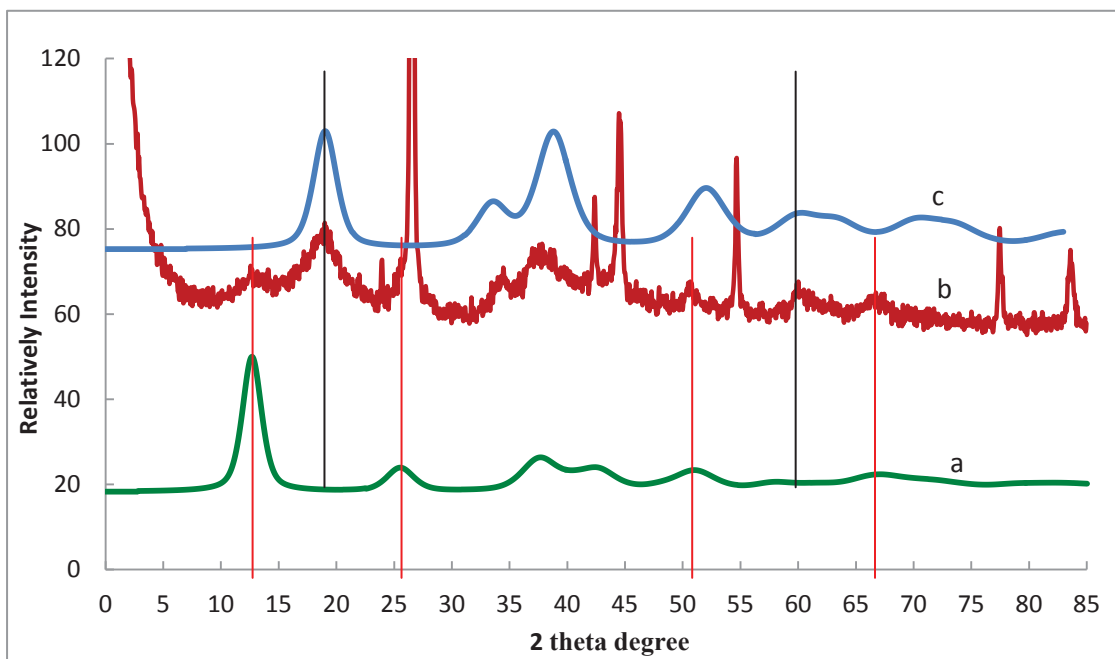


Fig. 5.5. Comparison of the experimental XRD pattern of the formed electrode (b) with the calculated XRD patterns of  $P\bar{3}m\ \beta'$  (c) and  $R\bar{3}m\ 3\gamma$  (a).

Table 5.9.

Comparison of the experimental XRD pattern with the calculated  $P\bar{3}m$  and  $R\bar{3}m$  patterns for the formed sample (see input in Table 5.8 and 5.6).

Experimental		Calculated with $P\bar{3}m$ ( $\beta'$ ) and $R\bar{3}m$ ( $3\gamma$ ) structures			
<u><math>2\theta</math></u>	<u><math>d(\text{\AA})</math></u>	<u><math>2\theta</math></u>	<u><math>d(\text{\AA})</math></u>	<u><math>A</math></u>	<u><math>h\ k\ l</math></u>
12.68	7.042	12.68 ( $3\gamma$ )	7.042	100	0 0 3
19.02	4.662	19.02 ( $\beta'$ )	4.662	100	0 0 1
25.52	3.488	25.52 ( $3\gamma$ )	3.488	17.48	0 0 6
34.28	2.614	33.50 ( $\beta'$ )	2.672	35.43	1 0 0
37.45	2.399	37.65 ( $3\gamma$ )	2.387	19.46	0 1 2
		38.80 ( $\beta'$ )	2.319	80.85	0 1 1
50.62	1.802	51.01 ( $3\gamma$ )	1.789	13.73	0 1 8
		52.03 ( $\beta'$ )	1.756	27.69	0 1 2
59.92	1.542	59.90 ( $\beta'$ )	1.543	20.59	1 1 0
66.68	1.402	67.46 ( $3\gamma$ )	1.387	5.58	1 1 3

#### 5.5.3.2 Evaluation of the XRD Patterns for Discharged 1x and 10x Electrodes

The XRD patterns of the discharged electrodes 1x and 10x are compared in Fig. 4.26. The peak positions of the discharged 1x sample are almost identical with the discharged 10x; however, the intensities of peaks at  $12.68^\circ$  and  $66.80^\circ$   $2\theta$  are different. These two peaks have been associated with the  $3\gamma$  phase (see Table 5.6), which can also be demonstrated by the 50% discharged sample (refer to section 5.5.3.1 and Table A.3). The remaining peaks are similar to those in the formed electrode (Table 5.9). The  $P\bar{3}m$  structure can again be used to calculate the XRD patterns of the  $\beta'$  phase in these discharged 1x and discharged 10x samples. The input parameters for the  $P\bar{3}m$ ,  $\beta'$  phase in these two discharged samples are given in Table 5.10. Table 5.11 compares experimental and calculated  $2\theta$ ,  $hkl$ , and the relative intensities for the discharged 1x and 10x electrodes.

The peaks at  $19.02^\circ$ ,  $33.78^\circ$ ,  $38.47^\circ$ , and  $59.92^\circ$   $2\theta$  match very well with the calculated pattern (see black lines in Fig. 5.6). But a  $52.02^\circ$   $2\theta$  peak, that was predicted in the calculated  $\beta'$  pattern, was not observed in the experimental patterns. The  $3\gamma$  peaks at  $12.68^\circ$ ,  $51.01^\circ$  and  $67.46^\circ$   $2\theta$  agree with the calculated  $3\gamma$  pattern with the  $R\bar{3}m$  structure (see red lines in Fig. 5.6).

Above all, the discharged 1x sample is mainly  $\beta'$ -Ni(OH)<sub>2</sub> and the discharged 10x is a mixture of the  $\beta'$  and  $3\gamma$  phases (see Fig. 4.21 and 4.23). The  $3\gamma$  peaks are formed by the overcharging, and incomplete discharge leaves the remnant  $3\gamma$ .

Table 5.10.

Input parameters for a  $P\bar{3}m$  structural model of the discharged 1x and 10x electrodes for the XRD powder pattern calculation.

Atom	Site Symmetry	Population Parameter	(x, y, z)	Thermal Parameter
Ni	1a	1	(0, 0, 0)	0.173
O	2d	1	(0.333, 0.667, 0.234)	0.764
Hexagonal: $a_h = 3.0858 \text{ \AA}$ , $c_h = 4.6620 \text{ \AA}$				
Space Group: $P\bar{3}m$ ( $D_{3d}^1$ )				
FWHM*: $1^\circ$ at $3^\circ 2\theta$ ; $4^\circ$ at $50^\circ 2\theta$				

\*FWHM: Full-Width at Half-Maximum.

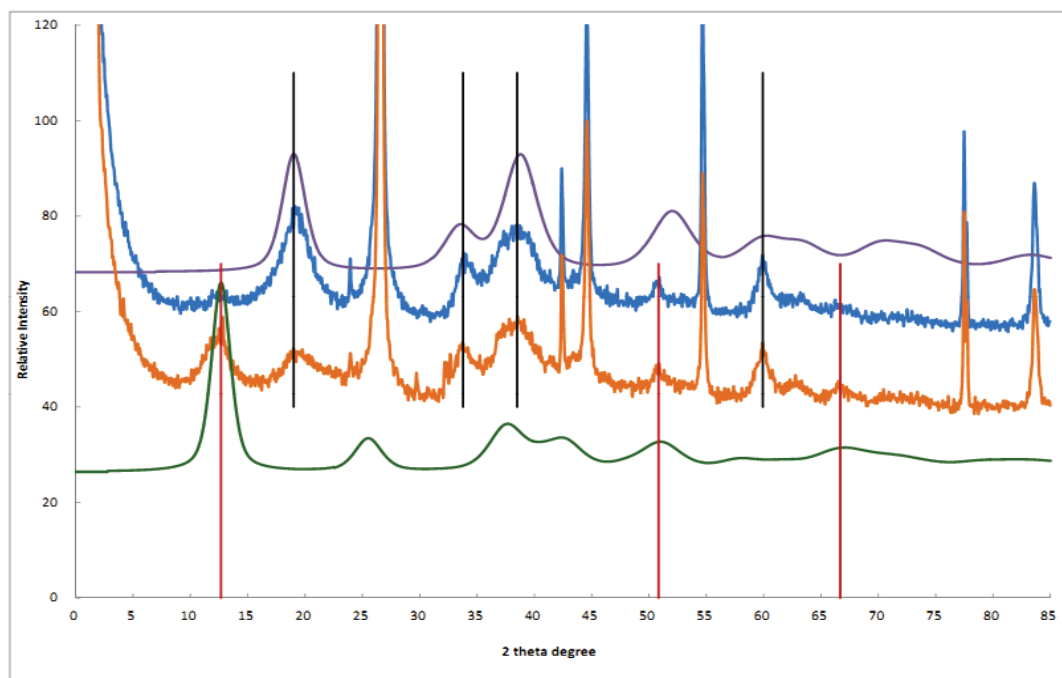


Fig. 5.6. Comparison of experimental XRD patterns: the discharged 1x (c) and discharged 10x (b), with the calculated  $P\bar{3}m\ \beta'$  pattern (d) and the calculated  $R\bar{3}m\ 3\gamma$  pattern (a).

Table 5.11.

Comparison of the experimental XRD patterns for the discharged 1x and 10x electrodes with the calculated pattern with  $P\bar{3}m$  and  $R\bar{3}m$  structures.

Experimental				Calculated with $P\bar{3}m$ ( $\beta'$ ) and $R\bar{3}m$ ( $3\gamma$ ) structures			
Discharged 1x		Discharged 10x					
<u>2<math>\theta</math></u>	<u>d(Å)</u>	<u>2<math>\theta</math></u>	<u>d(Å)</u>	<u>2<math>\theta</math></u>	<u>d(Å)</u>	<u><math>\Delta</math></u>	<u>h k l</u>
12.68*	6.975	12.68	6.975	12.68 ( $3\gamma$ )	6.975	100	0 0 3
19.02	4.662	19.02	4.662	19.02 ( $\beta'$ )	4.662	100	0 0 1
33.78	2.654	33.78	2.654	33.50 ( $\beta'$ )	2.672	35.43	1 0 0
38.47	2.338	38.47	2.338	38.80 ( $\beta'$ )	2.319	80.85	0 1 1
50.72*	1.798	50.72	1.798	51.01 ( $3\gamma$ )	1.789	13.73	0 1 8
				52.02( $\beta'$ )	1.757	27.70	1 0 2
59.92	1.542	59.92	1.542	59.90 ( $\beta'$ )	1.543	20.59	1 1 0
62.96	1.475	62.96	1.475	63.45 ( $\beta'$ )	1.465	18.73	1 1 1
66.68*	1.402	66.68	1.402	67.46 ( $3\gamma$ )	1.387	5.58	1 1 3

\* extremely weak peak.

## CHAPTER 6

### CONCLUSIONS AND FUTURE WORK

#### 6.1 Conclusions

##### 6.1.1 Conclusions: Symmetric Capacitors

The electrochemical performance of the 3 wt% and 5 wt% PTFE/CB sheets were examined for their suitability as negative electrodes in the symmetric aqueous cells using CV and constant current tests. The CV measurements prove that the 3 wt% and 5 wt% symmetric cells are typical double-layer capacitors, with the 3 wt% being more ideal. The 3 wt% cell has the highest specific single electrode capacitance (121.8 F/g), energy density (6.44 Wh/kg), and power density (604.1 W/kg). The additional PTFE in the 5 wt% and 10 wt% cells is seen to be detrimental. BET surface area and effective resistance for the 3 wt%, 5 wt%, and 10 wt% PTFE/CB sheets were measured. These two are the primary requirements for the active carbon to serve as an electrode in symmetric cells. Among the three types of PTFE/CB sheets, the 3 wt% sheet has the largest BET surface area (1239 m<sup>2</sup>/g) and the lowest ER (0.3618 ohm/cm), followed by the 5 wt% sheet (1237 m<sup>2</sup>/g and 0.3887 ohm/cm), while the 10 wt% sheet has the smallest 967 m<sup>2</sup>/g surface area and highest 0.4125 ohm/cm ER. These are the ultimate reasons for the different CV and constant current cycling results for the 3 wt%, 5 wt%, and 10 wt% symmetric cells.

##### 6.1.2 Conclusions: Asymmetric Capacitors

3 wt% PTFE/CB negative electrodes were used in the asymmetric cells (J1, J2, and J3) because the 3 wt% results were shown to be optimum in the above section. Asymmetric cells with nickel hydroxide supported on carbon foam as the positive electrode were



fabricated and examined over a wide range of current densities. Cell J2 displayed the maximum energy density (19.94 Wh/kg) and specific cell capacitance (20.35 F/g) at 20.46 mA/cm<sup>2</sup>. The highest power density (714.8 W/kg) was obtained at 31.16 mA/cm<sup>2</sup> due to the relatively high current. The cycle life tests show that cell J2 had the most stable electrochemical performance with the longest rated cycle life (11,505 cycles to 80% discharge capacity), followed by cell J1 (8,292 cycles). J3 had only 2,547 cycles. However, J3 gave the highest specific cell capacitance (25.48 F/g) and highest efficiency (> 97%) among the three cells.

### 6.1.3 Conclusions: XRD Characterization of the Positive Electrode

Based on the calculated XRD patterns, the deposited electrode is  $\alpha$ -Ni(OH)<sub>2</sub> with the non-close packed  $R\bar{3}m$  structure (ABBCCA stacking), with  $a_h=3.1027\text{\AA}$ ,  $c_h=21.5352\text{\AA}$  for an hexagonal cell. The XRD patterns of charged 1x and 10x are almost identical, containing  $3\gamma$ -NiOOH. These two samples have been fitted with the same  $R\bar{3}m$  structure, with  $a_h=2.8311\text{\AA}$  and  $c_h=20.9262\text{\AA}$ . The three discharged samples, the formed electrode, the discharged 1x, and 10x electrodes are mixtures of  $\beta'$ -Ni(OH)<sub>2</sub> and  $3\gamma$ -NiOOH because of extensive overcharging, aging, and incomplete discharge. The  $\beta'$  phase in these 3 electrodes has the  $P\bar{3}m$  structure (with close packed, ABAB stacking). The lattice parameters differed slightly for the formed ( $a_h=3.0849\text{\AA}$  and  $c_h=4.6620\text{\AA}$ ) and the two discharged electrodes ( $a_h=3.0858\text{\AA}$  and  $c_h=4.6620\text{\AA}$ ). The  $3\gamma$  content varied in these 3 electrodes. It is apparent that the  $\beta'$ -phase aged very quickly from the  $2\alpha$  in the aqueous KOH, the  $2\alpha$  forming upon discharge of the  $3\gamma$ .

## 6.2 Future Work

This work has proved that the asymmetric capacitor using a carbon black negative

electrode and a nickel hydroxide/carbon foam positive electrode has stable performance. The XRD powder pattern analyses defined the content of the positive electrodes during cycling. Further testing and improvement are needed to understand the reasons for cell failure, to achieve higher specific capacitance, energy density, and power density, and to identify under what conditions the  $3\gamma$  will discharge to a stable  $2\alpha$  and how to obtain full discharge of the  $3\gamma$ . Two categories of improvement are listed in the following:

(1) Negative electrode

- ✓ Find different types of active carbon to obtain higher specific capacitance of the asymmetric cell because the capacitance of the cell is limited by the negative electrode.
- ✓ Apply impedance tests, IR, Raman, SEM, TEM and BET measurements on the fresh and the cycled negative electrodes to identify the reasons for cell failure.

(2) Positive electrode

- ✓ Optimize the mass ratio of the positive electrode and negative electrode to achieve higher capacitance, energy density and power density.
- ✓ Define the optimum charge and discharge cut-off voltages and current density to extend the cycle life of the cell.
- ✓ Identify the charge and discharge conditions for nickel active mass to stay in  $2\alpha/3\gamma$  or  $2\beta/3\beta$  cycles.

## REFERENCES

1. D. Linden, Handbook of Batteries, 4<sup>th</sup> ed, pp. 265-265. Elsevier, Maryland Heights, MO, 1995,
2. B. E. Conway, Electrochemical Supercapacitors: Scientific Fundamentals and Technological Applications, Kluwer Academic/Plenum, New York, 1999.
3. P. Simon, Y. Gogotsi, "Materials for electrochemical capacitors," *Nature Materials*, **7** [11] 845-854 (2008).
4. I. Tanahashi, A. Yoshida, A. Nishino, "Electrochemical Characterization of Activated Carbon-Fiber Cloth Polarizable Electrodes for Electric Double-Layer Capacitors," *Journal of the Electrochemical Society*, **137** [10] 3052-3056 (1990).
5. T. Morimoto, K. Hiratsuka, Y. Sanada, K. Kurihara, "Electric double-layer capacitor using organic electrolyte," *Journal of Power Sources*, **60** [2] 239-247 (1996).
6. Y. R. Nian, H. S. Teng, "Nitric acid modification of activated carbon electrodes for improvement of electrochemical capacitance," *Journal of the Electrochemical Society*, **149** [8] A1008-A1014 (2002).
7. Q. Deyang, "Studies of the activated carbons used in double-layer supercapacitors," *Journal of Power Sources*, **109** [2] 403-411 (2002).
8. S. A. Kazaryan, G. G. Kharisov, S. V. Litvinenko, V. I. Kogan, "Self-discharge related to iron ions and its effect on the parameters of HES PbO<sub>2</sub>|H<sub>2</sub>SO<sub>4</sub>|C systems," *Journal of the Electrochemical Society*, **154** [8] (2007).
9. A. I. Beliakov, A. M. Brintsev, "Proceeding of the 7th International Seminar on Double Layer Capacitors and Similar Energy Storage Devices," Florida Educational Seminars, 1997.

10. D. Villers, D. Jobin, C. Soucy, D. Cossement, R. Chahine, L. Breau, D. Belanger, "The influence of the range of electroactivity and capacitance of conducting polymers on the performance of carbon conducting polymer hybrid supercapacitor," *Journal of the Electrochemical Society*, **150** [6] A747-A752 (2003).
11. Y. Wang, Y. Xia, "Hybrid Aqueous Energy Storage Cells Using Activated Carbon and Lithium-Intercalated Compounds," *Journal of the Electrochemical Society*, **153** [2] A450-A454 (2006).
12. J. P. Zheng, T. R. Jow, "High energy and high power density electrochemical capacitors," *Journal of Power Sources*, **62** [2] 155-159 (1996).
13. J. Chang, C. Lin, W. Tsai, "Manganese oxide/carbon composite electrodes for electrochemical capacitors," *Electrochemistry Communications*, **6** [7] 666-671 (2004).
14. J. H. Park, S. Kim, O. O. Park, J. M. Ko, "Improved asymmetric electrochemical capacitor using Zn-Co co-doped Ni(OH)<sub>2</sub>; positive electrode material," *Applied Physics A: Materials Science & Processing*, **82** [4] 593-597 (2006).
15. H. Bode, K. Dehmelt, J. Witte, "Zur kenntnis der nickelhydroxidelektrode—I. Über das nickel (II)-hydroxidhydrat," *Electrochimica Acta*, **11** [8] 1079-1087 (1966).
16. P. L. Loyselle, P. J. Karjala, B. C. Cornilsen, "A point-defect model for nickel electrode structures," *Journal of the Electrochemical Society*, **133** [8] C298-C298 (1986).
17. B. C. Cornilsen, P. J. Karjala, P. L. Loyselle, "Structural models for nickel electrode active mass," *Journal of Power Sources*, **22** [3-4] 351-357 (1988).
18. B. C. Cornilsen, X. Y. Shan, P. L. Loyselle, "Structural comparison of nickel electrodes and precursor phases," *Journal of Power Sources*, **29** [3-4] 453-466 (1990).
19. H. I. Becker, "Low voltage electrolytic capacitor," U.S. Patent, 2 800 616, 1957.

20. D. I. Boos, "electrolytic capacitor having carbon paste electrodes," U.S. Patent, 3 536 963, 1970.
21. S. Trasatti, G. Buzzanca, "Ruthenium dioxide: A new interesting electrode material. Solid state structure and electrochemical behaviour," *Journal of Electroanalytical Chemistry and Interfacial Electrochemistry*, **29** [2] A1-A5 (1971).
22. B. E. Conway, W. G. Pell, T. C. Liu, "Diagnostic analyses for mechanisms of self-discharge of electrochemical capacitors and batteries," *Journal of Power Sources*, **65** [1-2] 53-59 (1997).
23. C. Lin, J. A. Ritter, B. N. Popov, "Characterization of sol-gel-derived cobalt oxide xerogels as electrochemical capacitors," *Journal of the Electrochemical Society*, **145** [12] 4097-4103 (1998).
24. S. C. Pang, M. A. Anderson, T. W. Chapman, "Novel electrode materials for thin-film ultracapacitors: Comparison of electrochemical properties of sol-gel-derived and electrodeposited manganese dioxide," *Journal of the Electrochemical Society*, **147** [2] 444-450 (2000).
25. K. W. Nam, K. B. Kim, "A study of the preparation of NiO(x) electrode via electrochemical route for supercapacitor applications and their charge storage mechanism," *Journal of the Electrochemical Society*, **149** [3] A346-A354 (2002).
26. M. John R, "Electrochemical capacitor thermal management issues at high-rate cycling," *Electrochimica Acta*, **52** [4] 1703-1708 (2006).
27. J. R. Miller, A. F. Burke, "Electrochemical capacitors: challenges and opportunities for real-world applications," *Electrochemical Society Interface*, **17** [1] (2008).
28. R. Kotz, M. Carlen, "Principles and applications of electrochemical capacitors," *Electrochimica Acta*, **45** [15-16] 2483-2498 (2000).
29. D. M. Zogbi, "Proceedings of the 6th International Seminar on Double Layer Capacitors and Similar Energy Storage Devices," Florida Educational Seminar, 1996.

30. V. Wouk, "Hybrid Electric Vehicles," *Scientific American*, **45** (1997).
31. J. H. Park, O. O. Park, K. H. Shin, C. S. Jin, J. H. Kim, "An Electrochemical Capacitor Based on a  $\text{Ni}(\text{OH})_2$  /Activated Carbon Composite Electrode," *Electrochemical and Solid-State Letters*, **5** [2] H7-H10 (2002).
32. M. B. Chye, "Development and Characterization of a Rechargeable Carbon Foam Electrode Containing Nickel Oxyhydroxide Active Mass"; Ph.D. Dissertation. Michigan Technological University, Houghton, 2011.
33. B. C. Cornilsen, "The nonstoichiometric, solid solution structural model for nickel electrode active mass," *Selected Battery Topics. Proceedings of the Symposia (Electrochemical Society Proceedings Vol.98-15)* (1999).
34. V. Srinivasan, B. C. Cornilsen, J. W. Weidner, "A nonstoichiometric structural model to characterize changes in the nickel hydroxide electrode during cycling," *Journal of Solid State Electrochemistry*, **9** [2] 61-76 (2005).
35. Z. Xu, "XAS and XRD Structural Study of Nickel Electrode Materials (Part I) and FTIR Quantitative Analysis of Mineral Mixtures (Part II)"; Ph.D. Dissertation. Michigan Technological University, Houghton, 1999.
36. R. Barnard, C. F. Randell, F. L. Tye, "Studies concerning charged nickel hydroxide electrodes I. Measurement of reversible potentials," *Journal of Applied Electrochemistry*, **10** [1] 109-125 (1980).
37. R. Barnard, C. F. Randell, "Studies concerning charged nickel hydroxide electrodes. VI. Voltammetric behaviour for pre-cycled electrodes," *Journal of Applied Electrochemistry*, **13** [1] 27-38 (1983).
38. C. Baerlocher, L. B. McCusker, D. H. Olson, Atlas of Zeolite Framework Types, Elsevier, Amsterdam, 2007.
39. C. R. Hubbard, S. M. Lederman, and N. P. Pyrras, A least Squares Unit Cell Refinement Program, JCPDS-NBS\*LSQ82, U.S. National Bureau of Standards, Washington, DC, and JCPDS-International Center for Diffraction Data, 1601 Park Lane, Swarthmore, PA 19081, 1982; Updated to Windows by S.I. Zdziszynski and S.T. Mixture, NYS College of Ceramics, Alfred, NY, 1998.

40. P. S. Kuttipillai, "Performance Evaluation of A Novel Asymmetric Capacitor Using A Light-Weight, Carbon Foam Supported Nickel Electrode "; Master Thesis. Michigan Technological University, Houghton, 2011.
41. W. N. Yeo, "Development and Testing of An Asymmetric Capacitor with A Nickle-Carbon Foam Positive Electrode"; Ph.D. Dissertation. Michigan Technological University, Houghton, 2011.
42. A. Singh, B. C. Cornilsen, M. E. Mullins, T. N. Rogers, "Nickel hydroxide impregnated carbon foam electrodes for rechargeable nickel batteries," U.S. Patent Application, 2006 0024583, 15 July, 2005.
43. A. Szytula, A. Murasik, M. Balanda, "Neutron Diffraction Study of  $\text{Ni}(\text{OH})_2$ ," *physica status solidi (b)*, **43** [1] 125-128 (1971).
44. O. Glemser, J. Einerhand, "Über höhere Nickelhydroxyde," *Zeitschrift für anorganische Chemie*, **261** [1-2] 26-42 (1950).

# APPENDIX A

## PREPARATION AND XRD CHARACTERIZATION OF THE 50 % DISCHARGED ELECTRODE

Table A.1.

The capacities, depth of discharge (discharged to 0.0 V), cut off charge voltage, the charge and discharge times of the formation and cycling processes for the 50% discharged electrode (after 6<sup>th</sup> cycle).

Formation process for the 50% discharged electrode, Formed-2 (3-24-2012), at 70 mA/cm <sup>2</sup> for the 1 <sup>st</sup> cycle and 20 mA/cm <sup>2</sup> for 2x to 5x cycles						
Cycle Number	Charge Cap (Ah)	Discharge Cap (Ah)	DOD	V <sub>cut off</sub> Charge (V)	Charge Time (s)	Discharge Time (s)
1	0.1632	0.0109	0.067	0.614	1740.0	116.3
2	0.0531	0.0667	1.255	0.524	1981.7	2490.5
3	0.0483	0.0397	0.822	0.461	1800.0	1481.9
4	0.0483	0.0398	0.823	0.485	1800.0	1485.0
5	0.1632	0.0109	0.067	0.614	1740.0	116.3
Five cycles for 50% Discharged electrode with 50% discharge in the 6 <sup>th</sup> cycle at 10 mA/cm <sup>2</sup> (3-26-2011)						
Cycle Number	Charge Cap (Ah)	Discharge Cap (Ah)	DOD	V <sub>cut off</sub> Charge (V)	Charge Time (s)	Discharge Time (s)
1	0.0742	0.0895	1.207	0.502	5532.7	6678.7
2	0.0668	0.0540	0.809	0.464	4980.0	4027.7
3	0.0668	0.0559	0.838	0.472	4980.0	4172.7
4	0.0668	0.0557	0.834	0.477	4980.0	4155.6
5	0.0668	0.0550	0.823	0.482	4980.0	4101.3
6	0.0668	0.0331	0.0496	0.489	4980.0	2050.6



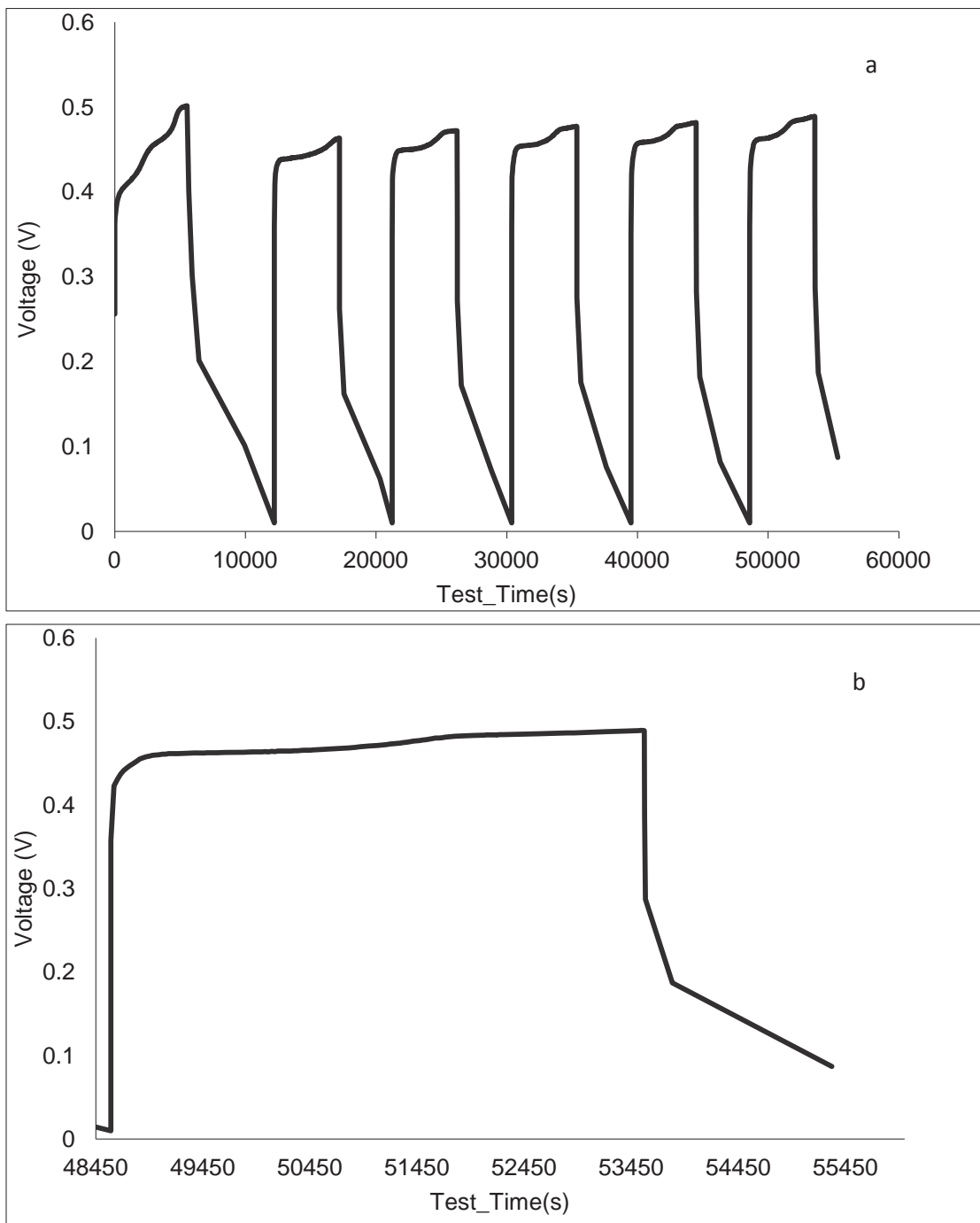


Fig. A.1. Potential vs. time response for the 6 cycle preparation of the 50% discharged sample (a) with an expansion of the last 50% discharge cycle (b) at 10 mA/cm<sup>2</sup> versus a Hg/HgO reference electrode.

Table A.2.

Input parameters for the  $P\bar{3}m$  structural model of the 50% discharged sample for the XRD powder pattern calculation.

Atom	Site Symmetry	Population Parameter	(x, y, z)	Thermal Parameter
Ni	1a	1	(0, 0, 0)	0.173
O	2d	1	(0.333, 0.667, 0.234)	0.764
Hexagonal: $a_h = 3.0849 \text{ \AA}$ , $c_h = 4.6620 \text{ \AA}$				
Space Group: $P\bar{3}m$ ( $D_{3d}^1$ )				
FWHM*: $1^\circ$ at $3^\circ 2\theta$ ; $4^\circ$ at $50^\circ 2\theta$				

\* FWHM: Full-Width at Half-Maximum.

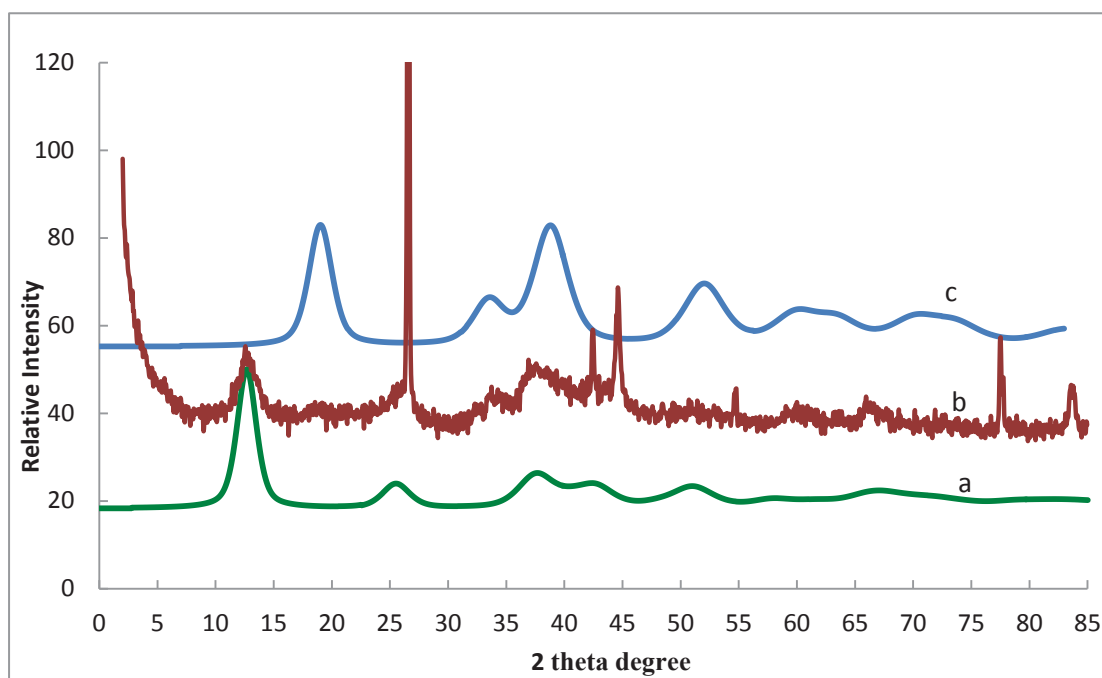


Fig. A.2. Comparison of experimental XRD pattern of the 50% discharged electrode, in the 6<sup>th</sup> cycle (b) with the calculated XRD patterns of  $P\bar{3}m \beta'$  (c) and  $R\bar{3}m \gamma$  (a).

Table A.3.

Comparison of the experimental XRD pattern of the 50% discharged sample and the calculated patterns with the  $P\bar{3}m$  and  $R\bar{3}m$  structures.

Experimental		Calculated with $P\bar{3}m$ ( $\beta'$ ) and $R\bar{3}m$ ( $3\gamma$ ) structures			
$2\theta$	$d(\text{\AA})$	$2\theta$	$d(\text{\AA})$	$A$	$hkl$
12.68	7.042	12.68 ( $3\gamma$ )	7.042	100	0 0 3
19.02	4.662	19.02 ( $\beta'$ )	4.662	100	0 0 1
34.28	2.614	33.50 ( $\beta'$ )	2.672	35.43	1 0 0
37.45	2.399	37.65 ( $3\gamma$ )	2.387	19.46	0 1 2
		38.80 ( $\beta'$ )	2.319	80.85	0 1 1
50.62	1.802	51.01 ( $3\gamma$ )	1.789	13.73	0 1 8
		52.03 ( $\beta'$ )	1.756	27.69	0 1 2

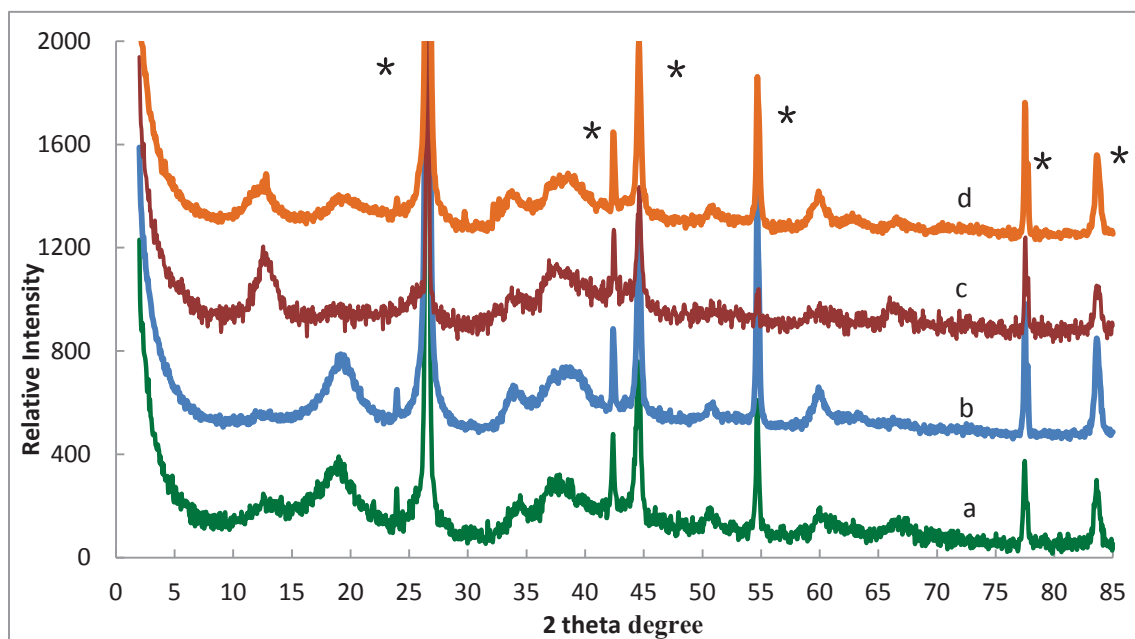


Fig. A.3. Comparison of experimental XRD patterns of the formed (a), the discharged 1x (b), the 50% discharged (c), and the discharged 10x (d) electrodes (\* peaks are from carbon foam).

# APPENDIX B

## IR SPECTRA OF THE CHEMICALLY PREPARED NICKEL COMPOUNDS

### B. 1 Sample Preparation

Table B.1.  
Preparation of the Nickel Hydroxide/Oxyhydroxide Compounds

Sample number	Sample Description	Sample Preparation
1 (3/18/11)	Initially oxidized by P.Sasthan Kuttipillai	Original material was oxidized in KOH/Br <sub>2</sub> and was intended to be a gamma NiOOH with K <sup>+</sup> in the structure by P. Sasthan Kuttipillai.
2 (4/15/11)	Reduced no. 1 by JJ	Sample no.1 was reduced in ethanol three times, then washed in DI water, centrifuged and dried.
3 (5/4/11)	Re-oxidized no. 1 by JJ	Sample no. 1 was oxidized again in KOH/Br <sub>2</sub> , washed in DI water, centrifuged, and dried. (no.1 had reduced in air).
4 (6/13/11)	Heated sample by JJ	Sample no.2 was heated at 800C for 4 hours and slowly cooled down at rate of 10 C/min.
5 (6/15/11)	Re-oxidized no.4 by JJ	Sample no.4 was re-oxidized in KOH/Br <sub>2</sub> , washed with DI water, centrifuged and dried.

## B. 2 IR Spectra

### (a) IR Spectrum of Compound No. 2

Scan conditions for compound no. 2 (reduced sample): A KBr pellet of sample no. 2 was prepared and measured on the Matson FTIR instrument, Galaxy Series, FTIR 3000, with 1000 scans. The resolution was  $8\text{ cm}^{-1}$ . This sample is a mix of  $\beta$ - and  $\gamma$ -type materials (possibly some  $\alpha$ ).

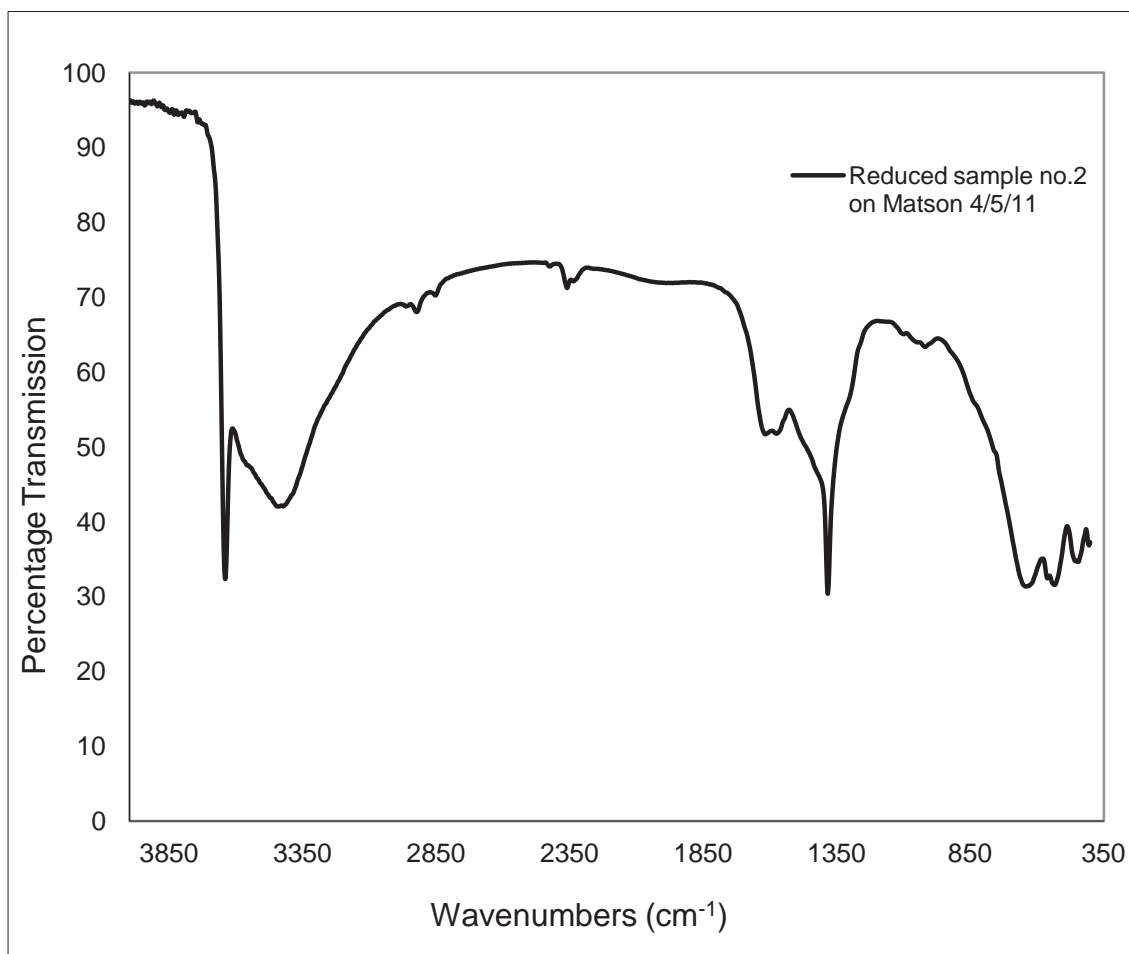


Fig. B.1. IR spectrum of sample no. 2 (reduced).

(b) IR Spectrum of Compound No. 3

Scan conditions for compound no. 3 (re-oxidized sample): A KBr pellet for sample no. 3 was prepared and measured on the Bruker, IFS-66 FTIR instrument with 500 scans. The resolution was  $4\text{ cm}^{-1}$ . This is a  $\gamma$ -type IR.

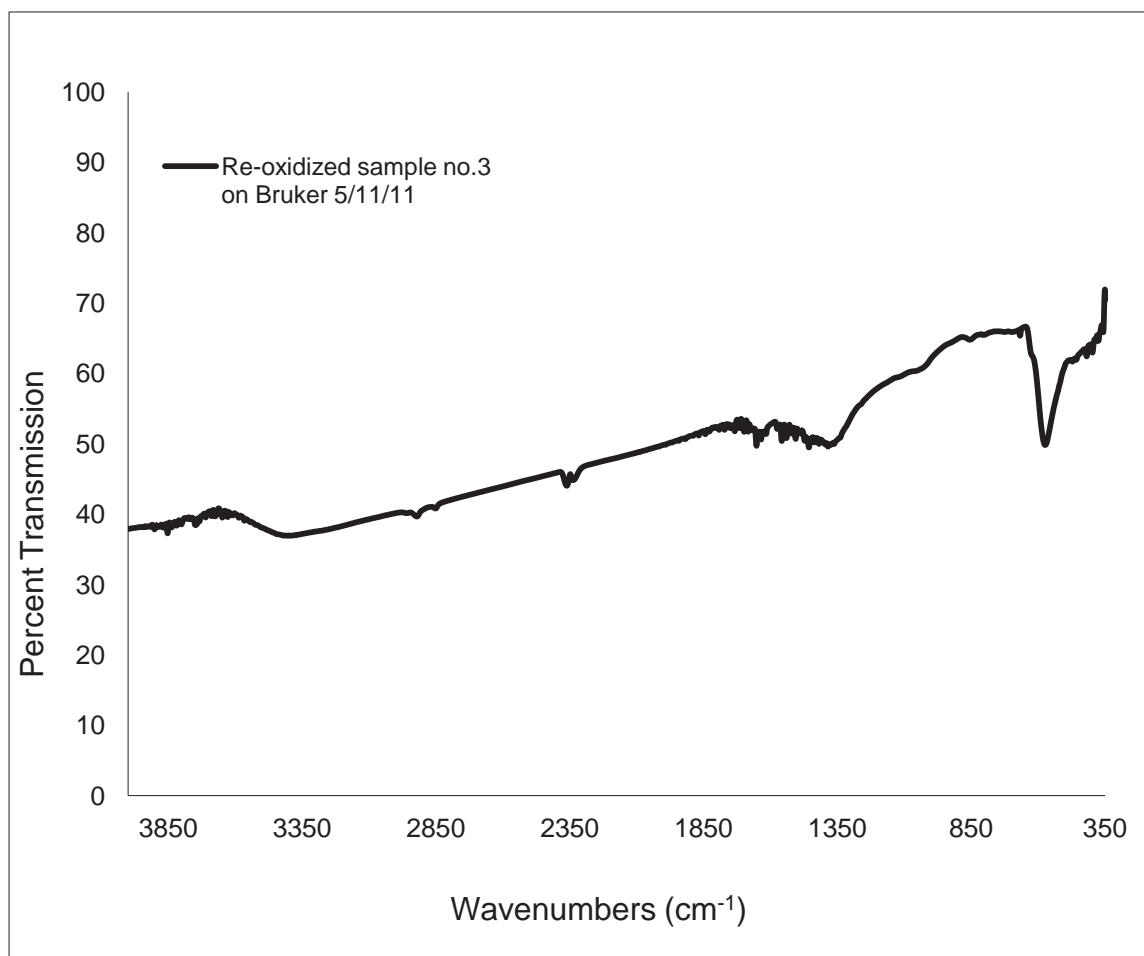


Fig. B.2. IR spectrum of the sample no. 3 (re-oxidized).

(c) IR Spectrum of the No. 4 Compound

Scan conditions for compound no. 4 (800°C heated sample): A KBr pellet of sample no. 4 was prepared and measured on the Bruker, IFS-66 FTIR instrument with 300 scans. The resolution was 4  $\text{cm}^{-1}$ .

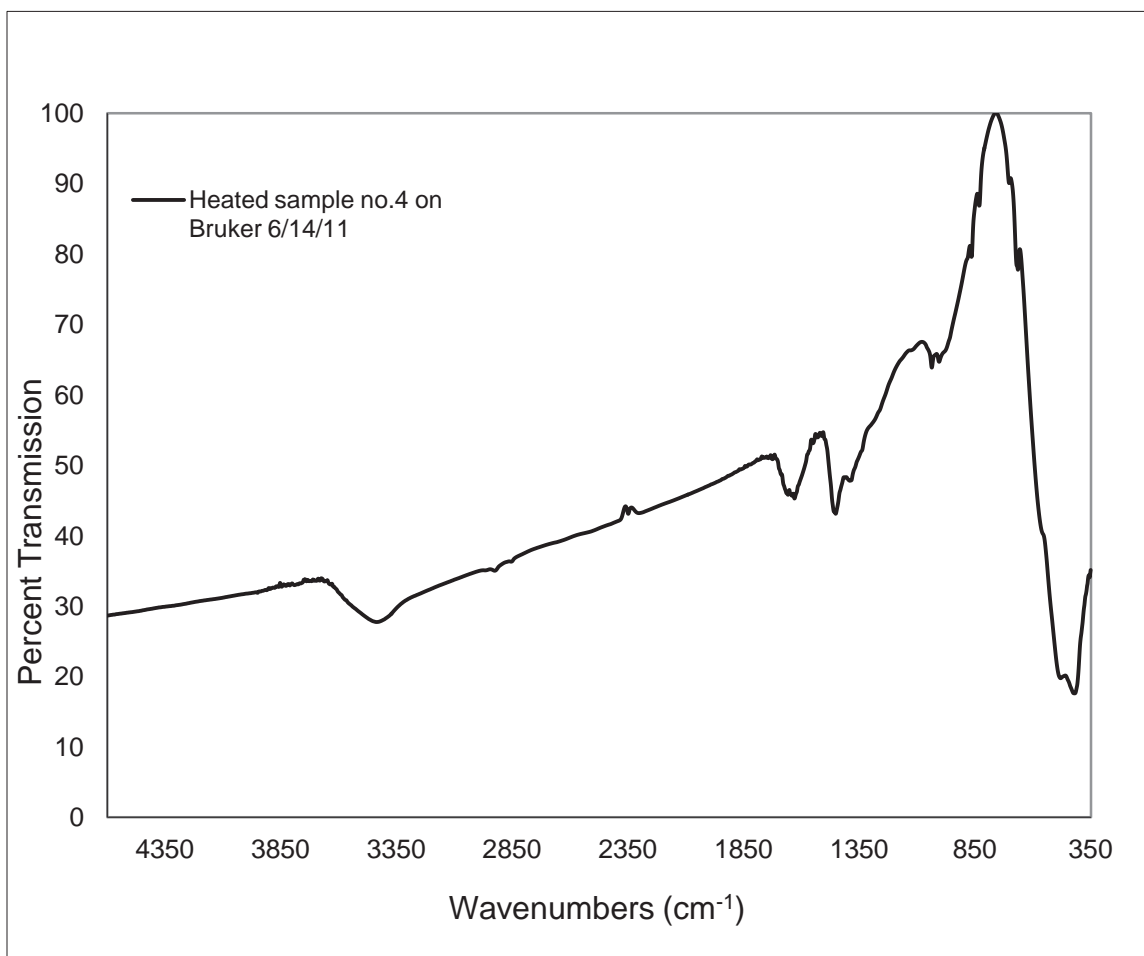


Fig. B.3. IR spectrum of sample no. 4 (heated sample).

(d) IR Spectrum of the No. 5 Compound

Scan conditions for compound no. 5 (re-oxidized of the 800°C heated sample): A KBr pellet of sample no. 5 was prepared and measured on the Bruker, IFS-66 FTIR instrument with 300 scans. The resolution was 4  $\text{cm}^{-1}$ .

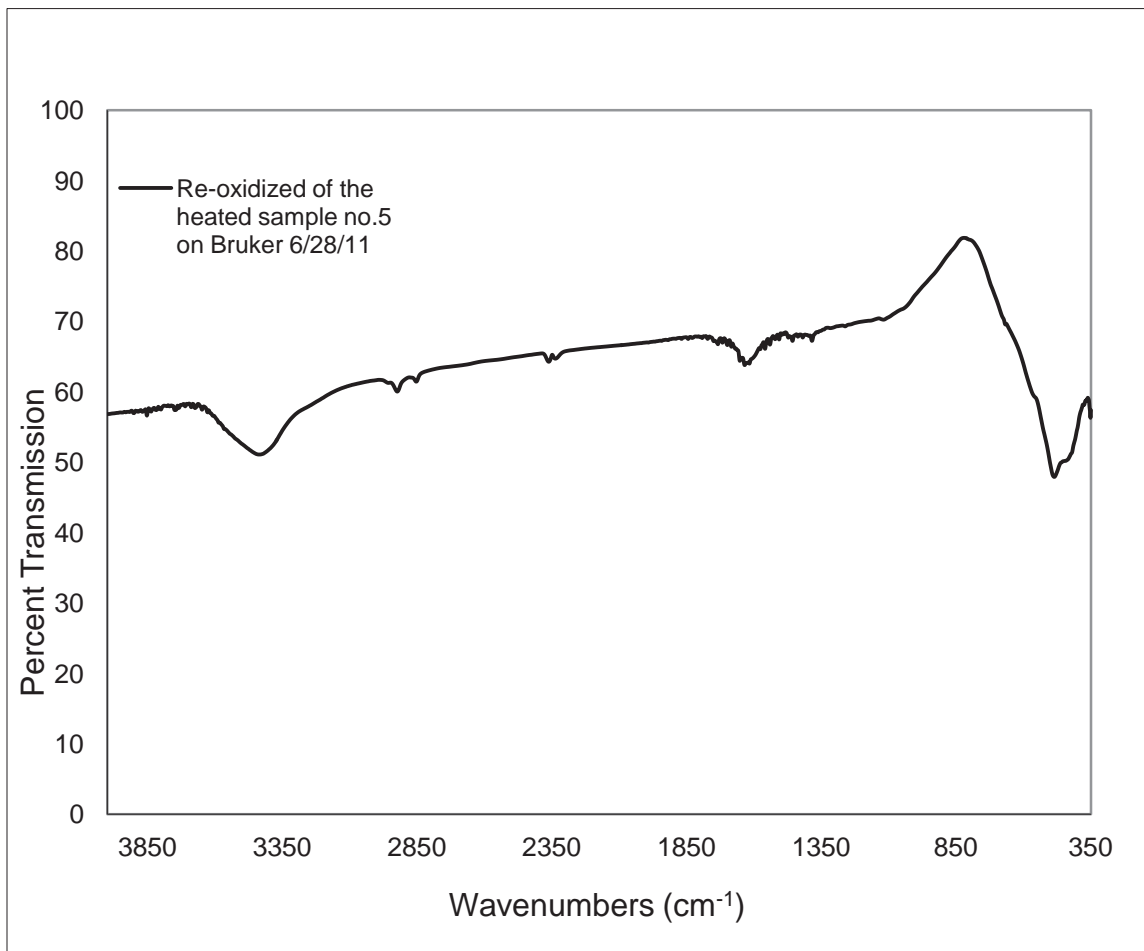


Fig. B.4. IR spectrum of sample no. 5 (re-oxidized of the heated sample) with 300 scans on Bruker, IFS-66 FTIR.



# APPENDIX C

## THE CHARGE/DISCHARGE CAPACITIES OF NICKEL POSITIVE ELECTRODES FOR XRD CHARACTERIZATION

Table C.1.

The capacities, depth of discharge (discharge to 0.0 V), cut off charge voltage, the charge and discharge time of the formed electrode.

Formation process for the formed electrode, Formed-1 (3-23-2012), at 70 mA/cm <sup>2</sup> for first cycle and 20 mA/cm <sup>2</sup> for 2x to 5x						
Cycle Number	Charge Cap. (Ah)	Discharge Cap. (Ah)	DOD	V <sub>cut off</sub> Charge (V)	Charge Time (s)	Discharge Time (s)
1	0.1726	0.0186	0.108	0.663	1785.8	192.6
2	0.0288	0.0205	0.714	0.568	1043.3	745.5
3	0.0215	0.0192	0.926	0.560	780.0	723.2
4	0.0232	0.0199	0.859	0.570	840.0	722.4
5	0.0197	0.00858	0.917	0.569	780.0	716.4

Table C.2.

The capacities, depth of discharge (DOD, discharge to 0.15 V), cut off charge voltage, the charge and discharge time of the formation and cycling process of the charged 1x electrode.

Formation process for the charged 1x electrode, Formed-2(11-15-2011), at 70 mA/cm <sup>2</sup> for the 1 <sup>st</sup> cycle and 20 mA/cm <sup>2</sup> for 2x to 5x cycles						
Cycle Number	Charge Cap (Ah)	Discharge Cap (Ah)	DOD	V <sub>cut off</sub> (V)	Charged Time (s)	Discharged Time (s)
1	0.1314	0.0356	0.271	0.631	1202.9	325.6
2	0.0581	0.0485	0.836	0.547	1800.0	1506.9
3	0.0564	0.0491	0.870	0.545	1749.0	1523.0
4	0.0544	0.0496	0.911	0.545	1687.9	1539.0
5	0.0540	0.0496	0.919	0.545	1673.6	1539.4
One cycle for charged 1x at 10 mA/cm <sup>2</sup> (11-16-2011)						
Cycle Number	Charge Cap (Ah)	Discharge Cap (Ah)	DOD	V <sub>cut off</sub> Charge (V)	Charge Time (s)	Discharge Time (s)
1	0.0835			0.524	5830.0	

Table C.3.

The capacities, depth of discharge (DOD, discharge to 0.15 V), cut off charge voltage, the charge and discharge time of the formation and cycling process of the discharged 1x electrode.

Formation process for discharged 1x electrode, Formed-1(11-15-2011), at 70 mA/cm <sup>2</sup> for the 1 <sup>st</sup> cycle and 20 mA/cm <sup>2</sup> for 2x to 5x cycles						
Cycle Number	Charge Cap. (Ah)	Discharge Cap. (Ah)	DOD	V <sub>cut off</sub> Charge (V)	Charge Time (s)	Discharge Time (s)
1	0.2161	0.0373	0.172	0.555	1980.0	341.4
2	0.0364	0.0240	0.659	0.402	1128.2	743.9
3	0.0327	0.0204	0.624	0.400	1015.8	635.0
4	0.0280	0.0192	0.688	0.400	867.8	597.8
5	0.0247	0.0183	0.742	0.400	766.5	569.2
One cycle for discharged 1x at 10 mA/cm <sup>2</sup> (11-17-2011)						
Cycle Number	Charge Cap (Ah)	Discharge Cap (Ah)	DOD	V <sub>cut off</sub> Charge (V)	Charge Time (s)	Discharge Time (s)
1	0.0513	0.0460	0.897	0.522	3760.0	3383.7

Table C.4.

The capacities, depth of discharge (DOD, discharge to 0.15 V), cut off charge voltage, the charge and discharge time of the formation and cycling process of the charged 10x electrode.

Formation process for the charged 10x electrode, Formed (11-20-2011), at 70 mA/cm <sup>2</sup> for the 1 <sup>st</sup> cycle and 20 mA/cm <sup>2</sup> for 2x to 5x cycles						
Cycle Number	Charge Cap. (Ah)	Discharge Cap. (Ah)	DOD	V <sub>cut off</sub> Charge (V)	Charge Time (s)	Discharge Time (s)
1	0.1374	0.0417	0.303	0.582	1437.3	436.0
2	0.0663	0.0502	0.758	0.528	2427.5	1842.0
3	0.0591	0.0490	0.829	0.520	2163.2	1796.5
4	0.0570	0.0487	0.854	0.520	2088.1	1786.2
5	0.0559	0.0484	0.866	0.520	2048.3	1777.4
Ten cycles for charged 10x electrode at 10 mA/cm <sup>2</sup> (11-20-2011)						
Cycle Number	Charge Cap. (Ah)	Discharge Cap. (Ah)	DOD	V <sub>cut off</sub> Charge (V)	Charge Time (s)	Discharge Time (s)
1	0.0362	0.0081	0.224	0.519	2651.7	594.9
2	0.00872	0.00849	0.974	0.508	639.1	622.4
3	0.00954	0.00973	1.021	0.505	699.0	713.9
4	0.0107	0.0126	1.183	0.505	782.7	926.0
5	0.0142	0.0182	1.280	0.505	1041.5	1333.1
6	0.0196	0.0251	1.282	0.505	1434.1	1839.5
7	0.0266	0.0305	1.147	0.505	1952.8	2240.0
8	0.0319	0.0346	1.084	0.505	2339.9	2536.6
9	0.0355	0.0362	1.020	0.505	2602.8	2656.6
10	0.0368				2696.7	

Table C.5.

The capacities, depth of discharge (DOD, discharge to 0.15 V), cut off charge voltage, the charge and discharge time of the formation and cycling process of the discharged 10x electrode.

Formation process for the discharged 10x electrode, Formed-3 (11-18-2011), at 70 mA/cm <sup>2</sup> for the 1 <sup>st</sup> cycle and 20 mA/cm <sup>2</sup> for 2x to 5x cycles						
Cycle Number	Charge Cap (Ah)	Discharge Cap (Ah)	DOD	V <sub>cut off</sub> Charge (V)	Charge Time (s)	Discharge Time (s)
1	0.1920	0.0429	0.224	0.588	2026.7	453.4
2	0.0521	0.0491	0.941	0.522	1922.8	1812.5
3	0.0538	0.0474	0.882	0.520	1984.0	1753.0
4	0.0507	0.0458	0.904	0.510	1870.4	1693.5
5	0.0496	0.0451	0.909	0.510	1831.0	1666.3
Ten cycles for discharge 10x electrode at 10 mA/cm <sup>2</sup> (11-19-2011)						
Cycle Number	Charge Cap (Ah)	Discharge Cap (Ah)	DOD	V <sub>cut off</sub> Charge (V)	Charge Time (s)	Discharge Time (s)
1	0.5695	0.0921	0.162	0.519	38977.1	6322.1
2	0.0846	0.0826	0.976	0.508	5791.7	5672.5
3	0.0810	0.0796	0.982	0.505	5546.6	5463.9
4	0.0790	0.0777	0.984	0.505	5409.3	5338.8
5	0.0776	0.0762	0.981	0.505	5314.0	5232.9
6	0.0764	0.0749	0.981	0.505	5230.2	5146.2
7	0.0753	0.0738	0.980	0.505	5154.0	5070.2
8	0.0742	0.0726	0.979	0.505	5079.4	4989.3
9	0.0729	0.0715	0.981	0.505	4988.4	4911.3
10	0.0719	0.0705	0.980	0.505	4923.8	4844.1